

N 8 4 - 2 4 5 1 9



Technical Memorandum 86102

# **Energetic Electrons in Impulsive Solar Flares**

**David Allen Batchelor**

**MAY 1984**

National Aeronautics and  
Space Administration

**Goddard Space Flight Center**  
Greenbelt, Maryland 20771

ENERGETIC ELECTRONS IN IMPULSIVE SOLAR FLARES

by

David Allen Batchelor

A Dissertation submitted to the faculty of The  
University of North Carolina at Chapel Hill in partial  
fulfillment of the requirements for the degree of  
Doctor of Philosophy in the Department of Physics and Astronomy

Chapel Hill

1984

Approved by:

Carol Jo Brunell

Adviser

Wayne A. Christensen

Adviser

Bruce W. Carnoy

Reader

W. J. Thompson

Reader

James York

Reader

**Page intentionally left blank**

**Page intentionally left blank**

DAVID ALLEN BATCHELOR. Energetic Electrons in Impulsive Solar Flares  
(Under the direction of CAROL JO CRANNELL and WAYNE A. CHRISTIANSEN)

#### ABSTRACT

Impulsive bursts of hard X rays and microwaves are observed during most solar flares, and both emissions can be attributed to a common distribution of source electrons with energies from approximately 10 keV to several hundred keV. A detailed account of the evolution of the electron distribution is crucial to a complete description of the energy release process in flares. In this dissertation, a new analysis is made of a thermal flare model proposed by Brown, Melrose, and Spicer (1979) and Smith and Lilliequist (1979). They assumed the source of impulsive hard X rays to be a plasma at a temperature of approximately  $10^8$  K, initially located at the apex of a coronal arch, and confined by ion-acoustic turbulence in a collisionless conduction front. Such a source would expand at approximately the ion-sound speed,  $c_s = (kT_e/m_i)^{1/2}$ , until it filled the arch. Brown, Melrose, and Spicer (1979) and Smith and Brown (1980) argued that the source assumed in this model would not explain the simultaneous impulsive microwave emission. In contrast, the new results presented here show that this model leads to the development of a quasi-Maxwellian distribution of electrons that explains both the hard X-ray and microwave emissions. This implies that the source sizes can be determined from observations of the optically-thick portions of microwave spectra and the temperatures obtained from associated hard X-ray observations. In this model, the burst emission would rise to a maximum in a time,  $t_r$ , approximately equal to  $L/c_s$ , where  $L$  is the

half-length of the arch. New observations of these impulsive flare emissions are analyzed herein to test this prediction of the model. The X-ray observations were obtained with the Hard X-ray Burst Spectrometer on board the Solar Maximum Mission spacecraft, and the microwave observations were obtained from the Bern Radio Observatory in Switzerland. The results of this investigation are in good agreement with the model and are not explained by any other flare models which have been considered.

**DEDICATION**

**To Laurie Jean Batchelor**

**Page intentionally left blank**

**Page intentionally left blank**

## ACKNOWLEDGEMENTS

A host of colleagues and friends have helped to make this work possible. First, I wish to express my deep appreciation to Dr. Carol Jo Crannell for providing me with the opportunity to undertake this research at NASA Goddard Space Flight Center, and for serving as my research advisor, both at NASA-GSFC and as a member of my dissertation committee. She has tried to convey to me a broad knowledge and critical understanding of the subject of solar flares and the many physical processes that are involved in them. Her previous work on the flare problem has served as foundation and stimulus of the investigations described herein, and her guidance has led me to address the most fundamental issues at hand. Her tireless pursuit of the most precise possible expression of an idea has led to many improvements in this dissertation.

I am also particularly grateful to Dr. Wayne A. Christiansen, who served on the dissertation committee and as my faculty advisor at the University of North Carolina, who arranged for me to undertake a dissertation project with Dr. Crannell, and who provided valuable advice in the writing of this dissertation. The other members of the dissertation committee, Dr. Bruce Carney, Dr. William J. Thompson, and Dr. James W. York, Jr., also made many helpful comments. I also wish to thank the other faculty members and staff of the Department of Physics and Astronomy at UNC for the cooperation and encouragement that made possible my research at NASA-GSFC. Dr. Thompson and Mrs. Elizabeth Henderson were particularly helpful in keeping me registered as a student, despite my remote post.

I wish to thank Dr. Brian R. Dennis, Dr. Larry E. Orwig, and Mr. Kenneth J. Frost of NASA-GSFC for access to the Hard X-Ray Burst Spectrometer data and analysis facilities, and for kind advice and assistance that contributed much to this work. The data reduction was greatly facilitated by the use of the excellent HXRBS data analysis software, for which Mr. Harold E. Dennis and Ms. A. Kimberley Tolbert of Science Applications Research, and Mr. Tom Chewning, were responsible. I am also grateful to Dr. Alan L. Kiplinger of Applied Research Corporation for the use of his extremely versatile OCTOPUS program, and for many helpful discussions of the flare problem. Mr. G. Shelby Kennard and Mr. Bernard E. Gibson advised me on the practical uses of the HXRBS data analysis software. The analysis also could not have been performed without software contributed by Mr. John Bonomo.

I wish to thank Dr. Andreas Magun and Dr. Herbert Wiehl of the University of Bern, Switzerland, for kindly providing calibrated microwave data from Bern Radio Observatory, and for much essential advice on the interpretation of their observations.

Many people assisted me in the use of facilities at NASA-GSFC. In particular, I wish to thank Dr. Joseph Gurman and Mr. David Pothier for indispensable help in the use of the VAX 11/750 at the Solar Maximum Mission Experimental Operations Facility. Mr. Ed Sullivan and Ms. Clara Hughes provided additional programming and data processing assistance with the PDP 1134 in the Laboratory for Astronomy and Solar Physics.

I also thank Dr. Jason Porter for comradeship during the wee hours.

Helpful discussions of this work with Dr. John C. Brown, Dr. David Forrest, Dr. Dean F. Smith, Dr. Dan S. Spicer, and Dr. Loukas Vlahos are

gratefully acknowledged.

This work was supported in part under contract NAS 5-26341 through Energy/Environmental Research Group of Tuscon, Arizona. I thank Dr. John Scott and Mr. Eric Craine of E/ERG for managing that portion of my support. Additional support was provided under grant NSG 5066 through the Catholic University of America, and I thank Dr. Carl Werntz for managing the grant. Funding for both the contract and the grant was provided via the Goddard Space Flight Center from the Solar and Heliospheric Physics Office and the Solar-Terrestrial Theory Program of NASA Headquarters. I am grateful to Dr. Reuven Ramaty for arranging that funding. For the past year, I have been supported as a NASA Graduate Student Researcher at the Laboratory for Astronomy and Solar Physics at Goddard Space Flight Center.

The encouragement and support, both moral and financial, of my family has been crucial to the completion of this work. For all they have provided, I thank my mother, Mrs. Betty N. Batchelor, my father, Mr. Victor S. Batchelor, my grandmother, Mrs. Geneva J. Nethercutt, my aunt and uncle, Mrs. Lou J. Kennedy and Mr. Gordon Kennedy, and my aunt, Ms. Mary Jackson.

I am also grateful to Mr. Mark D. Beasman and Mrs. Mary A. Scroggs for kindly providing indispensable buoyancy enhancements.

Finally, I acknowledge my deepest debt of gratitude to Ms. Laurie Jean Batchelor, my wife, for extraordinary patience, countless hours of work and years of self-sacrifice. Her commitment to the importance of my work has provided invaluable reassurance during these many years of graduate school.

**Page intentionally left blank**

**Page intentionally left blank**

## CONTENTS

DEDICATION . . . . .	v
ACKNOWLEDGEMENTS . . . . .	vii
I. INTRODUCTION . . . . .	1
II. PHYSICS OF HARD X-RAY AND MICROWAVE EMISSIONS . . . . .	11
2.1 Physical Conditions at the Flare Site . . . . .	11
2.2 Primary Energy Release . . . . .	14
2.3 Hard X Rays . . . . .	18
2.3.1 Phenomenology of Impulsive Hard X-ray Bursts . . . . .	18
2.3.2 The Emission Process — Bremsstrahlung <u>vs.</u> Alternatives . . . . .	27
2.3.3 Models of the Bremsstrahlung Source . . . . .	29
2.3.4 Nonthermal Thick-target Model . . . . .	30
2.3.5 Nonthermal Trap-plus-precipitation Model . . . . .	41
2.3.6 Thermal Models . . . . .	45
2.4 Microwaves . . . . .	51
2.4.1 Phenomenology of Impulsive Microwave Bursts . . . . .	51
2.4.2 The Emission Process — Gyrosynchrotron Radiation . . . . .	57
2.4.3 Radiative Transfer . . . . .	58
2.4.4 Gyrosynchrotron Emission from Thermal Electrons . . . . .	64
2.4.5 Gyrosynchrotron Emission from a Power-law Distribution of Electrons . . . . .	67
2.4.6 Inhomogeneous Sources . . . . .	69
III. THE THERMAL MODEL WITH CONDUCTION FRONT CONFINEMENT . . . . .	73
3.1 Development and Previous Applications of the Model . . . . .	73

3.2	The High-energy Limit of Confinement and Its Implications for Microwave Emission . . . . .	81
3.2.1	Limits on the Confinement of Electrons According to Smith and Brown (1980) . . . . .	83
3.2.2	Population of the Maxwellian Tail . . . . .	85
3.2.3	Re-evaluation of the Confinement Limits . . . . .	89
3.3	A Test of the Model Based on the Revised Predictions . . .	92
3.4	Other Derived Parameters . . . . .	97
3.5	Efficiency of the Conduction-Front Model . . . . .	99
IV.	OBSERVATIONS AND DATA REDUCTION . . . . .	101
4.1	Hard X Rays . . . . .	101
4.1.1	The Hard X-Ray Burst Spectrometer . . . . .	101
4.1.2	Instrumental Effects . . . . .	104
4.1.3	Simulation of the Instrument Response . . . . .	109
4.1.4	Spectral Analysis Procedure . . . . .	112
4.2	Microwaves . . . . .	115
4.2.1	Spectral Coverage and Temporal Resolution . . . . .	115
4.2.2	Flux Calibration . . . . .	116
V.	THE TEST OF THE MODEL . . . . .	119
5.1	Flare Selection . . . . .	119
5.2	Selection of a Homogeneous Sample of Impulsive Rises . . .	121
5.3	Observed and Derived parameters for Each Rise . . . . .	122
5.4	Correlation Analysis of Observed and Predicted Rise Times .	129
5.5	Uncertainties in the Measurements . . . . .	132
5.6	Consistency Checks . . . . .	132
5.6.1	Search for More Fundamental Correlations . . . . .	132
5.6.2	Limb Rise Analysis . . . . .	138

5.6.3 Comparison with Results of Crannell et al. (1978) . . 139

5.7 Other Derived Parameters . . . . . 141

VI. CONCLUSIONS AND SUGGESTIONS FOR FUTURE INVESTIGATIONS . . . . 143

REFERENCES . . . . . 147

APPENDIX: PROGRAMS FOR SIMULATION OF PULSE PILE-UP . . . . . 157

## Chapter I

### INTRODUCTION

Solar flares are storms in the solar atmosphere. They last for times ranging from seconds to hours, and involve the release of prodigious quantities of energy in a multitude of forms. These forms include: electromagnetic radiation ranging from energetic  $\gamma$  rays to radio emissions at low frequencies; energetic particles such as electrons, neutrons, and various species of ions which are released into the interplanetary medium; and clouds of gas which are sometimes ejected into the corona (cf. reviews by Svestka 1976; Sturrock 1980; Brown and Smith 1980; Priest 1981). Estimates of the energy released during the largest flares range as high as  $10^{32}$  erg (Svestka 1976). The flare luminosity never exceeds a small percentage of the total solar luminosity, but the flare energy comes from a region estimated to be only  $\approx 10^4$  km in size, so that a given volume of flaring atmosphere may briefly produce thousands of times as much power as an equal volume of the quiet Sun.

No existing theory adequately accounts for the flare phenomenon. No theory is available for accurate predictions of the onset of flare activity, the intensity of flare emissions, or particular manifestations during the event, from pre-flare observations. Such a theory is desirable not only for reasons of scientific interest, but also because

of the significant and growing impact of flares on human activities. For example, flares induce magnetic disturbances at the Earth that make navigation difficult. Radio bursts, emitted during flares, interfere with radio communications and radar. X-ray and particle radiations from flares also make the space environment hazardous for manned exploration and unmanned instrument satellites (e.g. radiation from a large flare recently damaged an important weather satellite, GOES West, interrupting photographic weather map coverage of the Pacific). As the activities of human civilizations are extended into space, the understanding and forecasting of flares will become as vital as the present forecasting of the weather.

Scientific reasons for studying flares are many. Flares occur in upwellings of highly magnetized gas, between  $10^4$  and  $10^5$  km in size, known as active regions. Flare activity is apparently triggered in the coronal part of an active region, where the solar atmosphere consists of a highly ionized plasma, permeated by a magnetic field of order 100 G. Much of the activity occurs in plasma that is confined in arch- or arcade-shaped configurations of magnetic flux tubes with sizes comparable to that of the active region. A flare is therefore a natural laboratory in which the behavior of plasmas can be studied on time scales and length scales that are inaccessible in the terrestrial laboratory. During a flare, the plasma undergoes instabilities and excitations in a sequence that is only vaguely understood. The instabilities probably involve rearrangements, or reconnections, of the magnetic field configuration in the active region, with the result that a portion of the field is annihilated. The energy density,  $B^2/8\pi$ , associated with the annihilated field component is the most plausible

source of energy for the flare. During a flare, the plasma is heated from an initial temperature of about  $2 \times 10^6$  K to much higher temperatures. In addition, various particle species are accelerated and interact with the ambient medium at high energies. Magnetic field annihilation can indeed supply enough energy to heat the gas and accelerate the particles, but the specific electrodynamic and hydrodynamic processes that actually occur are not yet fully understood. A full, detailed account of the mechanisms that heat and accelerate particles in flares would have wide applicability in other areas of astrophysics. For example, flare stars, dwarf novae, and accretion disks are likely sites for similar processes. Because of the Sun's relative nearness, it is possible to study these important plasma processes in the solar atmosphere with much greater detail than in more remote astrophysical plasmas.

As a step toward understanding the energy release mechanisms, many investigators have studied the most energetic particles that are found in flares: energetic electrons and ions. In this work, the focus will be on the energetic electrons. These electrons manifest their presence through a variety of emission mechanisms, and play an important role in the energy transport and total energy budget of a given flare (cf. reviews by Brown 1975, 1976; Brown and Smith 1980). The electrons emit hard X rays by collisional bremsstrahlung with atomic nuclei, producing a steep continuum spectrum that is observed at photon energies above  $\approx 10$  keV. Because the electrons gyrate in a magnetic field of order 100 G, they also emit microwaves by the gyrosynchrotron process, producing a continuum spectrum at frequencies in the range from approximately 1 to 100 GHz. These two emissions, hard X rays and

microwaves, provide the most direct information available about the in situ electron population. The time histories of the two emissions are often very similar, as can be seen, for example, in Figure 1-1. Both emissions can be attributed to a common distribution of source electrons (cf. Holt and Ramaty 1969; Crannell et al. 1978). It has never been conclusively demonstrated that both emissions originate in a common source, however.

A detailed account of the evolution of the distribution of energetic electrons is crucial to a complete description of the energy release and its sequel. Analysis of simultaneous images in these emissions would greatly facilitate such an account, and would help to establish whether or not both emissions originate in a common electron distribution. Simultaneous imaging of both emissions has been accomplished only for one flare (Hoyng et al. 1983); however, the results are open to multiple interpretations. Many hard X-ray images obtained to date are also limited to the low-energy end of the range of interest,  $\approx 20$  keV, and may be misleading for the interpretation of the observations at 35 to 500 keV which we will consider here. Present imaging observations of both hard X-ray and microwave emissions also sacrifice temporal resolution and spectral coverage to obtain images in a fixed frequency or energy range.

The objective of this work is to make deductions about the evolution of the electron distribution, based on analysis of the dynamic spectral properties of both emissions and on theoretical considerations. The observations analyzed here are not spatially resolved. Important new information about the source structures can be drawn from their analysis, nevertheless, because these observations are the best ever

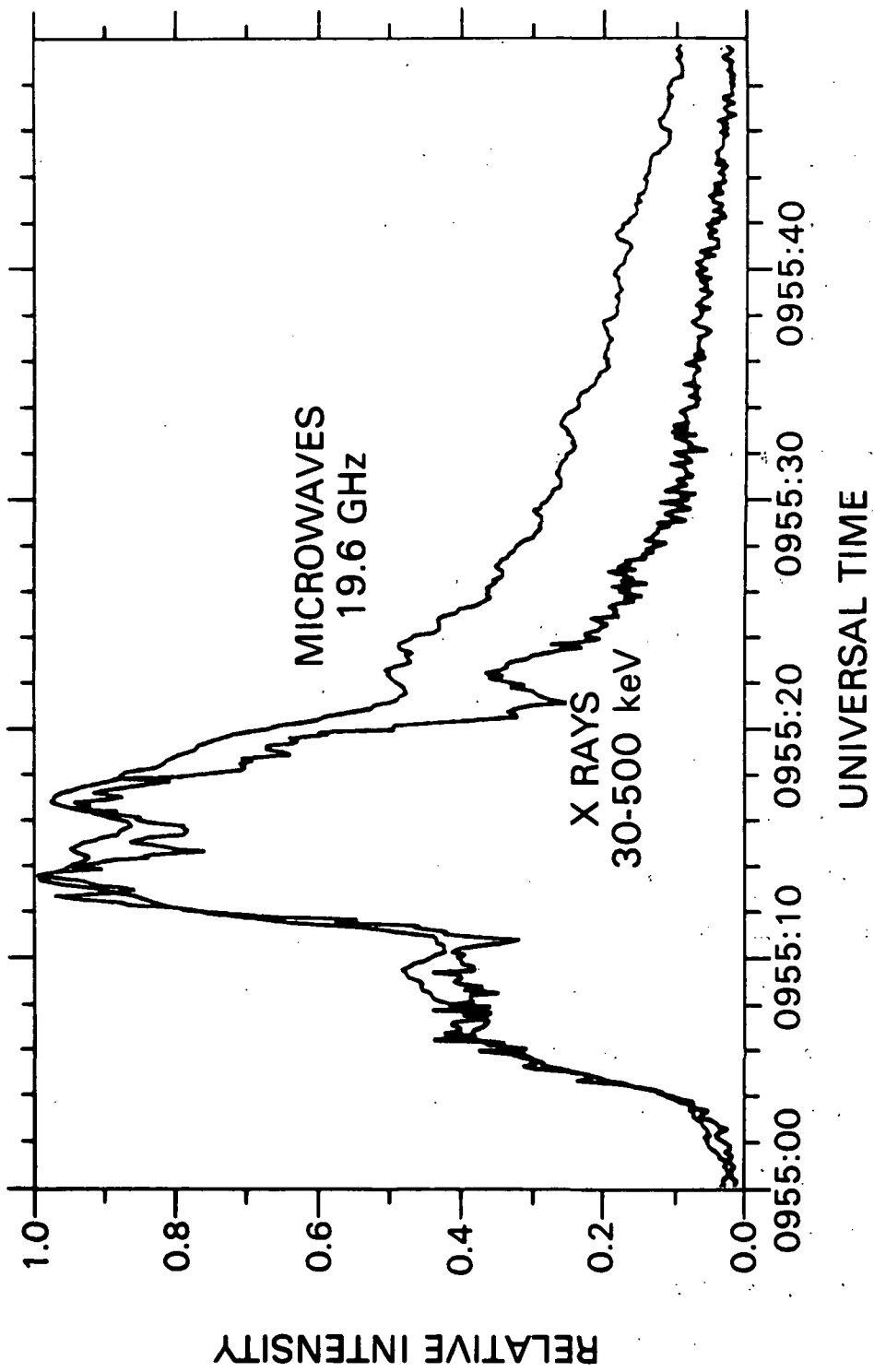


Figure 1-1. An example of the similarity between hard X-ray and microwave time histories. Times are in hours, minutes, and seconds of Universal Time.

obtained in terms of spectral coverage and temporal resolution of both emissions. The hard X ray observations were made with the Hard X-Ray Burst Spectrometer (HXRBS) on board the Solar Maximum Mission spacecraft (SMM). Because hard X-ray observations must be made from above the bulk of the Earth's atmosphere, and because SMM was operating during the peak of solar activity, the HXRBS has provided data of unprecedented quality for nearly 7000 flares since launch. The complementary microwave observations were made at the Bern Radio Observatory in Switzerland. The combination of fine temporal resolution of the microwave data with numerous observing frequencies is also unprecedented and was crucial to the success of the analysis.

Without spatially resolved observations, the characteristics of the source electrons and the region in which they interact cannot be uniquely determined from the analysis of either emission alone. In the case of the hard X rays, the density of the source can be determined from a spectrum only with additional information about the source volume. Similarly, the density, magnetic field, and electron energy distribution function cannot all be specified by measurement of the microwave spectrum alone. (For brevity, the distribution of electrons as a function of kinetic energy is referred to hereinafter as simply the electron distribution.)

If certain idealizations are made, however, a description of the source can be obtained from coincident analysis of the hard X-ray and microwave emissions. It must be assumed that the source is approximately uniform in magnetic field and electron energy distribution. (If variations in magnetic field or electron distribution were large, the observed spectra would be dominated by these variations,

resulting in the need for more free parameters to characterize the spatial scale and magnitude of the variations.) It must also be assumed that the electron distribution has a particular functional form, such as a Maxwellian or power law. Both of these idealizations are consistent with available data, and are commonly employed in interpretations of hard X-ray and microwave spectra. In order to determine the desired parameters, a third assumption relating the two emissions is required. One possible assumption is that both the hard X-ray and microwave emissions originate in a common source distribution. This assumption is referred to hereinafter as the common source hypothesis, and is justified by the similar time histories of the emissions. Under these assumptions, the two spectra can be used to derive the physical parameters that characterize the source: its size, magnetic field, and the parameters that specify the electron distribution function (of the assumed form). Further support for the common source hypothesis in the context of a particular flare model is provided by theoretical considerations in Chapter III of this work. The hypothesis then allows the evolution of the electron distribution to be determined.

The timescales of variations in hard X-ray and microwave flux during flares range from minutes to fractions of a second. Variations in flux with e-folding times of 30 s or less are commonly referred to as "impulsive". The sudden rises in Figure 1-1 serve as examples. Variations on much longer timescales are commonly characterized as "gradual". No particular timescale has been universally established as the boundary between these two classes of dynamical behavior, but all investigators would classify a sharp rise in flux during 30 s or less as impulsive. Complex flares are common, in which impulsive and gradual

variations take place concurrently. There is some evidence that the two classes of behavior result from energy release under qualitatively different conditions (e.g. Tsuneta 1983).

One of the most crucial and controversial questions about solar flares is whether the impulsive hard X-ray and microwave bursts originate in a thermal or nonthermal population of energetic electrons. In nonthermal models, the hard X rays are produced by accelerated electrons as they interact with the constituents of the ambient medium. This process is very inefficient because only one part in  $10^5$  of the total energy of the electron distribution goes into the production of hard X rays in the energy range of most of the emission, from about 10 to 100 keV. The most efficient of the nonthermal models, known as the "thick-target" model, invokes intense electron beams created in the corona and incident upon the chromosphere. Doubts about the prospects for creation and stabilization of such beams have been raised by Smith (1975), Melrose and Brown (1976), Hoyng, Brown, and van Beek (1976), Hoyng, Knight, and Spicer (1978), and Colgate (1978). In addition, Brown et al. (1983a) have shown that the temporal evolution of the height structures of five impulsive flares is entirely inconsistent with the thick-target model of hard X-ray bursts. Renewed interest in thermal flare models has been kindled by these difficulties with nonthermal models and by recognition of the potentially greater emission efficiency of a confined, collisionally relaxed X-ray source. Detailed discussions of these points are given by Crannell et al. (1978), Mätzler et al. (1978), Brown, Melrose, and Spicer (1979, hereinafter BMS), and Smith and Lilliequist (1979, hereinafter SL). No observational evidence has been published to date, however, that

distinguishes unambiguously between the two classes of models.

In this work, new observations of impulsive hard X-ray and microwave bursts are analyzed, and the results are compared with predictions of a particular thermal flare model which has received much attention in the literature. In the model, both emissions are assumed to originate in a hot plasma at a temperature of order  $10^8$  K (Chubb 1972; Crannell et al. 1978). The plasma is effectively confined by the development of collisionless conduction fronts, as proposed by BMS and by SL. In the present work, a new analysis of the model is presented, showing that both the hard X-ray and microwave emissions originate in the same quasi-Maxwellian electron distribution; i.e., the common source hypothesis is a natural consequence of the thermal model considered here. This is contrary to the results of previous analyses (BMS; Smith and Brown 1980), which are described in Chapter III. In the context of a thermal flare model, the common source assumption provides a new observational test of the model: the rise time of the emission specifies a relation of size to temperature of the source, which can be compared with the relationship derived from the observed hard X-ray and microwave spectra. The source sizes are calculated by means of techniques first applied to the analysis of solar flares by Crannell et al. (1978). The calculation of the theoretical rise time is shown to be in excellent agreement with the new observations, as well as providing a physical basis for the analysis that was performed by Crannell et al.

The plan of this dissertation is as follows. In Chapter II, the theory of the emission mechanisms is outlined and a brief review is given of some models that figure in current debates about the physical

origin of impulsive hard X-ray and microwave bursts. Chapter II also includes a discussion of some general properties of the hard X-ray and microwave dynamic spectra. In Chapter III, the thermal flare model which was first proposed by BMS and SL is discussed in detail. The elements of the model are described, and the model is developed further, resulting in a revised view of its predictions and the formulation of the test of the theoretical rise time. In Chapter IV, the observations and the data reduction techniques employed in this work are described. In Chapter V, the revised predictions of the model are compared with the observations of a sample of 20 flares, and agreement is found. Conclusions of this work are summarized in Chapter VI and recommendations are made for future research.

The principal conclusion of this work is that, of the impulsive solar flares models currently found in the literature, the thermal model considered here provides the most straightforward explanation of the observations presented in Chapter V. Indeed, there is no other extant model that predicts a relationship between burst dynamics and spectra such as that observed. While a conclusive test of the model awaits future imaging observations, the model should be regarded as a very strong candidate for explaining impulsive bursts.

## Chapter II

### PHYSICS OF HARD X-RAY AND MICROWAVE EMISSIONS

#### 2.1 Physical Conditions at the Flare Site

The energetic electrons that produce hard X-ray and microwave bursts are believed to originate at coronal heights in solar active regions. Densities derived from observations of active regions at extreme ultraviolet wavelengths are typically in the range from 0.5 to  $5 \times 10^9 \text{ cm}^{-3}$  (Foukal 1975; Svestka et al. 1977; Priest 1978). Densities derived from flare models are typically between  $10^9$  and  $10^{11} \text{ cm}^{-3}$  (Crannell et al. 1978; Svestka 1976 and references therein). Direct, model-independent measurements of density in burst sources are not currently available. In the low corona and chromosphere, the density is known to increase rapidly with decreasing altitude, reaching densities of order  $10^{15} \text{ cm}^{-3}$  in the upper photosphere. Magnetic fields derived from the competing models of the source region are of the order of a few hundred gauss. Although independent measurements of the magnetic field in the burst source are also unavailable, the derived values are consistent with the values typically obtained by extrapolation of photospheric field patterns into the corona (e.g. Rust and Bar 1973). (The photospheric field is directly measurable, with a magnetograph; cf. Bumba 1958; Severny 1958; Rust 1976 and references therein.) The

initial coronal temperatures are of order  $2 \times 10^6$  K, as measured by soft X-ray instruments (e.g. Van Hoven et al. 1980).

The plasma is characterized by a number of physical parameters which are conveniently introduced here. The electron plasma frequency is defined by the expression  $\omega_e = (4\pi n_e e^2 / m_e)^{1/2}$ . The plasma behaves as a system of coupled oscillators with the characteristic frequency  $\omega_e$ , and, consequently, no electromagnetic radiation can propagate through the plasma at a frequency  $\omega$  less than  $\omega_e$ . The velocity  $v_e$ , defined as  $(kT_e / m_e)^{1/2}$ , is known as the electron thermal velocity. (It should be noted that  $v_e$  is not  $v_{rms}$ , the root-mean-square width of the Maxwellian speed distribution,  $v_{rms} = 3^{1/2} v_e$ ; nor is it  $v_{mean}$  of the distribution,  $v_{mean} = (8/\pi)^{1/2} v_e$ . Cf. Reif 1965, pp. 262-269.) Because the charged particles that comprise the plasma are free to move, an isolated test charge attracts particles of opposite charge, which move to shield its electrostatic field from the rest of the plasma. The electric potential in the vicinity of a particle with charge  $e$  is not the vacuum field  $\phi_{vac} = e/r$ , but instead is  $\phi = \phi_{vac} \exp(-r/\lambda_{De})$ , where  $\lambda_{De}$  is the electron Debye length,  $v_e/\omega_e$ . The Coulomb logarithm,  $\ln \Lambda$ , is defined as  $\ln(4\pi n_e \lambda_{De}^3)$ , and characterizes the relative importance of small-angle and large-angle deflections that are experienced by the particles of the plasma during Coulomb collisions. (The physical significance of these plasma parameters is explained in more detail by Spitzer 1962, and by Krall and Trivelpiece 1973.)

Under pre-flare conditions, the plasma is prevented from crossing the magnetic field, or, equivalently, the field is "frozen into" the plasma. The charged particles that compose the plasma gyrate around the field lines in helical paths with radii equal to  $r_{Lj} = v_+/\Omega_j$ , the Larmor

radius, where  $v_{\perp}$  is the component of the particle's velocity perpendicular to  $\vec{B}$ ,  $\Omega_j = eB/m_jc$  is the Larmor frequency (a.k.a. the cyclotron frequency), and  $j$  labels the various particle species, electrons and ions. Under certain conditions, it is possible for the field to diffuse out of the plasma, but this process requires the existence of eddy currents. Consideration of the fluid equations for a plasma shows that the timescale for the field to diffuse out of the plasma is  $\tau_m = 4\pi\sigma\lambda_B^2/c^2$ , where  $\sigma$  is the electrical conductivity,  $\lambda_B$  is the length that characterizes field gradients in the plasma, and  $c$  is the speed of light (Krall and Trivelpiece 1973, pp. 105-106). The plasma has a very high conductivity,  $\sigma = n_e e^2 / f_c m_e$ , where the frequency of Coulomb collisions in the plasma is given by  $f_c = (\omega_e \ln \Lambda) / (2\pi n_e \lambda_{De}^3)$ . For the pre-flare conditions described above,  $f_c \sim 10^3 \text{ s}^{-1}$ ,  $\sigma \sim 10^{15} \text{ s}^{-1}$ , and  $\tau_m \sim 10^{-5} \lambda_B^2$ . The gradient scale length is of order  $10^2 \text{ km} = 10^7 \text{ cm}$ , so  $\tau_m \sim 10^9 \text{ s}$ . Thus the field does not diffuse away in the lifetime of an active region, which is of order  $10^6 \text{ s}$  (a few solar rotations). A more detailed discussion of the physical principles that apply is found in Krall and Trivelpiece (1973, Chap. 3).

The field and the plasma are frozen together, but the dynamical behavior of the fluid plasma in the corona is controlled primarily by the field. The physical parameter of interest is the plasma  $\beta$ , which is defined as  $w_T/w_B$ , where  $w_T = (3/2) \sum n_j kT_j$  is the thermal energy density (or pressure) in the plasma, and  $w_B$  is the energy density of the field,  $B^2/8\pi$ . For most of the corona,  $\beta \ll 1$ , indicating that dynamics of the plasma are dominated by the confining influence of the field.

## 2.2 Primary Energy Release

A cardinal characteristic of flares is their unpredictability from presently available pre-flare measurements. At the height of the solar cycle, there are usually several active regions on the observable part of the Sun at one time. Flares occur in these regions, apparently at random, usually at intervals of hours or days, but sometimes only minutes apart. This behavior is often interpreted as the build-up or storage of energy, punctuated by its sudden release when, as its structure evolves, the field configuration becomes unstable.

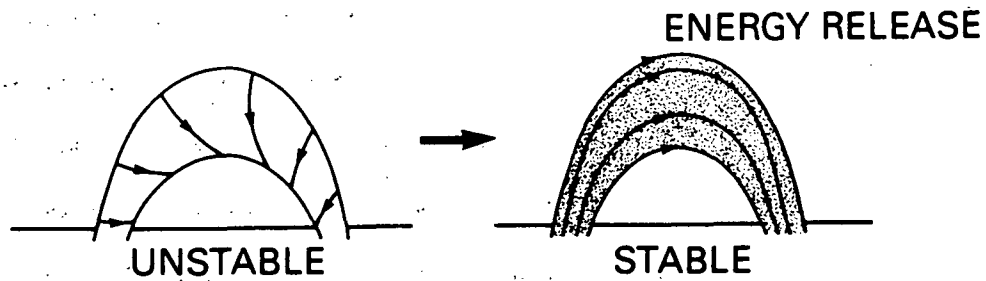
Active regions are bi-polar, in that the photospheric fields are arranged in patches of positive and negative flux. At the photospheric level, observations show that  $\beta \gtrsim 1$ . Because of the turbulent, vortical motions in the photosphere, and the up-wellings of new, magnetized gas, the field configurations in active regions can take on very complex geometries. Flare activity observed in H $\alpha$  emission (6563 Å) is associated with sites of strongly sheared magnetic field in active regions (Svestka 1976 and references therein). The so-called neutral line, the boundary between patches of positive and negative flux, is such a site. Arch-shaped flux tubes cross the neutral line and connect the patches of opposite polarity. Some, but by no means all, of these arches rise into the corona, reaching altitudes  $\gtrsim 2000$  km. Coronal arches are observable only when luminous gas fills them, a common occurrence after a flare. Motion of the photospheric layers can stretch and twist these flux tubes, or press them together so that regions of opposite field collide; both of these processes shear the field. Sheared field configurations are necessary for the occurrence of

field annihilation via reconnection, the process that is believed to supply the flare energy.

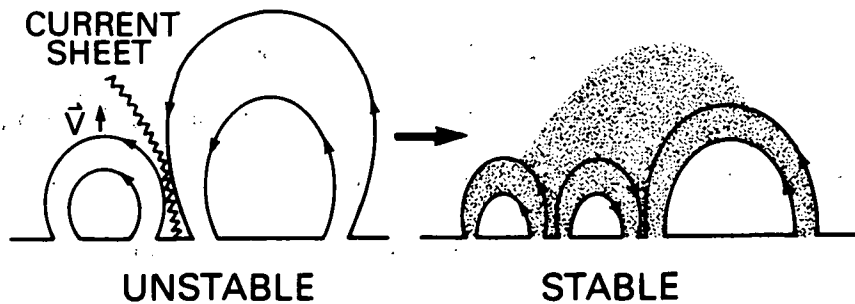
The two sheared field configurations that have received the most attention are the twisted flux tube, or arch, and the current sheet. These configurations are illustrated schematically in Figure 2-1. A current sheet is formed when regions of oppositely-directed flux are pressed together, e.g. if two arches collide. Current sheets were studied extensively by Petschek (1964), and many others, and are fundamental to the emerging flux model for the flare energy release proposed by Heyvaerts, Priest, and Rust (1977). An excellent review of the history and present status of this reconnection mechanism is given by Priest (1981b).

A twisted flux tube is currently regarded as a more likely site for impulsive energy release. Such an arch, characterized by a helical field bent into an approximately semi-circular form, is subject to magnetohydrodynamic (MHD) and resistive MHD instabilities, which lead to impulsive release of energy in the forms of heat, mass motions, and accelerated particles. These instabilities have been studied because they occur in plasma fusion experiments with tokomaks, and the results have been applied to the solar flare problem by Spicer (1976, 1977), Van Hoven (1976), and others. The instability with the most potential to explain impulsive flare energy release is the tearing mode (Furth, Killeen, and Rosenbluth 1963). This instability occurs when the ratio of the twisted field component to the component of  $\vec{B}$  along the arch reaches unity. The arch is then unstable to the growth of a current distribution that annihilates the twisted component and dissipates the energy associated with it. This instability is favored over that of the

## MECHANISMS OF MAGNETIC FIELD RECONNECTION



### TEARING MODES IN A TWISTED CORONAL ARCH



### RECONNECTION IN A CURRENT SHEET BETWEEN AN EMERGING ARCH AND A PRE-EXISTING ARCH

Figure 2-1. Schematic diagrams of two magnetic field annihilation mechanisms. Shading indicates the locations of heating and energetic particles that result from the energy release.

current sheet because the energy release rate of some tearing modes is sufficiently large to explain flares, whereas current sheet models have difficulty explaining the energy release rate of even a small flare (Brown and Smith 1980). According to Spicer (1976), tearing modes are likely to release energy near the apex of a twisted arch. The observations from Skylab of flares in soft X rays suggest that energy is released in single arches, or in a series of arches, known as an arcade. These observations, and the derived density values mentioned in Section 2.1 suggest that the energetic electrons responsible for hard X-ray and microwave emissions acquire their high energies as a result of tearing modes near the tops of coronal arches. A review of the present status of the tearing mode model for primary energy release in a twisted arch is given by Van Hoven (1981).

It is stressed that field annihilation via the tearing mode mechanism for flare energy release remains a hypothetical explanation, because adequate information about the dynamics of fields in the corona during flares is lacking. Changes in the active region field configurations during flares have been reported by many observers, but there is still disagreement about whether these changes are actually the signature of the field annihilation that powers the flares (cf. Rust 1976). It has not even been demonstrated that, in the course of a particular flare, a measured amount of flux was annihilated throughout a known volume, and that the corresponding quantity of energy appeared in the form of flare emissions or in some other form, such as mass motions. Until such a demonstration is made, doubt will remain about the nature of the flare energy source; nevertheless, reconnection is the most likely energy release process, given present knowledge.

## 2.3 Hard X Rays

### 2.3.1 Phenomenology of Impulsive Hard X-ray Bursts

As mentioned in the Introduction, the distinction between impulsive and gradual bursts is commonly made. Since the focus in this work is on the impulsive component of flares, the characteristics of the gradual components are not considered here.

Impulsive bursts vary greatly in temporal structure and amplitude. Simple "spikes" in the time history occur, and combinations thereof. It is widely believed that individual spikes are in some sense elementary events, and it has been suggested that more complex flares are made up of series of "simple" disturbances which occur in the same or different regions (e.g. van Beek, de Feiter, and de Jager 1974; de Jager and de Jonge 1978; Crannell et al. 1978; Karpen, Crannell, and Frost 1979). Figure 2-2 illustrates an event chiefly composed of impulsive features. Complex events are not uncommon, in which impulsive and gradual features are both evident. The tail in Figure 2-2, beginning at about 0955:25 UT, might be characterized as a gradual component.

The spectra of hard X-ray bursts are usually measured with scintillation spectrometers. The observed pulse height spectra are usually consistent with the assumption that the incident photon spectrum can be described by either a power law or a thermal bremsstrahlung functional form. (The physical basis for assuming either form lies in the choice of a model for the source electron distribution. Models are discussed in detail in Section 2.3.3.) Each of these functions is a two-parameter function of photon energy,  $\epsilon$ . The power law used in

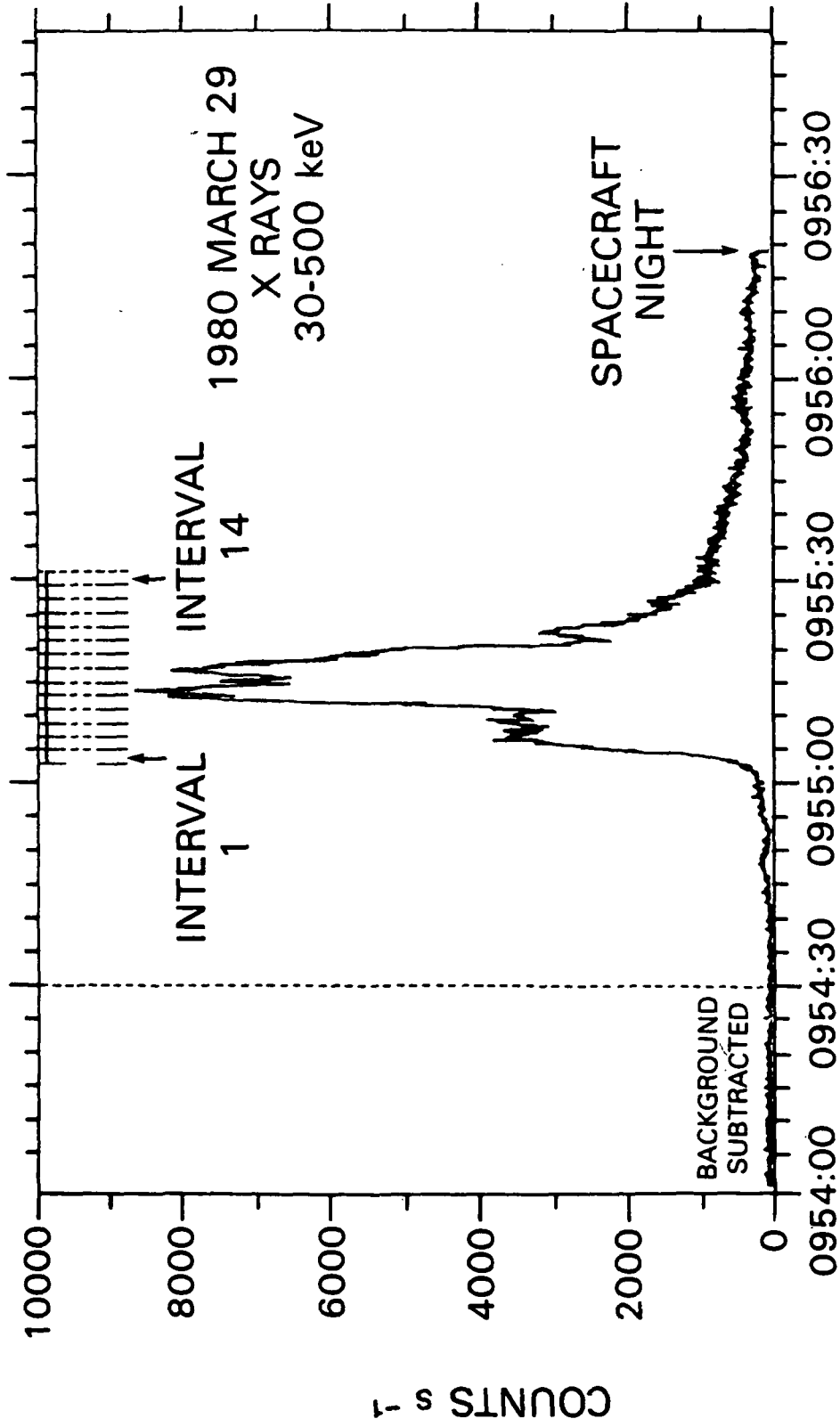


Figure 2-2. Time history of an impulsive hard X-ray burst, divided into 14 time intervals for dynamic spectral analysis. Resulting spectra are presented in Figure 2-3.

analysis of HXRBS data is

$$I(\varepsilon) = K_\gamma (\varepsilon/50 \text{ keV})^{-\gamma}, \quad (2.1)$$

where  $I(\varepsilon)$  is the differential X-ray flux in photons  $\text{cm}^{-2} \text{s}^{-1} \text{keV}^{-1}$ ,  $K_\gamma$  is the observed differential flux at 50 keV,  $\varepsilon$  is the photon energy in keV, and  $\gamma$  is called the spectral index of the photon spectrum.

The thermal bremsstrahlung function used in analysis of HXRBS data is

$$I(\varepsilon) = K_T \varepsilon^{-1} T^{-1/2} G_g \exp[-(\varepsilon - 50 \text{ keV})/T], \quad (2.2)$$

where  $K_T$  is a fitting parameter,  $T$  is the temperature in keV,  $G_g$  is the total effective Gaunt factor (Tucker 1975; Crannell *et al.* 1978). The electron temperature in deg K is denoted herein by  $T_e$ , and is given by  $T_e = 1.16 \times 10^7 T$ . For the energies and temperatures considered,  $G_g$  is a factor of order unity, which can be derived from the cross section for emission of hard X rays (*cf.* Karpen 1980). It is discussed more fully in Section 2.3.4. In the case of the thermal bremsstrahlung function, the thermal emission measure  $\mu$  is also of physical interest. The emission measure,  $\mu$ , is defined as  $n_e^2 V$ , where  $n_e$  is the electron number density in the source in  $\text{cm}^{-3}$ , and  $V$  is the source volume in  $\text{cm}^3$ . It is related to the parameters characterizing the thermal bremsstrahlung function by the following expression:

$$\mu = 9.3 \times 10^{41} K_T \exp(50 \text{ keV}/T). \quad (2.3)$$

A note of caution: a source composed of several components with different temperatures may give rise to a power-law spectrum within a limited energy range (Chubb 1972; Brown 1974). Conversely, nonthermal acceleration mechanisms can give rise to exponential spectra that are indistinguishable from a thermal spectrum (cf. Kaplan, Pikel'ner, and Tsytovich 1974).

To illustrate the typical dynamic spectral characteristics of these bursts, the impulsive phase of the flare shown in Figure 2-2 is divided into 14 time intervals, each 2 s in duration. Hard X-ray spectra for selected intervals are shown in Figure 2-3. The curves represent the best fit thermal bremsstrahlung function for each interval selected.

Typical values of  $T$  range from  $\sim 10$  to  $50$  keV ( $T_e$  from  $\sim 10^8$  to  $\sim 5 \times 10^8$  K). The thermal emission measure  $\mu$ , typically ranges from  $\sim 10^{44}$  to  $\sim 10^{46}$  cm $^{-3}$ . Values of  $\gamma$  typically range from  $\sim 3$  to  $\sim 6$ .  $K_\gamma$  typically ranges from  $0.01$  to  $10$  photons cm $^{-2}$  s $^{-1}$  keV $^{-1}$ .

The time history of fitted temperature,  $T$ , for this flare is shown in Figure 2-4. The flare represented in Figure 2-2 reached the unusually high temperature of  $80$  keV. The time history of  $T$  is usually similar to the X-ray and microwave time histories. An analogous relationship is found between intensity and fitted  $\gamma$  is found when spectra of impulsive features are analyzed with the power-law fitting function. In either case, the hardest spectra (minimum  $\gamma$  or maximum  $T$ ) are associated with peaks in intensity. The hardest spectrum during a peak may not be exactly coincident in time with the maximum intensity, however. In some spike bursts, there is a progressive hardening throughout the spike, while in others the maximum hardness precedes the maximum intensity. It is, nevertheless, most common for

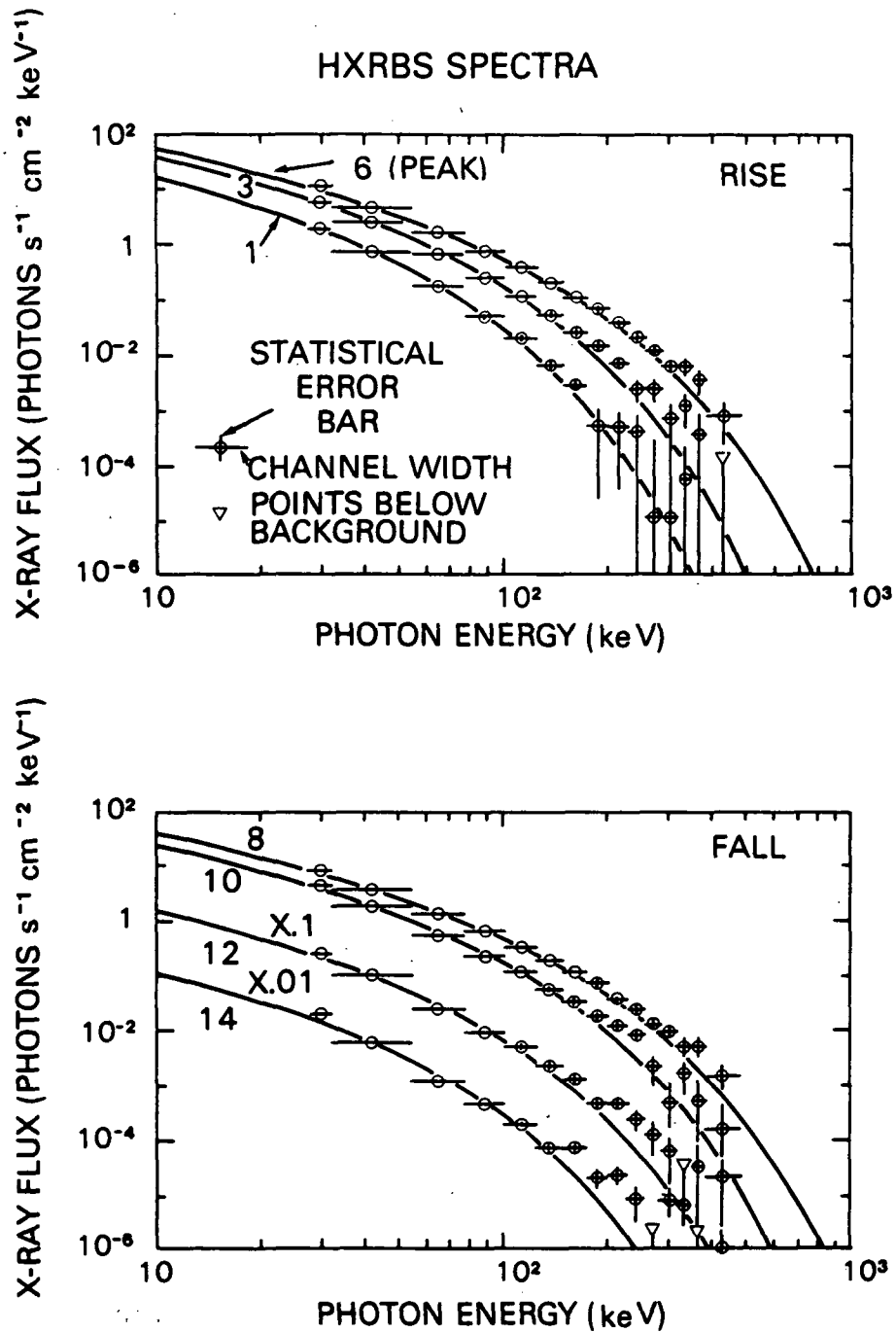


Figure 2-3. Dynamic spectra of the hard X-ray burst shown in Figure 2-2. The best-fit thermal bremsstrahlung function for each spectrum is indicated by a curve, labeled by the number of the interval.

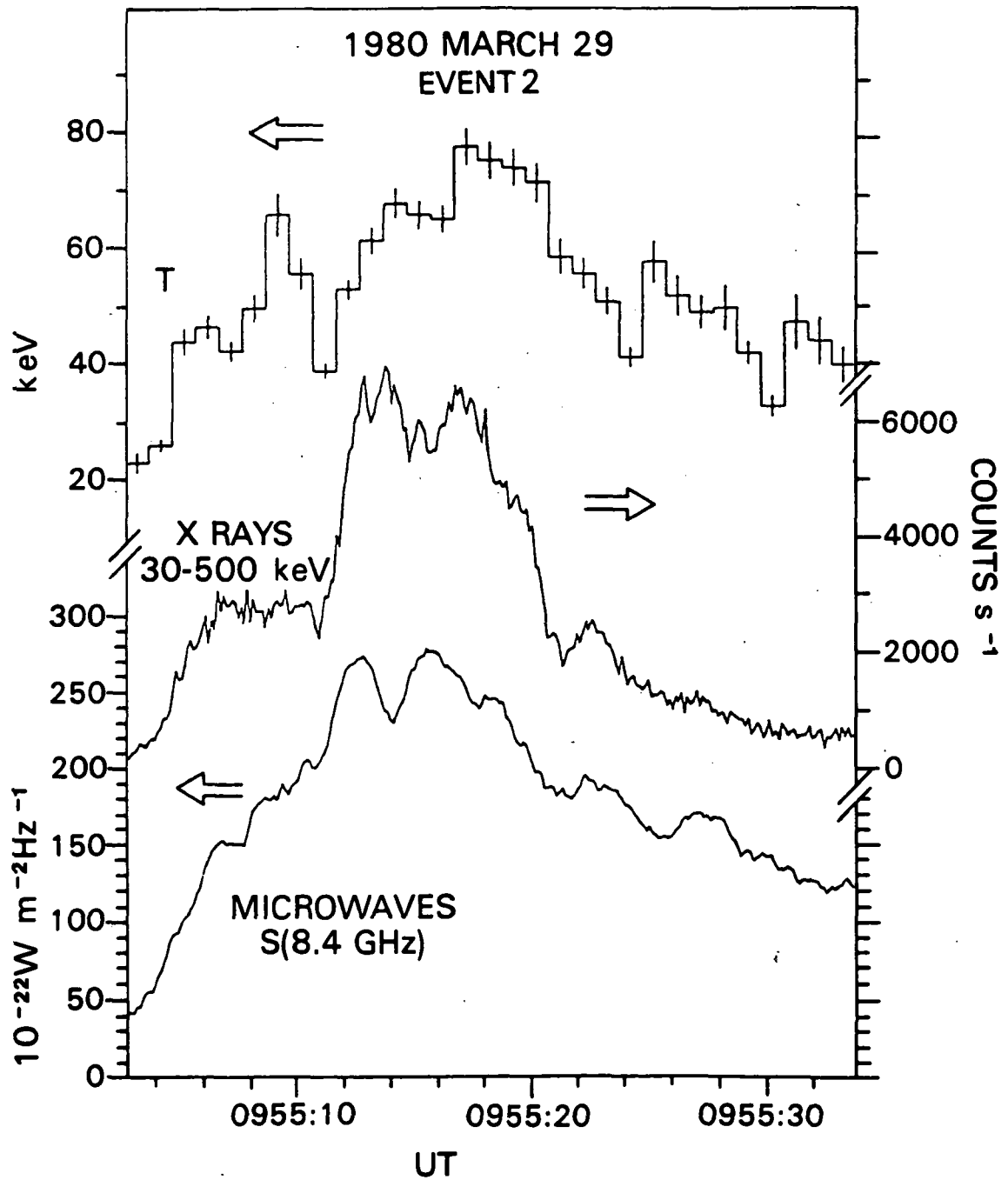


Figure 2-4. Time histories of fitted temperature, X-ray counting rate, and microwave flux for the flare shown in Figures 2-2 and 2-3.

the maximum hardness during an impulsive rise to occur within a second or two of the maximum intensity. Additional examples of this can be seen in Figures 5-1, 5-2, and 5-3.

It should be noted that the hardest spectrum evinced by a given flare may not be produced during an impulsive feature at all. It may be during a gradual decline, if the event has one. In complex events, an impulsive feature is usually associated with a temporary maximum in hardness, as measured by  $T$  or  $\gamma$ .

A comparison of spectral fits to the same measured pulse height spectrum with the thermal and power-law functions is shown in Figure 2-5. One can decide whether one or both of the two assumed functional forms are acceptable representations of the observations, or whether neither is acceptable, on the basis of the value of  $\chi^2$  obtained from the least squares fitting procedure (Bevington 1969). This fitting procedure can be used to determine the parameters characterizing the function of the assumed form (thermal or power-law) which gives the minimum value of  $\chi^2$ , taking into account the estimated uncertainties in instrument response, and statistical uncertainties due to random fluctuations in the count rates. This value of  $\chi^2$  can be used to calculate  $P(>\chi^2)$ .  $P(>\chi^2)$  is defined as the probability that, if the true spectrum were of the assumed form and measured with the given uncertainties, one would obtain a value of  $\chi^2$  greater than or equal to the observed value. The smaller the resultant probability, the less acceptable is the assumed representation of the data. The criterion adopted here for an acceptable fit is  $P(>\chi^2) \geq 0.1$ . For the case of Figure 2-5, the thermal function is acceptable, with  $P(>\chi^2) \approx 0.1$ , but the power law is not, with  $P(>\chi^2) \approx 10^{-3}$ .

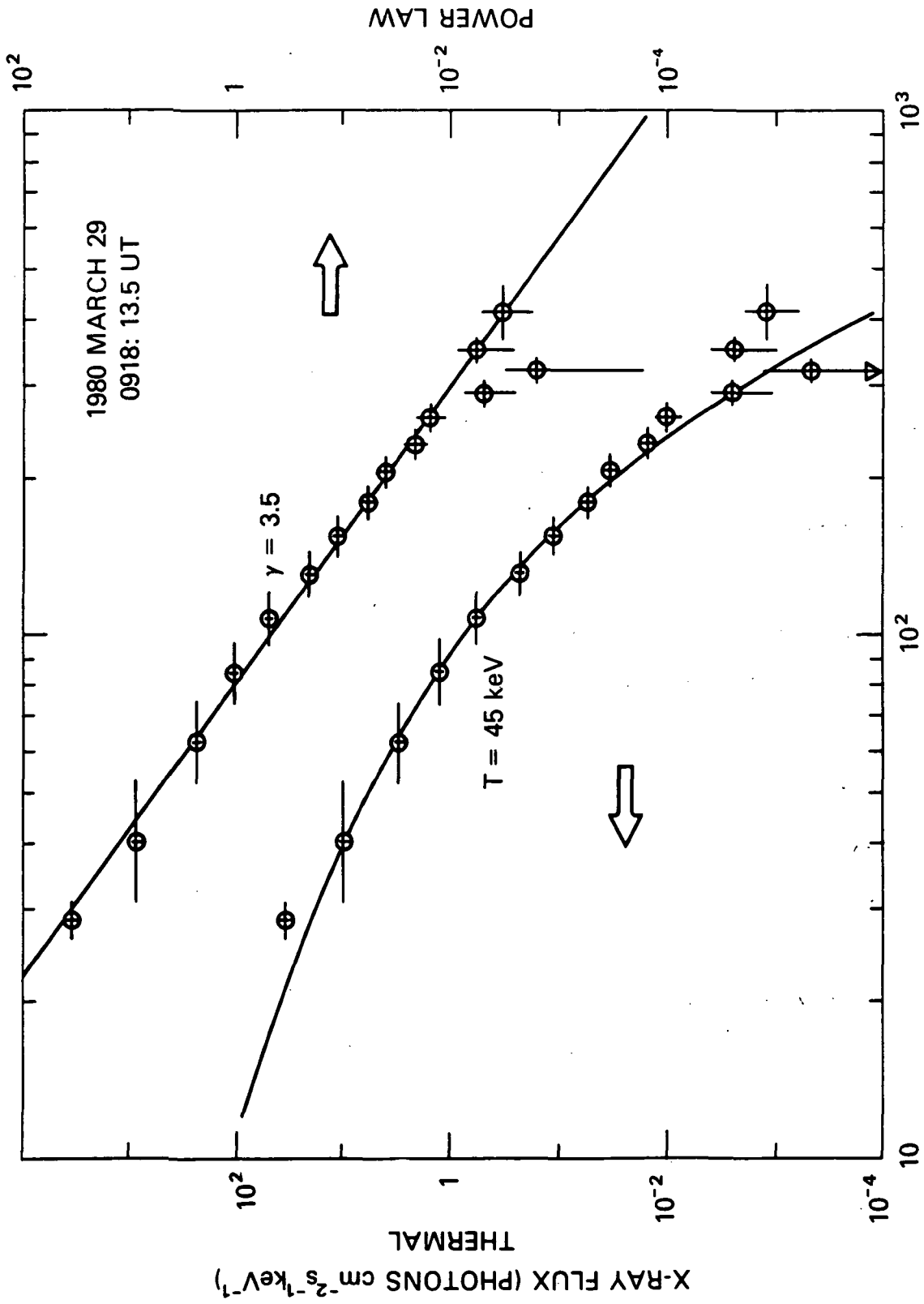


Figure 2-5. Comparison of best-fit power law and best-fit thermal function for the same pulse height spectrum. (From Wiehl et al. 1983.)

In many references, it is stated without qualification that flare hard X-ray spectra are power laws. This belief survives from the early days of observations with limited spectral range and less reliable counting statistics than are available today; under the early observational limitations, a straight line on a plot of  $\log I$  vs.  $\log s$  was considered to be an acceptable fit to the spectrum (cf. Kane 1974). It was pointed out by Chubb (1972), however, that a thermal bremsstrahlung function was an equally good representation in many cases. In fact, when the  $\chi^2$  test is applied to more recent spectra, obtained with better instruments, most of the spectra at the time of burst maximum are better fit by thermal functions than power laws (Crannell *et al.* 1978; Elcan 1978; Wiehl *et al.* 1983). X-rays with energies  $> 30$  keV are also commonly referred to as nonthermal, despite the fact that thermal models for the origin of this emission are still under active consideration. (For a discussion of hard X-ray emissions from an exclusively nonthermal standpoint, see Svestka 1976.) As mentioned previously, a power-law form of the spectrum is not sufficient to establish a nonthermal origin of the emission; nor does an exponential fall-off establish that the emission must be thermal.

The functional form of the spectrum changes during a flare in a way that is as unpredictable as the occurrence of flares. There seems to be a tendency for spike bursts to begin with a thermal form, which may persist until after the peak intensity, and to develop a power-law form during the intensity decline. This can be seen for the case of the dynamic spectrum shown in Figure 2-3. Such behavior should not be regarded as universal, however.

The spatial structure of hard X-ray sources is known for only a few

flares. Images have been provided in the 16 - 30 keV range by the Hard X-ray Imaging Spectrometer (HXIS) on SMM, and over various parts of the 17 - 60 keV range by the Solar Hard X-ray Telescope (SXT) on the Japanese Hinotori spacecraft. (HXIS is described in detail by Van Beek et al. 1980, and SXT is described by Makishima 1982.) The resolution of these images is  $\approx 10$  arc seconds, corresponding to  $\approx 7000$  km at the Sun. Much structure is probably still unresolved in these images; optical observations reveal unresolved structures in active regions at the limit of seeing,  $\sim 1$  arc seconds. Observations of 10 impulsive flares from SXT revealed single, compact sources in almost all cases (Takakura et al. 1983). In a few instances, nearly simultaneous impulsive brightenings occur at separate locations (Hoyng et al. 1981; Duijveman, Hoyng, and Machado 1982; Tsuneta 1983). This may be a manifestation of a diversity in hard X-ray source morphology.

### 2.3.2 The Emission Process — Bremsstrahlung vs. Alternatives

Before the first observations of hard X rays from the Sun, high-energy electrons were observed in interplanetary space in association with flares. Peterson and Winckler (1958, 1959) reported the first observation of a hard X-ray burst from the Sun, and interpreted the emission as bremsstrahlung from energetic electrons. Other processes have been proposed: synchrotron radiation from highly relativistic electrons (Guseinov 1963; Stein and Ney 1963), and inverse Compton radiation from interactions between flare-associated infrared photons and relativistic electrons in the flare region (Gordon 1960; Shklovskii 1964, 1965; Zheleznyakov 1965). If there were enough

relativistic electrons in the source to produce the hard X rays by synchrotron emission, then radio and optical emission much in excess of the observed intensities also would be produced (Svestka 1976). Synchrotron emission, as a primary source, can, therefore, be ruled out. Korchak (1965, 1967, 1971) showed that the inverse Compton effect is important only for ion densities  $n_i \lesssim 10^8 \text{ cm}^{-3}$ , more than an order of magnitude less than the density currently expected in the flare region. These considerations eliminate all but bremsstrahlung as likely sources of hard X-ray emission during flares (cf. Acton 1964; Brown 1976).

Bremsstrahlung ("braking radiation") is produced by fast charged particles when they undergo acceleration. In a solar flare, the dominant source of bremsstrahlung is the acceleration experienced by electrons during Coulomb collisions with atomic nuclei of the ionic component of the plasma. This is referred to as electron-ion bremsstrahlung. For non-relativistic electron energies, electron-electron bremsstrahlung is a second-order process, because electric dipole emission is forbidden in electron-electron collisions. At relativistic energies, however, electron-electron bremsstrahlung becomes important also. Ion-ion bremsstrahlung is negligible at the energies considered here, because of the relatively low velocities of the more massive ions. In a single electron-ion Coulomb collision, the electric field of the ion accelerates the electron, changing its direction. Radiation is emitted with an intensity that depends on the scattering angle, the initial velocity of the electron, and the charge,  $Z$ , of the ion nucleus. The bremsstrahlung spectrum produced by a given distribution of electrons in a plasma is obtained by integrating over all possible collisions (cf. Tucker 1975; Brown 1971). The

bremsstrahlung spectrum of a flare is, therefore, a function of the ion density and isotopic composition, as well as the electron density and energy distribution.

### 2.3.3 Models of the Bremsstrahlung Source

Excellent reviews of the many models that have been proposed for the origin of impulsive hard X-ray bursts are given by Kane (1974), Brown (1975, 1976), Svestka (1976), Melrose and Brown (1976), Rust and Emslie (1979), Sturrock (1980), and Brown and Smith (1980). Of the many models in the literature, there are three that command the most theoretical attention and are employed most often in interpretation of observations: the thick-target beam model, the trap-plus-precipitation model, and the thermal emission model with conduction front confinement. In the first two models, the source electron distribution is assumed to be an accelerated, nonthermal population, interacting collisionally with a relatively cool background distribution of thermal electrons and ions. In the thermal model, the source electron distribution is assumed to be collisionally relaxed; for this situation, there is no separate, background plasma, and the source electrons interact with each other and with the ions. Lack of information about the energy release mechanism and the plasma processes that the resulting energetic electrons undergo has prevented theorists from determining whether the source distribution is necessarily thermal or nonthermal. The observations of hard X-ray spectra do not provide a definitive test of this question because the spectral forms observed are consistent with either a thermal or nonthermal source population (cf. Brown 1974; Kaplan, Pikel'ner, and

Tsytovich 1974). This issue has been the cause of controversy for more than 20 years. The results of the analysis in Chapter V of this work bear upon the resolution of the controversy by providing evidence for the thermal model. For purposes of comparison, a description of the basic physics of the competing models is given in the following sections.

#### 2.3.4 Nonthermal Thick-target Model

Many investigators have been involved in the development of the thick-target model (de Jager and Kundu 1963; Arnoldy, Kane, and Winckler 1968; Acton 1968; Brown 1971; Hudson 1972; Syrovatskii and Schmeleva 1972; Petrosian 1973; Brown and McClymont 1974). In this model, it is postulated that energy is deposited in the source electrons by means of an unspecified acceleration mechanism, yielding an electron distribution characteristic of the mechanism. This distribution is usually assumed to be a power law in electron kinetic energy,  $E$ , given by

$$f(E) = A E^{-\delta}, \quad (2.4)$$

where the real number,  $\delta$ , is called the spectral index of the distribution,  $f(E)$  has the units electrons  $\text{cm}^{-3} \text{keV}^{-1}$ , and  $A$  is a constant. The assumption of a power-law electron distribution is justifiable because such a distribution is produced by certain particle acceleration mechanisms (e.g. Kaplan, Pikel'ner, and Tsytovich 1974), and because of the evidence for power-law distributions in other astrophysical sites of particle acceleration, such as supernova

remnants, cosmic rays, and radio galaxies. For explaining solar flares, values of  $\delta$  of physical interest are greater than 3. This form of the distribution function can only apply for a limited range in  $E$  since, at  $E = 0$ , the function is singular. Consequently, it must be assumed that there is a low-energy cut-off,  $E_0$ , below which the distribution is zero or has some well-behaved form.

The nonthermal electrons are assumed to be accelerated in the corona by the flare energy release mechanism, in a region connected to the chromosphere by magnetic field lines (see Figure 2-1). The electrons are then assumed to stream down along the field lines, or "precipitate", into a "target" region of relatively high density. The streaming electrons must form a dilute beam in order for the streaming to be stable; that is, the total density of nonthermal electrons,  $n_{nt}$ , must be a small fraction of  $n_0$ , the mean density of coronal background protons. There also must be a return current of the coronal background electrons, traveling in the opposite direction of the beam, which maintains charge neutrality (Benford and Book 1971; Melrose 1974; Hoyng, Brown, and van Beek 1976). (Because the plasma is electrically neutral,  $n_0$  is also a good approximation to the mean density of coronal background electrons.) In the target, the electrons lose energy in a time much shorter than the timescale of variations in the injection rate. This assumption is justified as follows. The energy loss timescale of a nonthermal electron, the time in which its energy drops to  $1/e$  of its original value, is  $\tau_1 \approx 2 \times 10^8 E^{3/2} / (\gamma n_t)$ , where  $n_t$  is the density of protons in the target (Hoyng, Brown, and van Beek 1976). If the target is assumed to be chromospheric matter of density  $\sim 10^{12} \text{ cm}^{-3}$ , then electrons with energies of order 100 keV will stop in the

target in less than 0.1 s. Because the typical timescale of variations in impulsive emission is much longer (of the order of seconds), these variations are attributed to the injection rate. The emerging X-ray photon spectrum then depends only on the distribution of injected electrons.

Because the plasma is mostly hydrogen, the Bethe-Heitler cross section for hydrogen can be used to compute the bremsstrahlung spectrum in the nonrelativistic energy range (Heitler 1954). It was shown by Brown (1971) that if the electron distribution is given by Equation (2.4), then the photon spectrum can be computed analytically, and is also a power law. If the observed photon spectrum is  $I(\epsilon) = a \epsilon^{-\gamma}$ , then the following relations hold:

$$\delta = \gamma + 1, \quad (2.5)$$

$$F(E_0) = 2.6 \times 10^{33} a (\gamma - 1)^2 B[\gamma - (1/2), 1/2] E_0^{-\gamma}, \quad (2.6)$$

where  $E$  and  $\epsilon$  are in keV,  $F(E_0)$  is the flux of electrons with  $E > E_0$  into the thick target, in electrons  $s^{-1}$ , and  $B(x, y)$  is the beta function. Since typical values of  $\gamma$  are  $\gtrsim 3$ , the free parameter  $E_0$  has a strong effect on the value of  $F(E_0)$ . A low-energy cut-off of 16 keV is adopted in the analysis of HXIS data (e.g. Hoyng et al. 1981). Observations suggest that  $E_0$  may be 10 keV or lower in some cases (Kahler and Kreplin 1971).

The thick-target model has been used to interpret many flare observations, perhaps more than any other flare model (e.g. Hoyng, Brown, and van Beek 1976; Benz 1977; Marsh et al. 1981; Hoyng et al.

1981; Duijveman, Hoyng, and Machado 1982; Hoyng et al. 1983). Use of the thick-target model leads to problems that call these interpretations into question, however. First, the theoretical problem of finding a mechanism to accelerate such a number of electrons in the required time has not been solved. Secondly, the model requires excessively large numbers of nonthermal electrons to explain a large flare, as shown by the following example. Every accelerated coronal electron is assumed to precipitate into the target. The total number of nonthermal electrons accelerated during the flare can be obtained by integrating the instantaneous value of  $F(E_0)$  for the duration of the flare. For the flare of 1972 August 4, Hoyng, Brown, and van Beek (1976) showed that  $4 \times 10^{39}$  nonthermal electrons with energies greater than 25 keV, carrying a total energy of  $2 \times 10^{32}$  erg, were necessary to explain the hard X-ray emission by means of the thick-target model. (Both of these values increase by a factor of 10 if the nonthermal electron distribution is assumed to extend as low as 10 keV.) To be stable, the beam of accelerated electrons would have to be dilute, with a density of electrons in the nonthermal tail,  $n_{nt} \sim 0.01 n_0$  (Hoyng, Brown, and van Beek 1976). This means that approximately  $4 \times 10^{41}$  electrons would have to be involved. It is generally assumed that the beam originates in the corona, which begins at 1.003 Solar Radii from the center of the Sun. At this distance, the density is approximately  $10^9 \text{ cm}^{-3}$ , and decreases steeply with increasing radius. The requirements on the beam and its dilution, therefore, imply that all of the electrons in the corona, out to 2 Solar Radii, would be involved. About half of these electrons are contained in a shell 0.1 Solar Radii thick. In contrast, interferometric microwave observations of flares indicate that source

sizes are consistent with those of active region structures (cf. Enome, Kakinuma, and Tanaka 1969). Thus the thick-target model cannot account for flares of the size of the 1972 August 4 flare.

Another obstacle to accepting the thick-target interpretation of hard X rays has been encountered recently by Brown et al. (1983a). The assumptions of the thick-target beam model lead to the prediction of a specific height structure of the emitting region, due to the variation of electron range with energy. Brown et al. (1983a) predict values of the ratio of hard X-ray flux from the upper part of the source to the flux from the entire source. The predicted values depend only on the atmospheric column density in the upper region and observed photon energy. The predicted ratio was compared with observed flux ratios which were available for five flares. In each of these five cases, the flare was observed with instruments on two spacecraft, the International Sun-Earth Explorer-3 and Pioneer Venus Orbiter. The occultation ratio could be obtained at 150 and 350 keV because, in each case, the solar limb occulted the lower part of the source, as observed with one spacecraft, but the entire source was observed with the other spacecraft. Allowance was made for the possible time dependence of the column density during the flare. Brown et al. (1983a) showed that the detailed, quantitative dependence of the ratio on height, energy, and time are not consistent with the thick-target model, as presently formulated. A reformulation of the model, including additional interactions between the beam electrons and the atmosphere might eliminate the discrepancy, but would increase the required number and energy of electrons.

Another model parameter of considerable interest is the efficiency

of bremsstrahlung emission, which, for this model, can be calculated as follows. The great majority of nonthermal electrons that contribute to hard X-ray emission are nonrelativistic. The primary processes by which nonrelativistic electrons lose energy are ionization and Coulomb collisions with the background thermal electrons. Brown (1971) has argued that the medium is completely ionized, so that ionization losses can be neglected. The rate of energy loss to Coulomb collisions by a nonrelativistic electron is (Brown 1971)

$$(dE/dt)_{cc} = - 55.7 \pi e^4 n_0 v / E , \quad (2.7)$$

where  $v$  is the electron velocity. Bremsstrahlung emitted by these nonrelativistic electrons is primarily electron-ion bremsstrahlung, and the rate of energy loss suffered an electron of energy  $E$  in the process of emission is

$$(dE/dt)_{ei} = - n_0 v \int_0^E Q_s \varepsilon d\varepsilon , \quad (2.8)$$

where the differential cross section for electron-ion bremsstrahlung,  $Q_s$ , is given by (Heitler 1954)

$$Q_s = - \frac{8}{3} \frac{r_0^2}{137} \frac{m_e c^2}{sE} \ln \left[ \frac{1 + (1 - \varepsilon/E)^{1/2}}{1 - (1 - \varepsilon/E)^{1/2}} \right] . \quad (2.9)$$

In this expression,  $r_0$  is the classical electron radius, defined by the expression  $r_0 \equiv e^2/m_e c^2$ . The efficiency of bremsstrahlung emission for a nonrelativistic electron is

$$\eta(E) = (dE/dt)_{ei} / (dE/dt)_{cc} . \quad (2.10)$$

Making the substitutions and performing the integration yields

$$\eta(E) \approx 2 \times 10^{-4} E / m_e c^2 . \quad (2.11a)$$

For example, only 2 parts in  $10^5$  of the energy of a 50-keV electron are transformed into bremsstrahlung photons.

At relativistic energies, the efficiency is no longer given by Equation (2.11a). This is because electron-electron bremsstrahlung contributes to the emission, the emission cross section changes to the relativistic form, and additional loss processes come into play. The contribution of electron-electron bremsstrahlung is discussed by Akheizer and Berestetskii (1965) and Maxon and Corman (1967).

Unfortunately, no closed analytical formula is available for the total bremsstrahlung cross section in the energy range for which  $E \sim m_e c^2$ . The total bremsstrahlung production has been calculated numerically by Bai (1977) for a power-law electron distribution. Bai shows that electron-electron bremsstrahlung flattens the X-ray spectrum of a power-law electron distribution, reducing  $\gamma$  by about 1/2 for energies above a threshold that depends on  $\delta$ . The threshold energy varies from approximately 300 to 600 keV, as  $\delta$  varies from 2 to 5.

Simple formulae for the total bremsstrahlung emission rate and the other loss processes are available for the ultra-relativistic energy range, and the bremsstrahlung efficiency for the energy range between the nonrelativistic ( $E \ll m_e c^2$ ) and ultra-relativistic ( $E \gg m_e c^2$ ) ranges can be estimated by interpolation.

For ultra-relativistic electrons, most of the thick-target energy loss occurs in dense, low-altitude layers of the solar atmosphere, with  $n_0 \gtrsim 10^{13} \text{ cm}^{-3}$  (Brown 1973). In these layers, the ionized fraction of the atmosphere is negligibly small for the purpose of the following calculations. The energy loss processes for ultra-relativistic electrons are ionization, bremsstrahlung radiation, inverse Compton scattering, and synchrotron radiation (Ginzburg and Syrovatskii 1964; Cheng 1972). At photospheric densities, inverse Compton scattering losses are insignificant in comparison with the other three processes for  $E < 10^6 \text{ keV}$ , and are not considered further here. The gas is mostly hydrogen, so that the ionization loss is given by

$$(dE/dt)_i = - 7.6 \times 10^{-12} n_0 (3 \ln [E/m_e c^2] + 20) , \quad (2.11b)$$

in the units  $\text{keV s}^{-1}$ . The bremsstrahlung radiation losses, including electron-electron and electron-ion bremsstrahlung, are given approximately by

$$(dE/dt)_b = - 5.1 \times 10^{-13} n_0 (E/m_e c^2) . \quad (2.11c)$$

Synchrotron radiation losses are given by

$$(dE/dt)_s = - 10^{-6} B_+^2 (E/m_e c^2)^2 , \quad (2.11d)$$

where  $B_+$  is the component of magnetic field perpendicular to the electron's trajectory. For the ultra-relativistic energy range,  $E \gg m_e c^2$ , the bremsstrahlung emission efficiency,  $\eta(E)$ , is

$(dE/dt)_b / (dE/dt)_{\text{total}}$ , where  $(dE/dt)_{\text{total}}$  is the sum of (2.11b), (2.11c), and (2.11d).

The competition of these energy loss processes leads to much more complex variations in the efficiency than in the nonrelativistic case. For example, with  $B_+ = 100$  G and  $n_0 = 10^{13}$  cm<sup>-3</sup>, ionization dominates the losses for  $5 \times 10^3$  keV  $< E < 3 \times 10^5$  keV. All three processes contribute about equally at  $3 \times 10^5$  keV. Above this energy, synchrotron losses are predominant. With  $B_+ = 1000$  G, however, bremsstrahlung losses are always less than 10% of the total, and synchrotron losses exceed ionization at about  $3 \times 10^4$  keV. The variation of efficiency with energy for each of these cases is illustrated in Figure 2-6. An individual electron becomes much more efficient at relativistic energies than at nonrelativistic energies.

The efficiency of an individual electron is, of course, not generally characteristic of the source as a whole (contrary to, for example, Smith and Lilliequist 1979, and Kiplinger *et al.* 1983). The entire source is properly characterized by the ratio of the total bremsstrahlung energy loss from the distribution to the total energy loss from the distribution by collisions:

$$\eta_{\text{tt}} = \frac{\int \eta(E) E f(E) dE}{\int E f(E) dE}, \quad (2.12)$$

where the integration is from  $E_0$  (the low-energy cut-off) to infinity. With the electron distribution given by Equation (2.4), and the use of the nonrelativistic efficiency in Equation (2.5), the result is

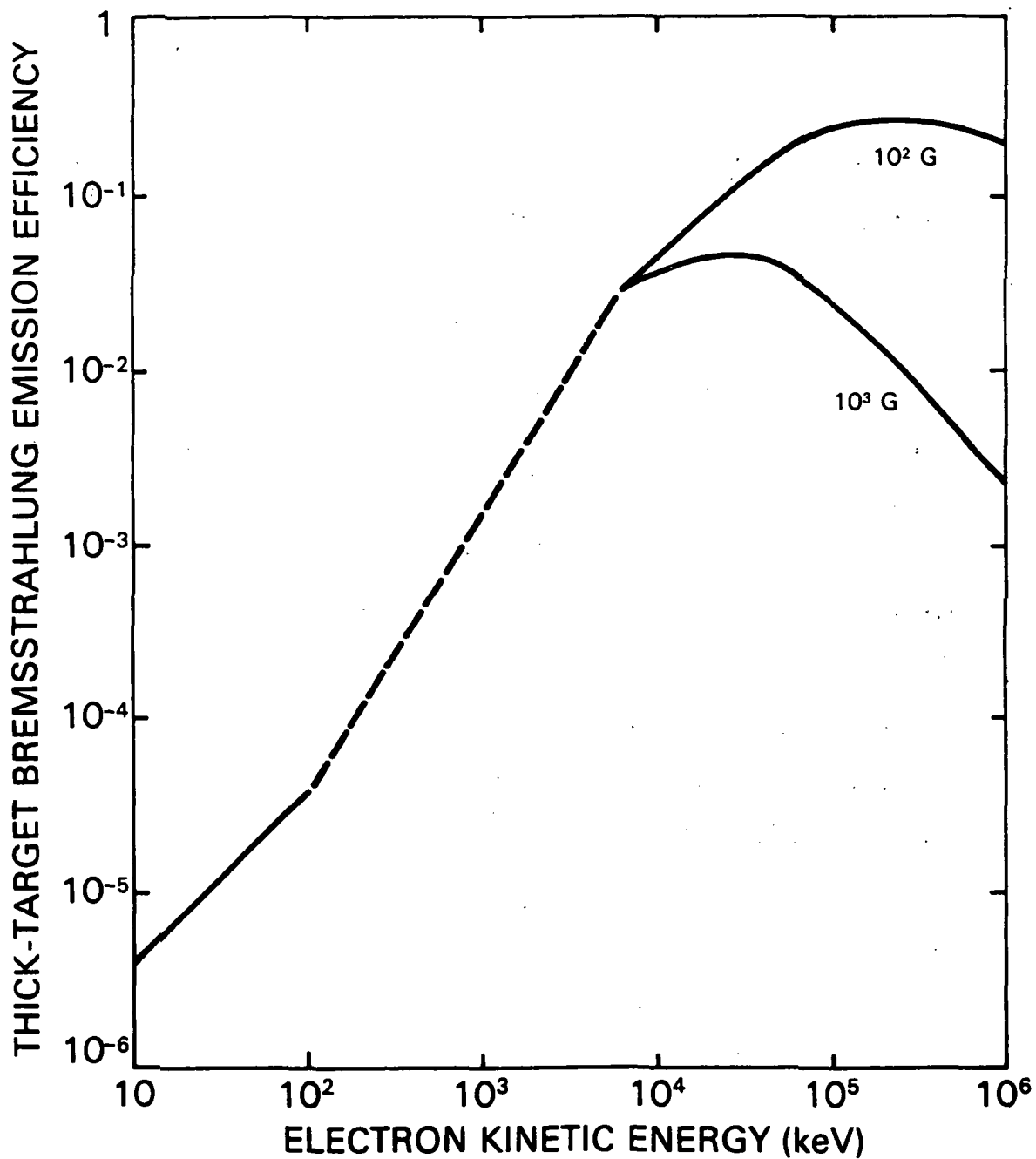


Figure 2-6. Efficiency of thick-target bremsstrahlung emission of an electron,  $\eta_{tt}$ , as a function of kinetic energy,  $E$ . The dashed part of the curve indicates the energy range in which both the nonrelativistic and ultrarelativistic approximations break down. Interpolation has been used to approximate the efficiency in this range.

$$\eta_{tt} = 2 \times 10^{-4} \frac{\gamma - 1}{\gamma - 2} \frac{E_0}{m_e c^2} . \quad (2.13)$$

Equation (2.13) is accurate to within 30% for  $\gamma > 3$  ( $\delta > 4$ ), which holds for almost all flares observed with the HXRBS. The nonthermal electron distribution is commonly assumed to extend as low as 16 keV (e.g. Hoyng et al. 1983). In such a case, the predominant contributions to the integral in the numerator of Equation (2.13) are made by the relatively numerous low-energy electrons. (It may be noted that the integrals converge in most cases of physical interest, because observed values of  $\gamma$  at nonrelativistic energies are generally greater than 2.) For the most energetic flares, however, the increase in efficiency in the relativistic range is important (see Figure 2-6). For  $\gamma < 3$ , Equation (2.13) is invalid, and the efficiency depends on the relativistic modifications of the bremsstrahlung cross section. Only one flare with  $\gamma \approx 2$  has been observed with HXRBS (1983 June 3). A few flares with  $\gamma$  as small as 2 have been observed with the Gamma Ray Spectrometer on SMM (D. Forrest, private communication).

The calculations by Hoyng, Brown, and van Beek (1976) of the total number of accelerated electrons required by the thick-target model for the 1972 August 4 flare were based on the same nonrelativistic approximations as Equation (2.13). For this event,  $\gamma$  was greater than 3 throughout all of the impulsive phase and much of the gradual decline, so that the estimates of the number of electrons and conclusions regarding the excessiveness of such a requirement should be valid.

Thus, in most cases, the efficiency of the source is explicitly

dependent upon the low-energy cut-off. For typical values of the parameters,  $\gamma = 3.5$  and  $E_0 = 16$  keV,  $\eta_{tt} = 10^{-5}$ .

The efficiency of a given flare model is a measure of the amount of energy that must be imparted to energetic electrons in order to account for the total energy emitted in the form of hard X rays. It would be naive to adopt or reject a model on the sole basis of its advantage in efficiency, relative to other possible models, because most processes in nature are inherently inefficient. Nevertheless, the efficiency of a model must be sufficient to produce the observed emission with a plausible number of electrons, or the model cannot be regarded as successful.

#### 2.3.5 Nonthermal Trap-plus-precipitation Model

The other nonthermal model that commands the most interest at present is the trap-plus-precipitation model. Coronal magnetic field configurations can serve to trap energetic particles, as first proposed by Takakura and Kai (1966). For instance, trapping occurs in a coronal arch such as those illustrated in Figure 2-1, due to the convergence of the magnetic field lines near the feet of the arch. This trapping is due to the conservation of magnetic moment, which is an adiabatic invariant of a charged particle trajectory in a magnetic field (cf. Boyd and Sanderson 1969; Krall and Trivelpiece 1973). The same mechanism of particle trapping is used in magnetic-bottle approaches to controlled thermonuclear fusion. Particle trapping by this mechanism also occurs in the Earth's Van Allen radiation belts.

As in the thick-target model, the particles are assumed to be

injected near the apex of an arch. Whether or not a particle is trapped depends on the pitch angle of the particle's initial trajectory. If  $v_x$  is the particle's component of velocity parallel to  $\vec{B}$ , and  $v_+$  is the component perpendicular to  $\vec{B}$ , then the pitch angle,  $\alpha$ , is defined by the relation  $\alpha \equiv \tan^{-1} (v_+/v_x)$ . In the absence of particle scattering, all particles with initial pitch angles greater than  $\alpha_0 = \sin^{-1} (B_{\text{apex}}/B_{\text{foot}})^{1/2}$  are reflected from the converging field. Particles with initial pitch angles less than  $\alpha_0$  (within the "loss cone") are not reflected, and precipitate into the chromosphere. The process of magnetic mirroring and other trapping processes are considered in more detail in Section 3.2.

Trapping of energetic electrons is a convenient explanation for hard X-ray and microwave emission observed from so-called "beyond-the-limb" flares. This term is used when it is known that only the coronal part of the flaring active region is visible to observers because the solar limb occults the dense, low-altitude parts of the active region (e.g. Frost and Dennis 1971; Roy and Datlowe 1975). Thick-target bremsstrahlung is generally assumed to originate in the dense matter of the low corona or chromosphere. In the case of a beyond-the-limb flare, thick-target bremsstrahlung from the dense layers cannot explain the observed emission.

The trap model was given additional credence when observations from Skylab revealed that soft X-ray emission from flares originates in arches located in the corona and chromosphere (e.g. Van Hoven *et al.* 1980). These observations made it more plausible that hard X-rays and microwaves might also originate in an arch-shaped trap.

Since the initial proposal of the trap model by Takakura and Kai

(1966), much theoretical effort has gone toward determining the observational consequences of trapping (Brown and Hoyng 1975; Brown and McClymont 1976; Melrose and Brown 1976; Emslie, McCaig, and Brown 1979). An important advance was the realization that precipitation of particles leaking from the trap is a necessary consequence of the model (Hudson 1972; Kane 1974; Melrose and Brown 1976). Thus, in addition to emission from the particles in the trap, thick-target emission from the precipitating particles must be accounted for. The model is now known as the trap-plus-precipitation model.

Melrose and Brown (1976) calculated the rate at which Coulomb collisions scatter the electrons in a trap into the loss cone, and derived the resulting hard X-ray spectrum, including emission from trapped and precipitating electrons. In the case of a power-law electron distribution, the hard X-ray spectrum is also a power law (Equation 2.1), characterized by

$$\gamma = \delta + 1/2 . \quad (2.14)$$

In addition to explaining beyond-the-limb flares, the trap-plus-precipitation model can account for fast variations of the X-ray and microwave spectra without requiring corresponding variations in the injection rate of nonthermal particles. This is because acceleration of trapped particles can be caused by perturbations in the trapping magnetic structure, independent of the injection of accelerated particles. For example, pulsations of an arch could be caused by the excitation of magnetohydrodynamic oscillations in the arch. The magnetic field oscillations that would occur in such a case would

modulate the electron energy distribution, and, in turn, the hard X-ray and microwave spectra. Repeated acceleration of the same trapped electron population, therefore, offers an alternative to the implausibly large number of electrons required in the thick-target model, in which it is assumed that each accelerated electron gives up its energy once and for all. A version of the trap model was proposed by Brown and Hoyng (1975), known as the betatron model, in which pulsations of a trap dominate the evolution of the electron distribution. Brown and Hoyng (1975) showed that data for the large X-ray burst of 1972 August 4 are consistent with the source electrons being trapped in a very large, vibrating coronal magnetic bottle. Independent observational evidence for such oscillations of coronal arches exists (e.g. Kattenberg and Kuperus 1983). The phenomenon appears to be rare, however, and does not appear to be a common mechanism of electron acceleration in impulsive flares. Karpen (1980, 1982) analyzed 20 complex impulsive bursts, and showed that the spectral evolution characteristic of the betatron model was not present in the impulsive phase of these flares. Thus, no evidence for reacceleration of electrons has been presented yet, except in the case of the 1972 August 4 flare. Even in such a case, the energy requirements remain very large, as in all nonthermal models (cf. Brown 1976).

The bremsstrahlung emission efficiency in a trap-plus-precipitation model is not considered here because of its complex dependence on the details of the structure and pulsations of the trap. Some of the emission occurs by thick-target processes while the rest is emitted less efficiently in "thin" target interactions, in which the emitting electrons do not lose all of their energy. Thus the source as a whole

converts electron energy into photons less efficiently than a thick-target source. While reacceleration of electrons in a trap-plus-precipitation model reduces the required number of accelerated electrons, the energy requirements are even larger than those of the thick-target model.

### 2.3.6 Thermal Models

As first shown by Chubb et al. (1966), observed hard X-ray spectra could be interpreted as thermal bremsstrahlung from a Maxwellian distribution of electrons with a temperature  $T_e$  of order  $10^8$  K. This interpretation was discounted, however, by Kahler (1971a,b) and others, on the following grounds. It was argued that coronal plasma at a temperature this high would cool on a timescale much shorter than observed burst timescales, due to the high thermal conductivity of the plasma and the nearness of the much cooler, dense photosphere (an effective heat sink, at a few thousand K). Implausible rates of energy release would be required to maintain a temperature consistent with the observations for burst timescales, in order to overcome the conduction loss rate. (Radiative cooling of the plasma would be negligible on impulsive burst timescales, as noted by Mätzler et al. 1978.) It also was argued that the plasma could not be collisionally relaxed because the Coulomb collision rate in a plasma of coronal density and  $T_e \sim 10^8$  K would be too low to produce thermal equilibrium. The close temporal relationship of the hard X-ray and microwave emissions was also used to argue in favor of a nonthermal nature of the hard X-ray source, because the microwave source electrons were believed to be

unquestionably nonthermal (cf. Svestka 1976).

The foregoing arguments have all been countered as understanding of the physical processes in high-temperature plasmas has advanced. Brown (1974) showed that the calculation of Kahler greatly overestimates the conduction losses, in part because of the temperature structure assumed for the plasma, and because plasma turbulence created by the gradients in temperature would be expected to reduce the conductivity dramatically. The turbulence would also serve to produce a Maxwellian distribution on the required timescales. Descriptions of processes that limit conduction losses and thermalize the electrons in a high-temperature plasma are given in Chapter III. In the remainder of this section, a thermal distribution of source electrons is assumed, and the consequences are described.

The differential X-ray flux from an optically-thin source of electrons with a Maxwellian distribution is given by the following expression (Tucker 1975; Crannell et al. 1978):

$$I(s) = 1.07 \times 10^{-42} \frac{g(s, T)}{s T^{1/2}} \left[ \sum \mu_i Z_i^2 \right] \exp(-s/T), \quad (2.15)$$

at a distance of  $150 \times 10^6$  km from the emitting region (1 astronomical unit). The function  $g(s, T)$  is called the average Gaunt factor, and accounts for the variation in contributions to the bremsstrahlung cross-section from free-free and free-bound interactions. The summation is over ionic species, and  $\mu_i$  is the emission measure in  $\text{cm}^{-3}$  of the ionic species with charge number  $Z_i$ . The emission measure is defined by the expression  $\mu_i \equiv n_e n_i V$ , where  $V$  is the volume of the emitting

region. From conservation of charge,  $n_e = \sum n_i Z_i$ . Following Groenschild and Mewe (1978), a solar abundance model with helium 8.5% as abundant as hydrogen was assumed, so that  $\sum n_i Z_i^2 = 1.355 n_e$ . The total effective Gaunt factor,  $G_g$ , is defined by the expression

$$G_g = (g_{ff} + g_{fb}) n_e^{-1} \sum n_i Z_i^2 . \quad (2.16)$$

$G_g$  was calculated through use of the expressions given by Matteson (1971), which were derived from calculations by Quigg (1967, 1968a,b). The free-free contribution to  $G_g$  is

$$g_{ff} \approx 1.04 (T/100 \text{ keV})^a (E/T)^{-b} , \quad (2.17)$$

where  $a = 0.125$  and  $b = 0.31 (T/100 \text{ keV})^{-0.190}$ . The free-bound contribution,  $g_{fb}$ , is approximately 0.08 for  $T \gtrsim 12 \text{ keV}$  (Mewe, private communication with Dennis). The total effective Gaunt factor is therefore

$$G_g = [1.41 (T/100 \text{ keV})^a (s/T)^{-b} + 0.11] n_e^{-1} . \quad (2.18)$$

Thus, recalling that  $\mu = n_e^{-2} V$ , Equation (2.15) can be rewritten as

$$I(s) = 1.07 \times 10^{-42} \frac{\mu G_g}{s T^{1/2}} \exp(-s/T) . \quad (2.19)$$

Comparison of this expression with Equation (2.2) shows that

$$K_T = 1.07 \times 10^{-42} \mu \exp(-50 \text{ keV}/T).$$

It should be noted that the above spectrum is characteristic of a source of uniform temperature. If the source comprises various regions in which local thermodynamic equilibrium prevails, it is necessary to characterize the source by means of  $d\mu(T_e)/dT_e$ , the differential emission measure as a function of temperature. The spectrum is then computed by integrating the contributions at various temperatures (Brown 1974). It has been shown that a source with even a small amount of non-isothermality exhibits a hard X-ray spectrum that is well-approximated by a power law over a wide range of energies (Brown 1974, 1978). Thus, the observation of a power-law spectrum is not sufficient to establish the presence of nonthermal electrons in the hard X-ray source.

The first thermal model to address the problem of the dynamics of hard X-ray emission was the adiabatic compression model of Crannell et al. (1978) and Mätzler et al. (1978). A homogeneous set of hard X-ray spike bursts was selected for analysis by Crannell et al. from flares observed with the Orbiting Solar Observatory-5 (OSO-5). Some of the properties of spike bursts that were reported are the following. The rise and fall times are approximately equal, suggesting that a reversible process is responsible for the evolution of the distribution of energetic electrons. The temperature maximum coincides approximately in time with the peak in emission. Spectra with sufficient counting statistics to study the correlation of  $T$  with  $\mu$  were available for two bursts. In the companion paper by Mätzler et al., it was shown that, as a function of time,  $t$ , during both the rise and the fall of a burst,  $\mu(t)$  was approximately proportional to  $T(t)^{3/2}$ . All of these

properties would be explained if a burst were produced by a reversible adiabatic compression and expansion of coronal plasma, perhaps due to a compressive disturbance propagating through plasma trapped in a magnetic bottle.

Although the adiabatic compression model explained the burst properties presented above, later analyses showed that the relationship between  $T$  and  $\mu$  during a flare was not usually consistent with the model (e.g. Elcan 1978; Wiehl et al. 1983). Thus, the adiabatic compression model cannot explain most bursts, and a model with more general applicability must be found, which can also explain the variety of  $(T, \mu)$  relationships observed.

The bremsstrahlung emission efficiency of the model is the ratio of the bremsstrahlung energy loss rate to the heating rate. The bremsstrahlung emissivity of a thermal source is (Tucker 1975)

$$j(T_e) = 2.4 \times 10^{-27} T_e^{1/2} n_e^2, \quad (2.20)$$

in the units  $\text{erg cm}^{-3} \text{ s}^{-1}$ . The heating rate is approximately  $3n_e kT_e/t$ , where  $t$  is the time, measured from the onset of heating. In particular, the efficiency of the thermal source at the time of peak hard X-ray emission,  $t_{\text{peak}}$ , is

$$\eta_{\text{ac}} \approx \frac{j(T_e)}{3 n_e kT_e} \approx 5.8 \times 10^{-12} T_e^{-1/2} n_e t_r, \quad (2.21)$$

where  $t_r$  is the rise time of the burst. For a typical case, with  $T_e = 3 \times 10^8 \text{ K}$ ,  $n_e = 3 \times 10^9 \text{ cm}^{-3}$ , and  $t_r = 5 \text{ s}$ ,  $\eta_{\text{ac}} = 5 \times 10^{-6}$ . This is to

be compared with the efficiency of a thick-target model of the same source,  $\eta_{tt}$ , given by Equation (2.14). The relative advantage in efficiency of the adiabatic compression model over the thick-target model is  $\eta_{ac}/\eta_{tt}$ , or

$$\xi \approx 1.3 \times 10^{-5} \frac{\gamma - 2}{\gamma - 1} \frac{n_e t_r}{T_e^{1/2} E_0} . \quad (2.22)$$

In this expression,  $\gamma$  is the best-fit power-law index of the hard X-ray spectrum at  $t_{peak}$ ,  $T_e$  is the electron temperature of the best-fit thermal bremsstrahlung function of the spectrum at the same time, and  $E_0$  is the low-energy cut-off in the assumed power-law electron distribution.

It is often stated categorically that thermal models are more efficient than nonthermal models. As Equation (2.22) shows, this statement should be qualified with reference to the density and temperature in question. For the typical case considered above,  $\xi$  is actually  $\approx 0.42 < 1$ .

An important element of any thermal model is the mechanism that confines the hot plasma and inhibits the heat conduction losses. This mechanism was never specified in applications of the adiabatic compression model, although magnetic confinement was proposed as one possibility. Magnetic bottles fail to confine particles with pitch angles in the loss cone, however, and are subject to other instabilities that lead to leakage. As shown by Melrose and Brown (1976) for the case of a nonthermal trap model, escape of electrons occurs in a trap model, leading to precipitation of the electrons which may dominate the hard

X-ray production. In the thermal case, this leakage might result in precipitation of electrons with a quasi-Maxwellian distribution into a thick target.

The thermal model proposed by Brown, Melrose, and Spicer (1979) and Smith and Lilliequist (1979) addresses the problem of confinement of the hot plasma. In this model, the confinement mechanism also plays a crucial role in determining the dynamics of the emission. The model is discussed in detail and developed further in Chapter III. The efficiency of hard X-ray emission in this model, as compared with the thick-target beam model, is also discussed.

## 2.4 Microwaves

### 2.4.1 Phenomenology of Impulsive Microwave Bursts

Microwave bursts during flares were first observed by Covington (1948, 1951). A comprehensive review of the early history of microwave observations and interpretations is given by Kundu (1965). The subject has been reviewed more recently by Krüger (1979).

What was said in Section 2.3.1 about the temporal structure of impulsive hard X-ray bursts also holds for the temporal structure of impulsive microwave bursts. As illustrated in Figures 1-1, 2-5, 5-1, 5-2, and 5-3, the evolutions of the two emissions usually correspond quite closely.

An example of the spectral evolution of a hard X-ray burst is given in Section 2.3.1. The dynamic spectrum of the coincident microwave burst is shown in Figure 2-7, the differential microwave flux,  $S$ , being

BERN OBSERVATORY DATA  
1980 MARCH 29

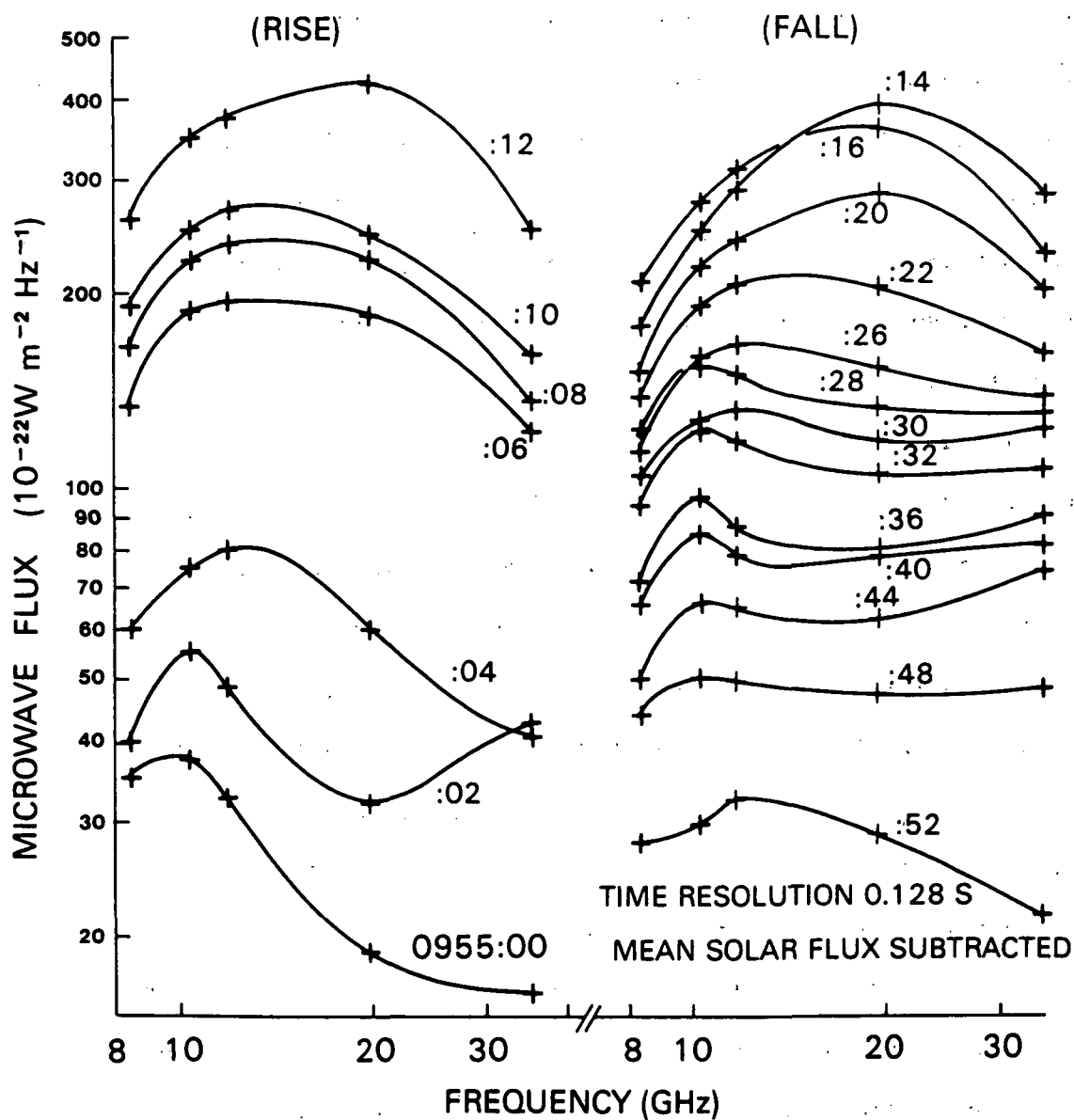
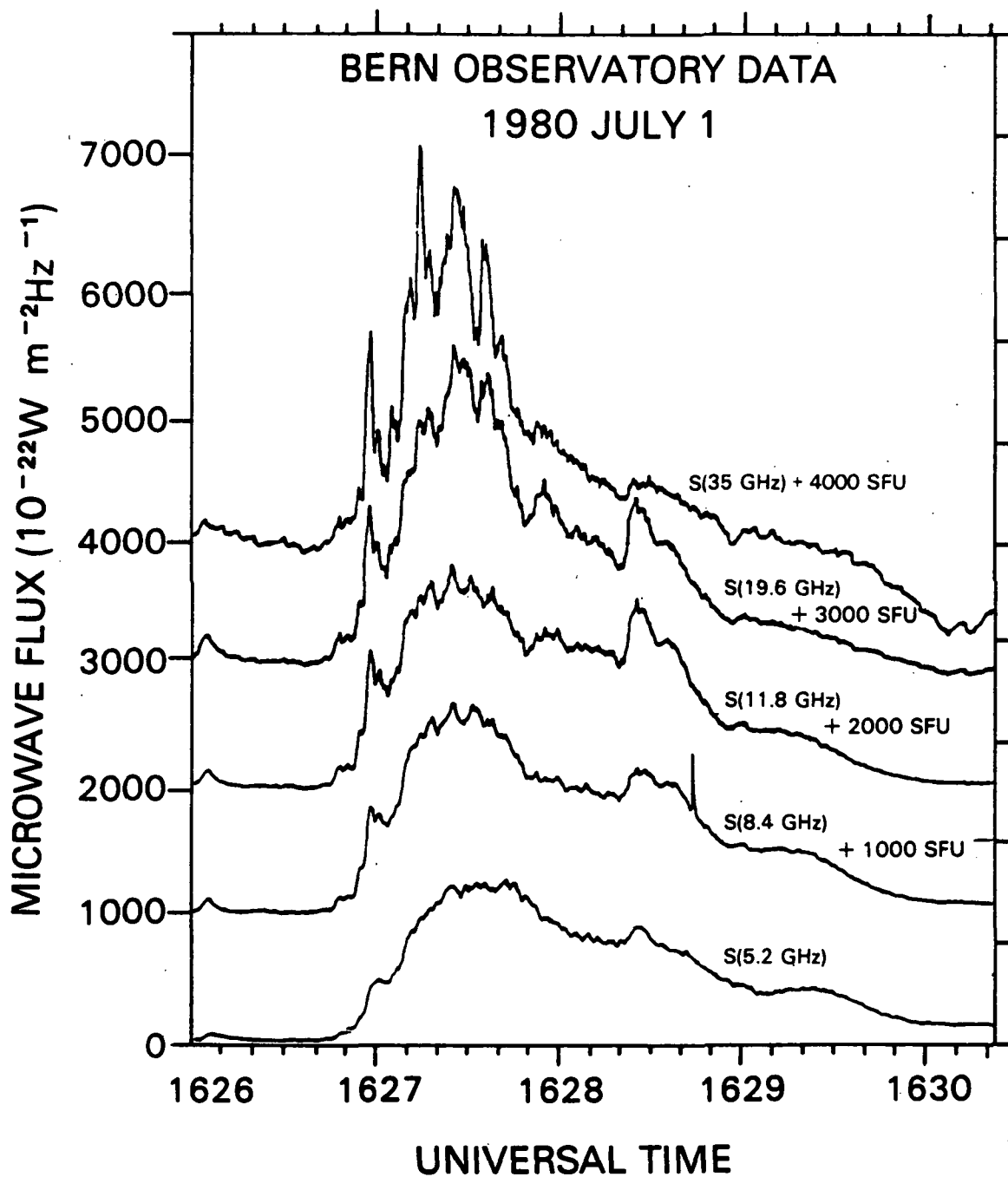


Figure 2-7. Dynamic microwave spectrum of the flare shown in Figures 2-2, 2-3, and 2-4. Crosses indicate the observing frequencies. The start time is indicated in UT at lower left; thereafter, the number of seconds after the start labels each spectrum.

measured in Solar Flux Units (SFU), as a function of frequency,  $f$ . (The unit SFU is the standard unit used in solar radio astronomy;  $1 \text{ SFU} \equiv 10^{-22} \text{ W m}^{-2} \text{ Hz}^{-1}$ .) This event is typical in that its spectra usually are characterized by an increasing flux density at low frequencies, up to a spectral maximum,  $f_{\text{max}}$ , above which the flux declines. Such spectra are classified as type C (Guidice and Castelli 1975). A less common feature of this event is the flatness of the spectrum after about 0955:26 UT. As noted by Hachenberg and Wallis (1961), some bursts produce spectra that are nearly flat over a wide range of frequencies. More complex spectra are sometimes observed, e.g. with multiple peaks. Microwave spectral morphologies have been classified and subjected to statistical analysis by Guidice and Castelli (1975).

The dynamic spectra of microwave bursts have been studied by Karpen, Crannell, and Frost (1979), Karpen (1980), and Kosugi (1981). In some cases the spectral maximum changes during the burst, as in Figure 2-7, but in most cases, the intensity at each frequency changes proportionally, as in Figure 1 of Karpen, Crannell, and Frost (1979). Further observations are necessary to determine whether a change in the observed  $f_{\text{max}}$  is the result of a change in the spectrum of a single source, or the appearance of another source with a spectrum characterized by a different  $f_{\text{max}}$ .

Another way to present the spectral data is by means of multiple time histories, as shown in Figure 2-8. At the highest frequencies, the most rapid variations in flux are observed. The time history of the hard X-ray flux is very similar to the 35 GHz trace in Figure 2-8. The correspondence is not so good, however, for microwave frequencies below the spectral maximum. For example, in the 5.2 GHz trace, the sharp



**Figure 2-8. Time histories at various frequencies for the flare of 1980 July 1 at 1626 UT. Each trace is displaced upward by 1000 SFU from the one below for separation.**

variations seen at high frequencies and in hard X rays are lost in a more gradual component.

In some cases, a delay is observed between features of the hard X-ray time history and the corresponding features of the microwave time history. This delay has been studied by many investigators (e.g. Crannell et al. 1978; Kaufmann et al. 1983; Cornell et al. 1984). There is a general tendency for impulsive microwave bursts to rise more slowly and reach a peak in emission shortly after the impulsive hard X rays. These delays range from small fractions of 1 s to a few seconds. The fall time of microwave emission is usually significantly longer than the fall time in hard X-rays. There is no general agreement on the cause of the delays, but they are not considered long enough to bring the common source hypothesis into doubt. The combination of the effects of the evolution of the electron distribution and the variation of magnetic field during a burst may be responsible, as suggested by Brown et al. (1983b).

Interpretations of the behavior described in this section are discussed in Section 2.4. Impulsive microwave emission is widely referred to as nonthermal, as is the impulsive hard X-ray emission, but a thermal origin for the microwaves is also possible, as discussed in Section 2.4.4.

Imaging observations of flares have been made by means of one-dimensional interferometry with linear antenna arrays, and, more recently, two-dimensional mapping with the Very Large Array (VLA). One-dimensional observations have been made by many observers (e.g. Knome, Kakinuma, and Tanaka 1969, and references therein; see also references in Kundu 1965, and Krüger 1979). These observations

established that burst source sizes are typically  $\lesssim 30$  arc seconds in angular size, and provided some information about the association of burst sources with features of active regions. Two-dimensional imaging observations are needed, with resolution better than 0.1 arc second, to determine the details of source structures. The VLA is capable of this resolution, and has been used for observations of a few flares; some results of these observations are reviewed by Marsh and Hurford (1982). Complete understanding of the role of energetic electrons in impulsive flares requires comparison between the structures of hard X-ray and microwave sources, however. Only one flare has been so analyzed, a small flare which was mapped in two dimensions at 15 GHz with the VLA, and imaged in the range 3.5 to 30 keV with HXIS (Hoyng *et al.* 1983). In that flare, the microwave source appeared to have a smaller projected area than the hard X-ray source, and the centroids of both sources appeared to coincide within a few arc seconds. Unfortunately, the relationship between microwave and hard X-ray source structures was not firmly established, because the burst was a complex one, and the X-ray data were very uncertain, due to poor counting statistics.

Interferometric observations of microwave bursts generally indicate that the sources are situated above a "neutral line", defined by the reversal of the polarity of the photospheric magnetic field in an active region. This supports the interpretation that the energetic electrons responsible for the bursts are located in coronal arches which connect the regions of opposite polarity (*cf.* Marsh and Hurford 1982, and references therein).

#### 2.4.2 The Emission Process — Gyrosynchrotron Radiation

The particles in a magnetized plasma gyrate around the magnetic field lines in response to the Lorentz force. The acceleration of the particles as they gyrate gives rise to gyromagnetic emission. In general, the electrons experience the largest acceleration, because of their small mass, and therefore dominate the emission.

Gyromagnetic emission is discussed by Trubnikov (1958), Ginsburg and Syrovatskii (1965), Bekefi (1966), and Melrose (1979). Gyromagnetic emission from nonrelativistic electrons is concentrated at the electron gyrofrequency  $\Omega_e = eB/m_e c$  and its first few harmonics. In the case of ultrarelativistic electrons, the emission is concentrated at very high harmonics. In the case of mildly relativistic electrons, which emit chiefly at harmonics from about 10 to 100, the emission is called gyrosynchrotron radiation.

The detailed correspondence of the time variations of hard X-ray and microwave emissions suggests that both come from the same distribution of energetic electrons. The interpretation of the hard X-ray spectra as bremsstrahlung leads to the inference that electrons with energies  $E \gtrsim 10$  keV produce the X rays. A distribution of electrons consistent with the hard X-ray spectrum, whether of power-law or thermal form, would also emit gyrosynchrotron radiation if the magnetic field were of order 100 G (Holt and Ramaty 1969; Takakura 1972; Ramaty and Petrosian 1972; Mätzler 1978; Dulk, Melrose and White 1979). Magnetic fields of this order are characteristic of the coronal parts of active regions, as mentioned in Section 2.1, and the interpretation of the microwave emission as gyrosynchrotron radiation

has become accepted.

A possible alternative emission mechanism is thermal free-free emission, or bremsstrahlung. In Section 2.4.4, it is shown that free-free emission is negligible when compared with the gyrosynchrotron emission from sources of relevance to this work.

### 2.4.3 Radiative Transfer

The microwave emission, unlike the hard X-ray emission, is subject to propagation effects. The radiative transfer equation must be solved in order to obtain the microwave spectrum. The following derivation of the microwave spectrum from the basic principles of radiative transfer is adapted from a preprint of Dulk and Marsh (1982).

The radiative transfer equation can be written in terms of the specific intensity,  $I_f$ , defined at a fixed frequency,  $f$ , as follows:

$$dI_f/d\tau_f = -I_f + F_f, \quad (2.23)$$

where  $I_f$  is in  $\text{erg cm}^{-2} \text{ s}^{-1} \text{ Hz}^{-1} \text{ sr}^{-1}$ ,  $d\tau_f = K_f dz$  is the differential optical depth,  $dz$  is the differential length along a ray path, and  $F_f$  is called the source function.  $F_f$  is defined to be the ratio of the volumetric emission coefficient, or emissivity,  $\eta_f$ , to the linear absorption coefficient,  $K_f$ . The units of  $\eta_f$  are  $\text{erg cm}^{-3} \text{ s}^{-1} \text{ Hz}^{-1} \text{ sr}^{-1}$ , and the units of  $K_f$  are  $\text{cm}^{-1}$ . It is more convenient to express the transfer equation in terms of the brightness temperature,  $T_b$ , which is defined by means of the pseudo-Planckian equation

$$I_f = \frac{hf^3}{c^2} \frac{1}{\exp(hf/kT_b) - 1} , \quad (2.24)$$

where, in contrast to the true black body equation,  $T_b$  may be a function of  $f$ . The advantage in conceptual simplicity of the use of  $T_b$  will become apparent when we come to the final expressions for the spectrum.  $T_b$  is also useful because observations are actually made by measuring  $T_b$ .

There are two modes with orthogonal polarizations, known as the ordinary and extraordinary modes, which propagate in the plasma. In general, the modes have orthogonal senses of polarization. Each equation in this section applies separately for each mode. Identifying the modes explicitly, the total specific intensity is

$$I_f^{\text{tot}} = I_f^{\text{o}} + I_f^{\text{x}} , \quad (2.25)$$

where o and x label the modes. Henceforth, explicit labels of the mode will be omitted unless they are required, but the independence of the two modes should be remembered.

In the radio frequency range, where  $hf \ll kT_b$ , we have the Rayleigh-Jeans form

$$I_f = kT_b f^2 / c^2 . \quad (2.26)$$

For the source function, it is also convenient to change to the variable  $T_{\text{eff}}$ , the effective temperature of the radiating particles at a specific position in the source, defined by the expression

$$F_f = \frac{hf^3}{c^2} \frac{1}{\exp(hf/kT_{\text{eff}}) - 1} . \quad (2.27)$$

In the radio range, where  $hf \ll kT_{\text{eff}}$ , this becomes

$$F_f = kT_{\text{eff}} f^2 / c^2 . \quad (2.28)$$

The radiative transfer equation then takes the simple form

$$dT_b/d\tau_f = -T_b + T_{\text{eff}} , \quad (2.29)$$

which can be integrated to yield

$$T_b = \int_0^{\tau_f} dt_f T_{\text{eff}} \exp(-t_f) + T_{b0} \exp(-\tau_f) , \quad (2.30)$$

In this equation,  $T_{b0}$  is a constant of integration, and the optical depth or optical thickness is denoted as  $\tau_f$ . The geometry is illustrated in Figure 2-9, after Dulk and Marsh (1982).  $T_{b0}$  is clearly the brightness temperature of the background beyond the source, if any. It should be noted that the forms of the radiative transfer equation written above are valid only for media in which the density  $n_e$  is sufficiently low that the index of refraction is nearly unity. For sufficiently high density, medium suppression, a.k.a. the Razin-Tsytovich effect, must also be accounted for. This effect is important only when  $f < 20 n_e/B_+$ , where  $B_+$  is the component of

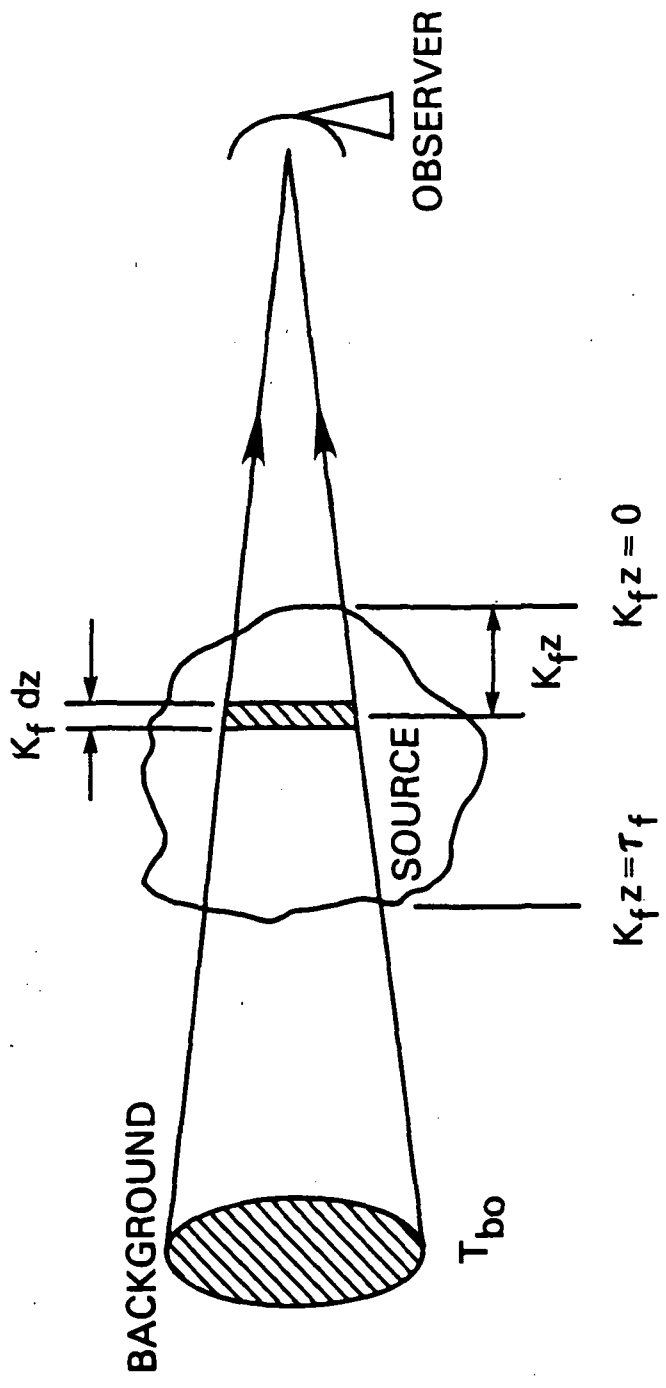


Figure 2-9. Geometry of microwave radiative transfer (after Dulk and Marsh 1982).  $K_f$  is the absorption coefficient,  $T_{bo}$  is the brightness temperature of the background,  $z$  is the distance along the ray path, and  $\tau_f$  is the optical depth.

magnetic field perpendicular to the observer's line of sight (Ginzburg and Syrovatskii 1965).

For the special case of  $T_{b0} = 0$  and  $T_{\text{eff}} = \text{constant}$ , we have

$$T_b = T_{\text{eff}} [1 - \exp(-\tau_f)] . \quad (2.31)$$

In this case,  $K_f$  and  $\eta_f$  are constant, and  $\tau = K_f z$ . If  $\tau_f \ll 1$  (optically-thin case), then  $T_b = T_{\text{eff}} \tau_f = (c^2/kf^2)\eta_f z$ ; if  $\tau_f \gg 1$  (optically-thick case), then  $T_b = T_{\text{eff}}$ . It should be noted that  $T_b \leq T_{\text{eff}}$ , and that  $T_b = T_{\text{eff}}$  only if  $\tau_f \gg 1$ . For a Maxwellian distribution of electrons,  $T_{\text{eff}} = T_e$ .  $T_{\text{eff}}$  is generally a function of  $f$  and the mode in the case of a nonthermal electron distribution.

To compute the spectrum, expressions for the emission and absorption coefficients are required. These expressions are conveniently written in terms of the harmonic number  $f/f_B$ , where  $f_B = \Omega_e/2\pi$ . The emissivity  $\eta_f$  is proportional to  $NB$ , where  $N$  is the total number density of electrons with  $E \geq E_0$ . (In the case of a Maxwellian,  $E_0 = 0$  and  $N = n_e$ .) The absorption coefficient  $K_f$  is proportional to  $N/B$ . Therefore it is convenient to work with the quantities  $\eta_f/NB$  and  $K_f B/N$ . Then

$$T_{\text{eff}} = \frac{c^2}{kf^2} \frac{\eta_f}{K_f} = \frac{c^2}{k} \frac{(\eta_f/NB)}{(K_f B/N)} \frac{B^2}{f^2} = 8.33 \times 10^{23} \frac{(\eta_f/NB)}{(K_f B/N)} \left[ \frac{f}{f_B} \right]^{-2} . \quad (2.32)$$

The o and x modes are circularly polarized in opposite senses. For one polarization mode  $m$  (either x or o), the flux density,  $S_m$ , is

related to  $T_{b,m}$  by

$$S_m = (kf^2/c^2) \int d\Omega T_{b,m} , \quad (2.33)$$

where  $d\Omega$  is the differential solid angle, and the integration is over the projected area of the source. The integration is trivial for a source with uniform  $\vec{B}$ ,  $T_{\text{eff}}$ , and  $\theta$  (the angle between  $\vec{B}$  and the line of sight). For a uniform source at a distance of 1 AU with sharp boundaries, the result is

$$S_m = 6.8 \times 10^{-45} f^2 A T_{b,m} , \quad (2.34)$$

where  $f$  is in Hz,  $A$  is the projected area in  $\text{cm}^2$ , and  $S_m$  is in SFU.

If  $\tau_f \ll 1$ , this reduces to

$$S_m = 4.4 \times 10^{-8} (\eta_{f,m}/BN) B N A z . \quad (2.35)$$

If  $\tau_f \gg 1$ , then

$$S_m = 6.8 \times 10^{-45} f^2 A T_{\text{eff},m} . \quad (2.36)$$

A general description of the polarization transfer involves polarization tensors (Melrose 1979, vol. 1, p. 196). In the simple case of a uniform source, the degree of circular polarization is

$$r_c = (T_{b,x} - T_{b,o}) / (T_{b,x} + T_{b,o}) . \quad (2.37)$$

To obtain the total flux density, it is necessary to determine  $r_c$ . The o-mode flux density is then related to the x-mode flux density by

$$S_o = \frac{1 - r_c}{1 + r_c} S_x, \quad (2.38)$$

and the total flux density is just

$$S = S_x + S_o = 2 S_x / (1 + r_c). \quad (2.39)$$

#### 2.4.4 Gyrosynchrotron Emission from Thermal Electrons

In the case of a plasma in which the emitting electrons have a Maxwellian distribution and an isotropic distribution of pitch angles, for each mode we have (i)  $T_{eff} = T_e$ , and (ii)  $\eta_f = K_f k T_e (f^2/c^2)$  (Kirchoff's Law). The emission and absorption coefficients were calculated analytically for this case by Trubnikov (1958), and numerically by Mätzler (1978). The exact expressions are very cumbersome, and the approximations derived by Dulk, Melrose, and White (1979) for the x mode are adequate for our purposes:

$$(K_{f,x} B) / n_e \approx 50 T_e^7 (\sin \theta)^6 B^{10} f^{-10}, \quad (2.40)$$

$$\eta_{f,x} / (B n_e) \approx 1.2 \times 10^{-24} T_e (f/f_B)^2 (K_{f,x} B) / n_e. \quad (2.41)$$

The range of validity of the approximations is  $10 \lesssim f/f_B \lesssim 100$ ,  $20^\circ \lesssim \theta \lesssim 80^\circ$ , and  $10^8 \text{ K} \lesssim T_e \lesssim 10^9 \text{ K}$ . These expressions are

accurate to better than a factor of 2 over some 20 decades of variation.

The spectrum of the radiation in each mode from a thermal source rises with increasing  $f$  in the optically-thick range, according to the Rayleigh-Jeans law, reaches a peak at  $f_{\max}$ , the frequency for which  $\tau_f = 1$ , and falls steeply in the optically-thin range. This behavior is conveniently characterized by means of the spectral index  $\alpha(f) \equiv d \log S(f)/d \log f$ . In the optically thick range,  $\alpha(f) = 2$ ; in the optically-thin range,  $\alpha(f) \approx -8$  (cf. Mätzler 1978; Dulk and Marsh 1982).

The peak frequency for the  $x$  mode can be found by setting  $K_{f,xz}$  equal to unity and solving Equation (2.37), with the result

$$f_{\max} \approx 1.4 (n_e z/B)^{0.1} (\sin \theta)^{0.6} T_e^{0.7} B. \quad (2.42)$$

For a uniform, sharp-edged thermal source, in the frequency range in which  $\tau_f \gg 1$  for both modes,  $r_c = 0$ . For  $\tau_f \sim 1$ , the polarization is small,  $\sim 10\%$ . Thus, by Equation (2.39),  $S_{\max} \approx 1.8 S_{x,\max}$ . In the range in which  $\tau_f \ll 1$  for both modes, the polarization is in the sense of the  $x$  mode, and is approximately

$$r_c \approx 6.1 T_e^{-0.18} 10^{2.1 \cos \theta - 1.3 \cos^2 \theta} \left[ \frac{f}{f_B} \right]^{0.045 - 0.30 \sin \theta}. \quad (2.43)$$

Because of the steep  $f^{-10}$  dependence of  $K_f$ , the frequency range  $\delta f$  over which  $\tau_f \approx 1$  for either mode is quite narrow,  $\lesssim 2$  GHz. The difference between  $f_{\max,x}$  and  $f_{\max,o}$  is of this order. The  $f_{\max,x}$  is therefore a good approximation of the frequency  $f_{\max}$  at which

$S_{\max} \equiv \text{Max}(S)$  is observed.

The utility of the expressions given in this section lies in the relations they provide between observables and physical parameters of the source. For example, if  $T_e$  is known from the hard X-ray spectrum, then  $f_{\max}$  can be used to obtain  $B$  from Equation (2.42), given some reasonable assumptions of the values of the remaining parameters. This is done in Section 3.4.

It was mentioned in Section 2.4.2 that thermal free-free emission is also a possible emission mechanism for microwave bursts. The importance of this mechanism relative to gyrosynchrotron emission can be assessed by comparing the absorption coefficients. The linear absorption coefficient for free-free emission is given by Tucker (1975):

$$K_f' = 1.7 \times 10^{-3} n_e^2 f^{-2} T_e^{-3/2} . \quad (2.44)$$

This expression is compared with  $K_f$ , the equivalent quantity for gyrosynchrotron emission (Equation 2.40). The ratio of these is

$$K_f/K_f' = 290 (\sin \theta)^6 T_e^{8.5} B^9 n_e^{-1} f^{-8} . \quad (2.45)$$

For values of the physical parameters typical of those inferred in Chapter V,  $T_e = 3 \times 10^8$  K,  $B = 200$  G,  $n_e = 2 \times 10^9$  cm<sup>-3</sup>, and  $f = 8 \times 10^9$  Hz. The ratio of gyrosynchrotron absorption to free-free absorption is  $5 \times 10^6 (\sin \theta)^6$ . Because the direction of  $B$  varies within an arch, it is not possible for  $\theta$  to be small throughout the source, and, in general, there will be emission from parts of the source with  $\theta \approx 90^\circ$ . Thus free-free emission clearly represents a negligible fraction of the

microwave emission from sources of relevance to this work.

#### 2.4.5 Gyrosynchrotron Emission from a Power-Law Distribution of Electrons

In this section, a brief description is given of the gyrosynchrotron emission from nonthermal energetic electrons such as those that figure in the thick-target model (Section 2.3.4), the trap-plus-precipitation model (Section 2.3.5), and other nonthermal models. A power-law distribution of electrons is generally assumed in these models. The calculation of the gyrosynchrotron emission from these electrons is much more complex in some cases than in the thermal case. The effects of anisotropy of the electron pitch angle distribution may not be negligible in beam models such as the thick-target model, and Kirchoff's law no longer applies, so that the emission and absorption coefficients must be determined separately. If the simplifying assumption of negligible anisotropy is made, however, then the spectra can be calculated easily by means of the approximations of the emission and absorption coefficients derived by Dulk and Marsh (1982). While some nonthermal models require strong anisotropy of the electron pitch angle distribution, there is at present no observational evidence for it (cf. Datlowe et al. 1977; Zolcinski et al. 1983).

Detailed calculations of the spectra for various nonthermal models are given by Takakura (1967), Ramaty (1969), Takakura and Scalise (1970), Trulsen and Fejer (1970), Wild and Hill (1971), and Tarnstrom (1976, 1977).

Assuming that the electron energy distribution function is a power

law (Equation 2.4), and that the pitch angle distribution is isotropic, the emission and absorption coefficients for the x mode can be approximated by (Dulk and Marsh 1982)

$$\eta_{f,x}/(BN) \approx 3.3 \times 10^{-24} 10^{-0.52\delta} (\sin \theta)^p (f/f_B)^q \quad (2.46)$$

where  $p(\delta) = -0.43 + 0.65\delta$ , and  $q(\delta) = 1.22 - 0.90\delta$ ,

$$(K_{f,xB})/N \approx 1.4 \times 10^{-9} 10^{-0.22\delta} (\sin \theta)^p (f/f_B)^q \quad (2.47)$$

where  $p(\delta) = -0.09 + 0.72\delta$ , and  $q(\delta) = -1.30 - 0.98\delta$ .  $T_{\text{eff}}$  depends, in this case, on the parameters approximately as

$$T_{\text{eff},x} \approx 2.2 \times 10^9 10^{-0.31\delta} (\sin \theta)^p (f/f_B)^q \quad (2.48)$$

where  $p(\delta) = -0.36 - 0.06\delta$ , and  $q(\delta) = 0.50 + 0.085\delta$ . For  $\tau_f \gg 1$ , the polarization,  $r_c$ , is  $\approx 10\%$  or less, in the sense of the o mode. For  $\tau_f \ll 1$ , the polarization is given by

$$r_c \approx 0.20 10^{0.05\delta} 10^p (f/f_B)^q, \quad (2.49)$$

where  $p(\theta) = 1.93 \cos \theta - 1.16 \cos^2 \theta$ , and  $q(\alpha) = -0.21 - 0.37 \sin \theta$ .

For the range  $2 \leq \delta \leq 7$ ,  $\theta \geq 20^\circ$ , and  $f/f_B \geq 10$ , these expressions are accurate to better than 26%. An example of the application of these formulae to interpretation of observations is given by Hoyng et al. (1983).

The spectrum of a power-law distribution is qualitatively similar

to that of the thermal distribution in that there is a low-frequency rising part, a peak at  $f_{\max}$ , and a high-frequency falling part. The chief differences between the spectra of thermal and power-law electron distributions are as follows. First, for  $\tau \gg 1$ , the power-law distribution gives rise to a spectrum that is steeper than the Rayleigh-Jeans law ( $\alpha(f) = 2$ ). In the power-law case,  $\alpha(f) \approx 2.9$ . Secondly, for  $\tau \ll 1$ , the spectrum is less steep than in the thermal case, varying from  $\alpha(f) \approx -1.5$  for  $\delta = 3$  to  $\alpha(f) = -4.2$  for  $\delta = 6$ .

#### 2.4.6 Inhomogeneous Sources

The observed spectral form of an impulsive microwave burst does not always correspond to that of a uniform, sharp-edged source, whether of a thermal or power-law electron distribution (cf. Figures 2-7, 5-4). For  $f < f_{\max}$  and a thermal distribution,  $\alpha(f) = 2$  (the Rayleigh-Jeans law), whereas, in the case of a power-law distribution,  $\alpha(f) \approx 2.5$  for this low-frequency range. In some cases, the low-frequency spectral index of observed sources is less than either of these values. Homogeneous, sharp-edged sources of either type also cannot explain the shallow slopes of some spectra in the range  $f > f_{\max}$ .

Several explanations have been proposed for the shallow slopes of some observed spectra. Optically-thin free-free emission was suggested by Hachenberg and Wallis (1961). This alternative can be ruled out because the high brightness temperatures observed ( $T_b > 12 \times 10^8$  K) require emission measures far larger than observed in hard X rays (Mätzler 1978). It was also proposed by Ramaty and Petrosian (1972) that the emission is free-free absorbed gyrosynchrotron emission from

nonthermal electrons, the absorption originating in plasma of  $T_e \sim 10^6$  K within the source. The problem with this explanation is that it requires a large free-free optical depth,  $\tau_{ff}$ , inside the nonthermal gyrosynchrotron source. A small amount of such gas just outside the source would impose additional absorption, by a factor of  $\exp(-\tau_{ff})$ , where  $\tau_{ff}$  is large and proportional to  $f^{-2}$  (Mätzler 1978). This would result in a sharp, low-frequency cut-off which is not always characteristic of spectra with shallow slopes.

The most promising alternative explanation of the spectral flattening is a nonuniform magnetic field, and, in some cases, a nonuniform electron distribution as well.

For the thermal case, the consequences of gradients in B were studied by Mätzler (1978). The possibility that both  $T_e$  and B vary within the source has been considered by Schöchlin and Magun (1979), Dulk and Dennis (1982), and Wiehl *et al.* (1983). In these models, local thermodynamic equilibrium is assumed.

The basis of the inhomogeneous models that have been formulated to date is the assumption that the temperature and magnetic field are greatest within a central region, and decline with distance from that hottest core. Both cylindrical and spherical source geometries have been considered. The cylindrical case is applicable to a single arch source (Mätzler 1978; Schöchlin and Magun 1979), while spherical symmetry might be appropriate to a nest or arcade of arches (Mätzler 1978; Dulk and Dennis 1982).

The result of the decline in  $T_e$  and B is that the outer layers of the source exhibit unit optical depth at lower frequencies. That is,  $f_{\max}$  is a decreasing function of radius from the core. The low-

frequency part of the microwave spectrum observed by a radiometer without spatial resolution therefore exhibits a value of  $\alpha(f)$  less than 2, the spectral index of a homogeneous source. In effect, the source as a whole exhibits an area that is a function of frequency,  $A(f)$ . The frequency of maximum emission of the spectrum is associated with the hottest core.

**Page Intentionally Left Blank**

## Chapter III

### THE THERMAL MODEL WITH CONDUCTION FRONT CONFINEMENT

#### 3.1 Development and Previous Applications of the Model

Conduction front confinement of a thermal hard X-ray source was first studied in the solar flare context by Brown, Melrose, and Spicer (1979, BMS). Spicer (1976, 1977a) had proposed magnetic reconnection via the tearing-mode instability as the energy-release mechanism for flares, and his calculations suggested that a pre-flare coronal arch would be most unstable to tearing-mode growth near its apex. Most of the energy released would go into heating the unstable portion of the arch (cf. Smith 1980). BMS therefore investigated the consequences of localized, impulsive heating of electrons at the apex of such an arch to a temperature  $T_e \gtrsim 10^8$  K. (Current-driven instabilities such as the tearing mode chiefly heat the electron component of the plasma, rather than the bulk of the ions.) The result of this energy release is illustrated in Figure 3-1. The heated region was taken to be of length  $L$  at the time of maximum emission.  $L \approx 10^4$  km was found to be consistent with observations. For reasonable coronal densities,  $n_e$ , of order  $10^9$  to  $10^{11}$   $\text{cm}^{-3}$  and electron temperatures characteristic of the hard X-ray spectra, the electron-ion energy equipartition time,  $\tau_{eq}$ , is of order  $10^4$  s (Spitzer 1962), thus the ions would remain

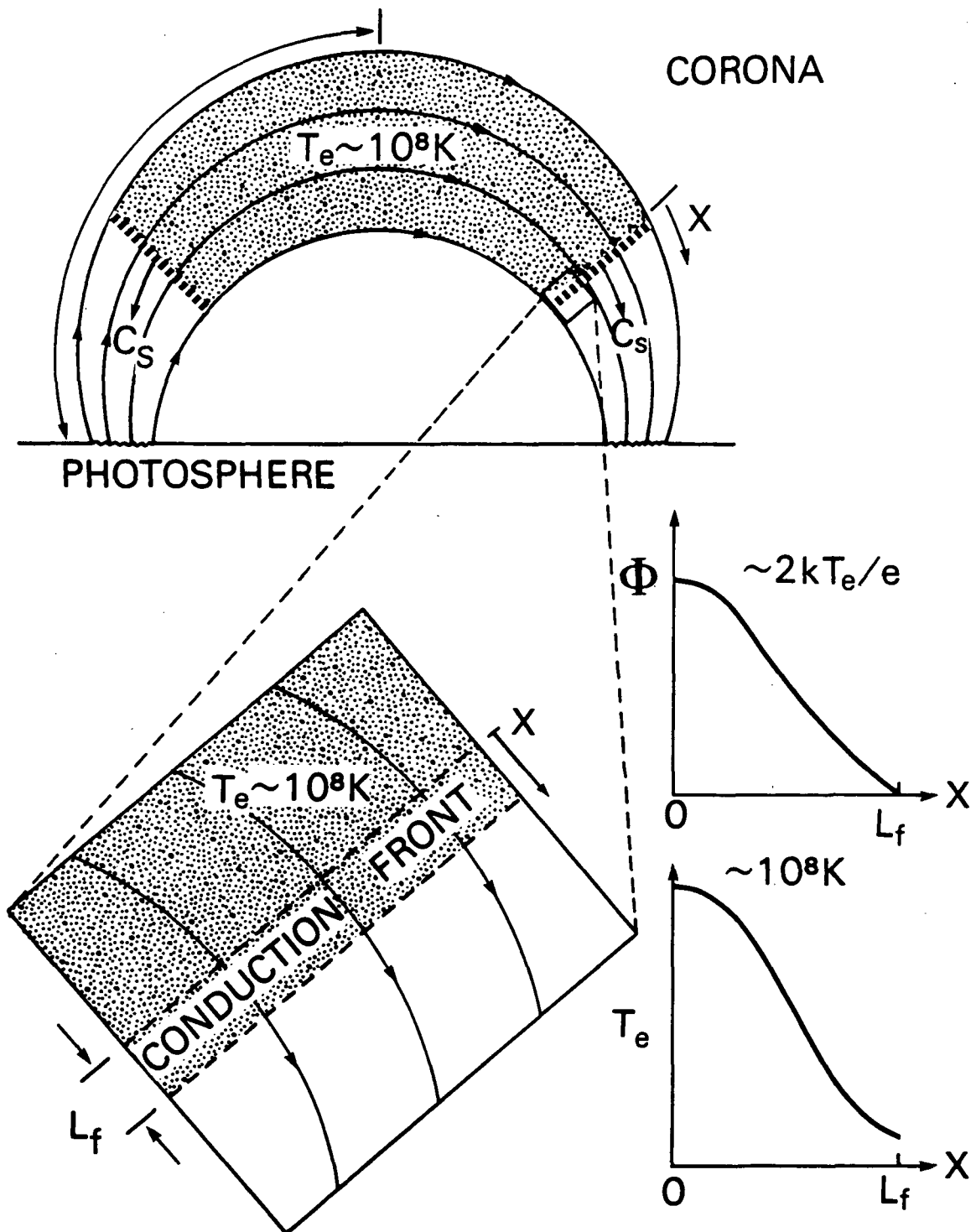


Figure 3-1. Schematic diagram of the thermal model with conduction front confinement in a coronal arch. Shading indicates the confined, high-temperature electrons. A portion of the conduction front is expanded to indicate its thickness,  $L_f$ . The front velocity is the ion-acoustic velocity,  $c_s$ . The coordinate  $x$  is the distance along the arch in the direction away from its apex, as measured from the boundary of the front nearest to the apex. The graphs illustrate the variation of the electric potential due to the thermoelectric field and the temperature in the front.

at their pre-flare temperature throughout the burst. In addition, under these conditions, the collisional mean free path of the hot electrons would exceed  $L$ . The hot electrons in such a region would begin to escape along the magnetic field lines, with negligible cross-field diffusion, and enter the gas in the lower parts of the arch, which would still be at pre-flare temperatures of  $\approx 2 \times 10^6$  K. As shown by Spicer (1977b), the hot electrons, streaming into the cooler region, would induce a neutralizing reverse current of cooler electrons, with a drift velocity,  $v_d$ , which would exceed the ion-sound velocity,  $c_s = (kT_e/m_i)^{1/2}$ . For  $v_d > c_s$ , the plasma is unstable to the growth of turbulent ion-sound waves, which are longitudinal, propagating oscillations of the electrons and ions (Boyd and Sanderson 1969; Krall and Trivelpiece 1973). These waves would grow in amplitude with an e-folding rate of order  $\omega_i$ , the ion plasma frequency, which is defined by the expression  $\omega_i \equiv (4\pi n_i e^2/m_i)^{1/2}$ . For the solar atmosphere,  $m_i \approx m_p$ , and the growth rate of the waves in a coronal arch with density  $\sim 10^9 \text{ cm}^{-3}$  would be  $\sim 10^7 \text{ s}^{-1}$ . The spectrum and directional distribution of the ion-sound waves is described by Horton and Choi (1979), both theoretically and as they are observed in comparable laboratory plasmas. Figure 3-2 illustrates these properties of the turbulent waves. The turbulent wave amplitude would grow for a few growth times — a few times  $10^{-7} \text{ s}$  — and would saturate with a total energy density in the waves  $w_s \approx 10^{-2} w_T$ , where  $w_T$  is the thermal energy density (pressure) in the plasma. The resulting ion-sound turbulence would be maintained at a marginally stable level in a relatively thin front at each end of the hot region, known as a collisionless conduction front. The conduction front would limit

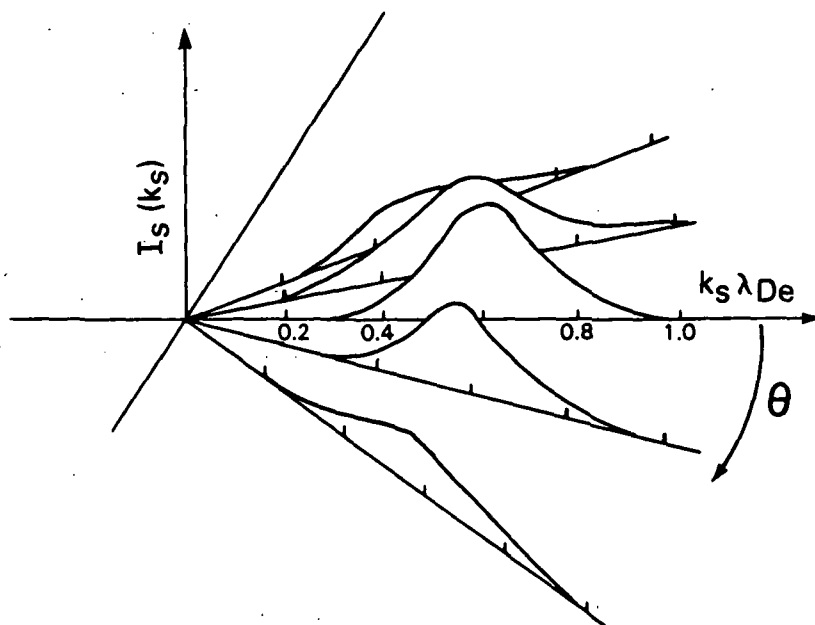


Figure 3-2. Distribution of amplitude of the ion-acoustic waves in the conduction front, as a function of the direction and magnitude of  $\vec{k}_s$ . The direction  $\theta = 0$  corresponds to the negative  $x$  direction in Figure 3-1. The quantity  $I_s(k_s)$  is the amplitude of the ion-acoustic wave with wave number  $k_s$ . The wave number  $k_s$  is the radius from the  $I_s$  axis, expressed in the units  $1/\lambda_{De}$ . (Figure after Horton and Choi 1979.)

expansion of most of the hot electrons to the speed of propagation of the front,  $\sim c_s$ . Thus, the turbulence would serve as a confinement mechanism, insulating the hot electrons. Note also that, in the absence of the turbulence, the hot electrons would stream out of the source with a speed of order  $v_e = (kT_e/m_e)^{1/2}$ . For the solar atmosphere, with  $m_i \approx m_p$ ,  $c_s$  is about  $v_e/43$ . Thus the turbulence would reduce the cooling rate of the source by about a factor of 43 below its free-streaming value. The turbulence also would effectively increase the collision rate of the electrons, leading to a relaxed electron distribution despite the low frequency of Coulomb collisions. The laboratory experience of Fowler (1968) suggests that the relaxed distribution would be nearly Maxwellian.

BMS and Smith and Lilliequist (1979, SL) gave detailed derivations of the front thickness and showed that the front velocity is  $c_s$ . BMS identified the hard X-ray fall time of emission from such a source with the cooling time,  $\tau_{cool} = L/c_s$ .

SL proposed a similar physical picture, but added several more realistic features. A one-dimensional, one-fluid, two-temperature numerical simulation was used to follow the evolution of a tube filled with plasma, continuously heated at its apex. This allowed the effects of convection to be taken into account. Continuous heating was also more realistic from an observational viewpoint; the temperature of hard X-ray bursts usually increases continuously until the time of maximum emission or later (e.g. Crannell *et al.* 1978; Wiehl *et al.* 1983). SL showed that conduction fronts indeed would develop in an arch  $10^4$  km in length with  $n_e = 3 \times 10^{11} \text{ cm}^{-3}$ . Computational problems limited the simulation to a duration of 0.74 s, however.

Smith and Auer (1980, hereinafter SA) extended the duration of the simulation and studied the consequences of varying the heating rate and initial temperature, also using the same initial density as SL. They showed that for the higher heating rates, the hot part of the arch divided into two regions of different temperatures, bounded by conduction fronts that advanced at velocities somewhat different from  $c_s$ . The two temperatures gave rise to a hard X-ray spectrum of the whole source that was indistinguishable from a power law over the photon energy range from 10 to 100 keV (cf. Brown 1974).

The most realistic simulation carried out to date, and the one with results of most relevance to the present work, was carried out by Smith and Harmony (1982, hereinafter SH2). For the first time, the limit of the expansion of the source was studied. A model chromosphere was included at the feet of the arch. When the conduction front reached the chromosphere, the cooler, denser matter there mixed with the hot, tenuous gas of the hard X-ray source, quenching it. SH2 provided a time history of the resultant hard X-ray flux, summed over photon energies  $\epsilon > 10$  keV, which resembles that of a simple, "spike" burst (compare Figure 4 of SH2 with Figure 1 of Crannell et al. 1978). The fall time of the emission was about equal to the rise time. (Similar results were obtained by Smith and Harmony 1981, hereinafter SH1.) The result of SH1 and SH2 that is most important to the present analysis is that the peak of the hard X-ray time history occurred at the time when the conduction fronts reached the chromosphere and mixing began to quench the source.

Before discussing theoretical advances that pertain to the microwave emission, it is worthwhile to consider two objections that have been raised against the kind of model developed by BMS and Smith

and collaborators, and to show that these objections can be refuted. First, there is the question of whether the model makes reasonable energetic demands. The energy source of solar flares is widely believed to be magnetic field annihilation. Observations suggest that a component of magnetic field  $B$  of order 100 G is available for annihilation in active region magnetic configurations. Annihilation of 100 G in a given volume yields only  $400 \text{ erg cm}^{-3}$ . The numerical models of Smith and collaborators therefore have been criticized because they require much larger heating rates to be sustained for several seconds. For example, SA assumed heating rates in the range 1 to  $8 \times 10^4 \text{ erg cm}^{-3} \text{ s}^{-1}$ . It should be noted, however, that these large heating rates were chosen to achieve the required temperatures for emission of hard X rays ( $\approx 2 \times 10^8 \text{ K}$ ) specifically with an assumed density of  $3 \times 10^{11} \text{ cm}^{-3}$ . If the density were two orders of magnitude smaller, e.g. a few times  $10^9 \text{ cm}^{-3}$ , the heating rate required to achieve the same temperature would be correspondingly smaller, and thus consistent with a few hundred G of annihilated field. If the observations reported here are interpreted with the conduction front model, densities of a few times  $10^9 \text{ cm}^{-3}$  are indeed inferred, as shown in Chapter V. Densities of this order are also consistent with those inferred from observations by Crannell et al. (1978), and agree with typical pre-flare densities observed in active regions.

As an aside, it may be noted that the densities of order  $3 \times 10^{11} \text{ cm}^{-3}$  alluded to above would imply much smaller source volumes than are consistent with the microwave observations to be described herein.

A second objection to the model of BMS and SL was raised by Brown, Craig, and Karpen (1980, hereinafter BCK). BCK argued that a single hot

source, or kernel, of the kind examined by BMS, could not explain the observed spectral evolution. Their argument was based on the predicted relationship between the two parameters that specify the thermal bremsstrahlung spectrum:  $T_e$  and the emission measure,  $\mu = n_e^2 V$ , where  $V$  is the source volume. BCK assumed that a kernel was heated until the time of peak emission, and that no further heating occurred thereafter. They also assumed that  $n_e$  remained constant. This assumption was considered justified because the expansion of the source is primarily a conductive process, rather than a hydrodynamic expansion. Under these assumptions, if radiative energy losses can be neglected during the decline in emission from such a kernel, then conservation of energy implies that the quantity  $\mu(t)T_e(t)$  would be constant, equal to  $\mu_0 T_{e0}$ , where the noughts designate values at the time of peak hard X-ray emission.  $T_e$  and  $\mu$ , therefore, should be inversely related. The observed relationship had been studied by Mätzler et al. (1978), who presented correlation diagrams of  $T_e$  and  $\mu$  for the flares of 1969 March 1 and 1970 March 1. In these two flares, the only events observed with sufficient counting statistics for such an investigation,  $T_e$  and  $\mu$  were instead positively correlated. Having concluded that a single kernel of the BMS type could not explain these bursts, BCK then developed a more complex model in which numerous small kernels of the BMS kind were produced at a time-varying rate such that the observed relation between  $T_e$  and  $\mu$  was the result.

The foregoing argument does not rule out the single kernel model for two reasons. First, hydrodynamic motions play a role in the simulations of Smith and collaborators, a role which depends on the heating rate, and can alter  $\mu$  by changing  $n_e$ . BCK assumed  $n_e$  to

be constant. Secondly, in the simulations of SH1 and SH2 the decline of hard X-ray emission is determined by competition between continuous heating and the convection or evaporation of cooler, chromospheric gas into the source, not just the conduction that BCK used to derive  $\tau_{cool}$ . For both of these reasons, the simple anticorrelation of  $T_e$  and  $\mu$  resulting from the assumptions of BCK is not expected to hold in general. In fact, a variety of relationships between  $T_e$  and  $\mu$  have been observed, some of them quite different from the correlations of Mätzler *et al.* (cf. Wiehl, Schöchlin, and Magun 1980; Wiehl *et al.* 1983). The relationship between  $T_e$  and  $\mu$  in the simulations of SH1 and SH2 would clearly depend on the heating rate and its spatial variation, which the observations are still inadequate to determine. It appears likely that the model can reproduce the observed range of relationships by means of appropriate choices of the heating rate and its spatial variation, although this has not been investigated.

### 3.2 The High-Energy Limit of Confinement and Its Implications for Microwave Emission

For a Maxwellian distribution with  $T_e \sim 10^8$  K in a region with  $B \sim 100$  G, most of the microwave flux is emitted by electrons in the tail of the distribution with kinetic energy in the range  $6 kT_e \lesssim E \lesssim 12 kT_e$  (Mätzler 1978). This corresponds to speeds of  $v \sim 3 v_e$  for typical sources considered in Chapter V, for which  $T_e \sim 3 \times 10^8$  K. It was first shown by BMS that the conduction fronts are transparent to tail electrons with velocities normal to the front in excess of some

threshold. If the coordinate  $x$  is along the arch in the direction away from its apex, as shown in Figure 3-1, then the component of an electron's velocity normal to the front is  $v_x$ . A detailed calculation by Smith and Brown (1980, hereinafter SB) suggested that this threshold was  $v_x \approx 2 v_e$ , corresponding to a kinetic energy of  $2kT_e$  associated with  $v_x$  (that is,  $m_e v_x^2/2$ ). Thus the fraction of the distribution with  $v < 2 v_e$  ( $E < 2kT_e$ ), approximately 74%, is confined by the conduction front.

As a result of the preceding analysis regarding escape of electrons with  $E > 2kT_e$ , no detailed predictions of microwave spectra were made by Smith and collaborators because they believed the microwave source electrons escape from the source, through the conduction fronts. Under these conditions, the escaping tail would not be relaxed, and would evolve independently of the thermal electrons. Consequently, the microwave emission has not been widely regarded as originating in a distribution of Maxwellian form, and the dynamics of the escaping tail have been treated as separate from the dynamics of the confined thermal electrons in this model. Flare emissions from electrons at energies above the threshold were studied qualitatively by Vlahos and Papadopoulos (1979). A particular functional form of the escaping electron distribution was considered by Emslie and Vlahos (1980), who calculated the resulting microwave spectrum and showed that it differed markedly from the spectrum of the confined source alone.

Clearly, then, the appropriateness of the treatment of the problem by SB, and the value of the escape threshold, are critical to any attempt to calculate the microwave spectrum expected in the conduction-front model. To begin, we shall re-examine the arguments advanced by SB

regarding electron confinement, and its consequences for microwave emission. In the following discussion, the analysis of SB is shown to be inadequate, primarily because the one-dimensional treatment of the electron velocities is inappropriate. Factors that contribute to a threshold effectively much higher than  $2kT_e$  are then described. On the basis of these arguments, it is suggested that the confined source would in fact possess a well-developed Maxwellian tail, and that microwave emission with a spectrum characteristic of this distribution is expected, originating in the confined source.

### 3.2.1 Limits on the Confinement of the Electrons Derived by SB

The same one-dimensional expansion as studied by BMS and SL was considered by SB. In this latter work, however, the ion-acoustic waves excited in the conduction front were treated more realistically. BMS had assumed that the ion-acoustic turbulence was isotropic, and that resonant scattering of the escaping electrons by the waves was the dominant confinement mechanism. Instead, theory and experiments with such current-driven waves show that only waves that propagate in directions within a cone of opening angle  $\sim 45^\circ$  around the direction of the return current electron drift are excited (Sagdeev and Galeev 1969). As a result, the resonance condition that must be met for an electron to be scattered by the turbulent waves is  $\omega_s \approx \vec{v} \cdot \vec{k}_s$ , where  $\omega_s$  is the frequency of the wave,  $\vec{v}$  is the velocity of the electron, and  $\vec{k}_s$  is the wave vector. For ion-acoustic waves,  $\omega_s/k_s \approx c_s \ll v_e$ . Because the waves propagate within  $45^\circ$  of the direction opposite to the motion of the front, and because  $v \sim v_e$  for the bulk of the electrons, the

resonance condition can only be met for  $\vec{v}$  approximately perpendicular to  $\vec{k}_s$ . In the one-dimensional analysis of SB, there are no electrons with such velocities. Hence, SB regarded resonant scattering of the hot source electrons by the waves as insignificant, and concluded that scattering is not the dominant process that confines the hot electrons. Rather, in their analysis, the bulk of electrons are returned to the source by the thermoelectric field that develops within the front due to the electron temperature gradient,  $\partial T_e / \partial x$  (see Figure 3-1). SB calculated the potential,  $\bar{\Phi}$ , due to the thermoelectric field, using marginal-stability conditions for the ion-acoustic turbulence, and showed that  $\bar{\Phi} \approx 2kT_e/e$ . Consequently, only electrons with  $v_x > 2v_e$  and kinetic energy  $E > 2kT_e$ , could surmount the barrier and cross the front. Such electrons would thereby lose  $2kT_e$  of kinetic energy in escaping from the confined thermal source. For these reasons, SB suggested that most of the microwave emission would come from the escaping component of the distribution, and they did not address the microwave emission any further. SB even questioned whether the escaping component could be produced by heating in a source confined by a collisionless conduction front. Citing the results of the numerical analysis by MacDonald, Rosenbluth, and Chuck (1957), SB argued that plasma heating would immediately establish an electron distribution with nearly Maxwellian form only for electron velocities  $v \sim v_e$ ; the tail of the distribution, containing the microwave-emitting electrons, would require a few times  $\tau_M(v') = \lambda(v')/v'$  to be populated up to velocity  $v'$ . The parameter  $\lambda(v)$  is the electron collisional mean free path in the absence of turbulence (cf. Montgomery and Tidman 1964), given approximately by

$$\lambda(v) \approx 10^{-20} v^4 / n_e. \quad (3.1)$$

For  $v \sim 3 v_e$ ,  $\tau_M$  is typically a few seconds, about equal to the duration of the impulsive bursts to be explained. The time for such an electron to be lost by escape through the front is  $\tau_s \approx L/v$ . Characteristic source sizes are  $L \sim 10^4$  km, so the streaming loss time  $\tau_s \sim 0.01$  s. Because the loss time is much shorter than the production time of tail electrons by Coulomb collisions, few tail electrons would be expected to exist, confined within the thermal source. Thus, the assumption that the effects of the turbulence on the distribution would be negligible led SB to conclude that the production of tail electrons in the confined source would be greatly inhibited, and that the microwave emission from the confined source would be insignificant.

### 3.2.2 Population of the Maxwellian Tail

An important question raised by SB was whether or not the Maxwellian tail could be populated rapidly enough to establish a relaxed Maxwellian distribution. Populating of the tail in a confined source would be enhanced by the resonant scattering of hot electrons in the front by the ion-acoustic waves. Resonant scattering increases the effective collision rate and causes the electron distribution to relax more rapidly than by means of Coulomb collisions alone. As noted above, the resonance condition is  $\omega_s = \vec{v} \cdot \vec{k}_s$  ( $\vec{v}$  approximately perpendicular to  $\vec{k}_s$ ). SB regarded resonant scattering of the hot source electrons by the waves as insignificant because in their one-dimensional analysis, there are no electrons with such velocities. The analysis of SB leads to prediction

of a truncated Maxwellian distribution in the confined source, poorly populated at  $E \gtrsim kT_e$ . If the analysis of SB were correct, it would then be necessary to postulate acceleration of nonthermal electrons, in order to explain the microwave emission, as done by Emslie and Vlahos (1980).

It appears, however, that the one-dimensional picture is misleading, and that the resonance condition can easily be met. For those electrons with  $\alpha > 0$ , a one-dimensional description of their trajectories is inadequate. (The pitch angle,  $\alpha$ , is defined as  $\tan^{-1}(v_+/v_x)$ , where  $v_+$  is the component of velocity perpendicular to  $\vec{B}$ ). Consider a typical thermal electron in the confined source with  $v_+ = v_x = v_e$ . When this electron encounters the conduction front, the confining electric field reduces  $v_x$  continuously to  $-v_e$ ; i.e., the electron is reflected by the potential barrier of the front. Near the turning point of its motion,  $v_x \approx 0$ , but  $v_+ = v_e$ . At this point, the resonance condition for scattering by the ion-acoustic waves is satisfied, and the electron is likely to be scattered into another part of the Maxwellian distribution. Actually, because the wave vectors  $\vec{k}_s$  are distributed within a cone of about  $45^\circ$  half-opening angle, as shown in Figure 3-2, resonance can occur for pitch angles in the range  $135^\circ > \alpha > 45^\circ$ . The turbulent wave intensity decreases with  $\theta$  as shown in Figure 3-2, however, and a conservative estimate of the half-width of the wave spectrum is  $22^\circ$ . This resonant scattering relaxes the electron distribution by acting as a mechanism for energy exchange between the electrons.

The effect of the turbulence on the electron energy distribution function is found by consideration of the anomalous collision frequency,

defined by the relation  $\langle \vec{v} f_{AN} \rangle \equiv \langle d\vec{v}/dt \rangle$ . The anomalous collision time  $\tau_{AN} = 1/f_{AN}$  is the time required for wave-particle interactions to result in a change  $\Delta \vec{v} \approx \vec{v}$ .) The turbulence increases the collision frequency from the Coulomb collision rate,  $f_c$ , to the anomalous collision frequency (SB; Sagdeev and Galeev 1969)

$$f_{AN} \approx \frac{\omega_e u T_e}{4 v_e T_i} \left[ \frac{e\phi}{kT_e} \right]^2, \quad (3.2)$$

where  $u$  is the drift velocity of the current that maintains the turbulence, and  $e\phi/kT_e$  is the ratio of energy in the waves to the thermal energy. In the present case,  $u = c_s$ . (Equation 3.2 was derived for  $u \gg c_s$ , but the same result, within a factor near unity, was obtained by Mannheimer 1977, independent of this restriction.) SB derive  $e\phi/kT_e$  self-consistently, finding the value

$$\left[ \frac{e\phi}{kT_e} \right]^2 = \frac{8(2\pi)^{1/2}}{3\pi} \frac{k}{m_e \omega_e c_s} \frac{\partial T_e}{\partial x}. \quad (3.3)$$

Because the electrons are rapidly heated to  $T_e \sim 10^8$  K while the ions remain at the pre-flare temperature  $T_i \sim 10^6$  K, the ratio  $T_e/T_i$  can be set to  $\approx 100$ . The temperature gradient  $\partial T_e/\partial x \approx T_e/L_f$ , where  $L_f$  is the front thickness. The scattering mean free path of an electron in the turbulent region is  $\lambda_{AN} = v/f_{AN}$ , or, after substitution of the above values for  $(e\phi/kT_e)^2$ ,  $T_e/T_i$ , and  $\partial T_e/\partial x$ ,

$$\lambda_{AN} \approx \frac{3\pi v}{200(2\pi)^{1/2} v_e} L_f \approx 0.02 \frac{v}{v_e} L_f. \quad (3.4)$$

Estimates of  $L_f$  vary from a fraction of 1 km (BMS) to 100 km (SA), but this expression shows that  $\lambda_{AN} \ll L_f$ , whatever value is chosen for  $L_f$ . Thus the turbulence will act to relax the distribution for values of  $v$  such that  $\lambda_{AN} \lesssim L_f$ , subject to the condition that  $113^\circ > \alpha > 67^\circ$  (for resonance to occur). In particular, the part of the high-energy tail in the electron distribution which is responsible for microwave emission,  $v \sim 3 v_e$ , is populated by this relaxation process, as the following argument demonstrates. Electrons with  $v = 2v_e$  are confined in the thermal source (because  $E < e\Phi$ ), and are part of the isotropic, Maxwellianized part of the distribution with  $v \lesssim 2v_e$ . Due to the resonant wave-particle interactions, as they enter the front, these electrons will perform a "random walk" in energy and pitch angle. By the definition of  $\tau_{AN}$ , the random walk will result in a  $\Delta v_{rms} = N v$  after a time  $\approx N^2 \tau_{AN}$ , where  $N$  is the number of steps of the random walk. Therefore, the time for an electron with initial speed  $2 v_e$  to attain  $3 v_e$  is approximately  $\tau_3 \approx (3/2)^2 \tau_{AN} \approx 2 \tau_{AN} \approx 0.03 L_f/v_e$ . The timescale for a  $3 v_e$ -electron to be lost from the thermal source by streaming out is  $\gtrsim \tau_s = L/(3 v_e) \approx 0.3 L/v_e$ . Since characteristic source sizes are  $L \sim 10^4$  km, and  $L_f$  is expected to be 100 km or much less, in general  $\tau_s \gtrsim 100 \tau_3$ . Thus, the streaming of microwave-emitting electrons out of the source occurs so slowly as to be negligible in comparison with their production rate. The Maxwellian tail is, therefore, expected to be populated by means of wave-particle interactions in the range of pitch angles and energies necessary for microwave emission because this pitch angle range is specifically the range for which the resonance condition is satisfied. Electrons in this pitch angle range make up about 39% of an isotropic distribution, so at

least 39% of particles that would be present in the tail ( $v > 2 v_e$ ) of an isotropic Maxwellian should exist in the thermal source. Those electrons in the specified pitch angle range that are not confined by the potential barrier of the conduction front should still be confined to the arch by magnetic mirroring.

### 3.2.3 Re-evaluation of the Confinement Limits

Several factors ignored by SB contribute to better confinement of the tail electrons than is implied by the arguments in Section 3.2.1. First, the one-dimensional analysis is again misleading. Heating processes such as the tearing mode instability are expected to lead to a nearly isotropic initial distribution of pitch angles. Electrons of total energy much greater than  $2kT_e$  would be confined by the thermoelectric field, as long as the component of their velocity perpendicular to the conduction front,  $v_x$ , was less than  $2v_e$ . Because the magnetic field in the arch is also directed perpendicular to the conduction front, the confined electrons would have high pitch angles, and, consequently, emit microwaves with a high relative efficiency (cf. Ginzburg and Syrovatskii 1965).

A second factor contributing to enhanced confinement is that the thermoelectric field depends critically on the spectrum of the turbulent ion-acoustic waves. To simplify the calculation, SB, in effect, assumed a delta function spectrum, peaked at wave number  $k_s = 0.5/\lambda_{De}$  (where  $\lambda_{De}$  is the electron Debye length). The spectrum of waves in a real conduction front extends to higher wave numbers (see Figure 3-2, after Horton and Choi 1979). Contributions from higher wave numbers would

increase the thermoelectric field in a more realistic calculation. The value  $\bar{E} = 2kT_e/e$  derived by SB is used in the following discussion, but it should be considered a conservative lower limit. A higher value of  $\bar{E}$  merely strengthens the following arguments.

A third factor is the convergence of  $\vec{B}$  observed in coronal arches near their feet in the chromosphere (cf. Spruit 1981). This convergence enables an arch to act as a magnetic bottle. The boundary of the loss cone is  $\alpha_0$ , which is given by  $\alpha_0 = \sin^{-1} (B_{\text{apex}}/B_{\text{max}})^{1/2}$ . Electrons with pitch angles greater than  $\alpha_0$  would be reflected from the region of converging field, back into the source (cf. Boyd and Sanderson 1969). Most electrons that escaped through the conduction front, therefore, would be returned to the thermal source by magnetic reflection. The fraction of escaping electrons that can return can be estimated as follows. For a conservative value of the mirror ratio,  $B_{\text{apex}}/B_{\text{max}} = 0.5$ ,  $\alpha_0$  equals  $45^\circ$ . The fraction of escaping electrons that would be mirrored depends on their pitch-angle distribution. If the escaping electrons comprise an isotropic distribution, then approximately 70% of them would have pitch angles in the range  $135^\circ > \alpha > 45^\circ$ , and, therefore, would be reflected back into the source.

In fact, the pitch angle distribution of the electrons escaping from the front is more favorable for reflection than that, as shown by the following considerations. In Section 3.2.2, it is shown that electrons with  $E > 2kT_e$  can be produced with pitch angles in the range  $135^\circ > \alpha > 45^\circ$ , and, in fact, most will be produced in the range  $113^\circ > \alpha > 67^\circ$ . Those electrons that passed through the front would lose  $2kT_e$  of kinetic energy in the  $x$  direction in surmounting the potential barrier of the front, resulting in the reduction of  $v_x$

relative to  $v_+$ . Thus, all those that passed through the front would incur an automatic increase of pitch angle and be mirrored. (In returning to the thermal source, these electrons would regain the lost  $2kT_e$ , so there would be no net loss of energy by the tail electrons, and hence no net loss of electrons from the tail.) In a fully-populated Maxwellian, electrons for which  $E > 2kT_e$  make up approximately 26% of the distribution. According to the estimates in Section 3.2.2, the tail produced by resonant interactions with the anisotropic wave turbulence is at least 39% populated. Hence, the electrons in the tail comprise 10% of a fully-populated Maxwellian. Electrons for which  $E < 2kT_e$  make up approximately 74% of the distribution. Thus, the mechanisms postulated in this model will populate and confine 84% of a complete Maxwellian distribution.

To summarize the results of the foregoing discussion:

- (1) The rise time of the impulsive hard X-ray burst is expected to be  $L/c_s$  in the thermal model with conduction front confinement and continuous heating.
- (2) The Maxwellian tail would be populated up to the energy range necessary for microwave emission by wave-particle interactions.
- (3) A three-dimensional treatment of the wave-particle interactions is necessary to properly characterize the electron distribution in the confined source, in contrast to the one-dimensional analysis of SB. When this is done, it is seen that more than 39% of the electrons with energies greater than the threshold calculated by SB would

have pitch angles sufficiently high to be efficient producers of microwave emission and would be confined by the thermoelectric field or magnetic mirroring.

This picture is expected to be representative until the conduction fronts reach the chromosphere, and are disrupted; the foregoing points constitute revised predictions of the model.

### 3.3 A Test of the Model Based on the Revised Predictions

The model, incorporating the revisions discussed in Section 3.2, can be tested using available observations. The observations have been analyzed under the following assumption: the electron distribution in the source can be approximated by a Maxwellian function with the temperature  $T_e$  resulting in the production of bremsstrahlung characterized by the best fit to the hard X-ray spectrum. This makes it possible to determine source parameters from the microwave and hard X-ray observations. The model leads to a prediction of burst rise times as a function of spectral parameters alone.

The conduction front is assumed to move at the ion-acoustic speed  $c_s$ . The solar atmosphere is mostly hydrogen, so  $m_i$  is  $m_p$ , the proton mass, and it follows that  $c_s = 9100 T_e^{1/2}$ . The rise time,  $t_r$ , is equal to  $L/c_s$ , where  $L$  is the distance along the arch from the apex to the foot of the arch. Examination of the time histories shown by SH1 and SH2 indicates that the assumption of a constant front velocity equal to  $c_s$  gives  $t_r$  within a factor of 2. At the time of peak X-ray emission,  $L$  can be estimated from  $T_e$  and the microwave observations,

as described by Crannell *et al.* (1978). The microwave spectrum usually rises with frequency  $f$  to a peak flux  $S_{\max}$  at  $f_{\max}$ , and falls for  $f > f_{\max}$ . The part of the spectrum for which  $f \lesssim f_{\max}$  is generally attributed to optically-thick emission. For a homogeneous source, the spectrum is given by the Rayleigh-Jeans law:

$$S(f) = 1.36 \times 10^{-44} f^2 A_0 T_e, \quad (3.5)$$

where  $S$  is the microwave flux density at the Earth in Solar Flux Units (1 SFU =  $10^{-22}$  W m<sup>-2</sup> Hz<sup>-1</sup>),  $f$  is the frequency in Hz,  $A_0$  is the observed source area in cm<sup>2</sup>, and  $T_e$  is the source temperature in degrees K. To determine  $A_0$ , Equation (3.5) is solved, using values of  $f$  and  $S$  in the optically-thick part of the microwave spectrum obtained simultaneously with the measurement of  $T_e$ . The value of  $f$  to be used here is denoted  $f_2$ , the observing frequency below the observed  $f_{\max}$ . Use of  $f_2$  insures that the measurement is within the optically-thick portion of the spectrum. The value  $S_2 \equiv S(f_2)$  also is used. If the source is inhomogeneous and has an area that varies with  $f$ , as discussed in Section 2.4.6,  $S(f)$  often exhibits a spectral index,  $\alpha(f) = d \log S(f) / d \log f$ , less than 2 (e.g. Mätzler 1978). In such a case,  $S(f)$  is not given by Equation (3.5), but the value calculated using that expression may be regarded as an effective area characterizing the source, and  $T_e$  must be similarly regarded as an effective temperature. As stated in Section 2.4.6, considerations of an appropriate model for such an inhomogeneous thermal source lead to the conclusion that the central, hottest part of the source is responsible for the optically-thick emission of maximum frequency (Schöchlin and

Magun 1979; Dulk and Dennis 1982). Because this hottest part also dominates the hard X-ray bremsstrahlung emission, the area calculated using  $f_2$  and  $S_2$  in Equation (3.5) is, indeed, a physically significant value for  $A_0$ .

The time of peak X ray flux is presumably the time when the conduction fronts reach the footpoints and the source just fills the entire arch. At that time, there is no room in the arch for a possible separate, escaped component of high-energy electrons which might complicate the microwave spectrum. Thus,  $S_2$  and  $f_2$  at the peak of the impulsive burst can be used to determine an  $A_0$  characteristic of the entire arch.

The value of  $L$  must be derived from the observed area  $A_0$ , which is a function of three factors: the dimensions of the arch, the orientation of the arch, and the anisotropy of the microwave emission. The unknown dimensions of the arch are accounted for by the parameter  $\eta \equiv 2 L/w$ , the ratio of total length of the arch to its average width. The value of  $\eta$  varies from arch to arch; a value of order 5 can be regarded as typical. A given arch, if viewed from the side, has a projected area of about  $2 L w$ . Rotation to another orientation can reduce this by as much as a factor of  $\pi$ . The effect of microwave anisotropy can reduce the observed area by another factor of order 2, as can be seen by considering the simplified expression for  $f_{\max}$  of Dulk and Marsh (1982):

$$f_{\max} \approx 1.4 (n_e w)^{0.1} (\sin \theta)^{0.6} T_e^{0.7} B^{0.9} . \quad (3.6)$$

In this expression,  $\theta$  is the angle between the magnetic field

direction and our line of sight, and  $B$  is in gauss. Because  $f_{\max}$  is the frequency at which the emission changes from optically-thick to optically-thin, Equation (3.6) also indirectly expresses the variation of optical depth with  $\theta$ . Unless the arch is viewed directly from its side,  $\theta$  varies from point to point along the arch, and consequently the section of the arch with the maximum value of  $\theta$  dominates the spectrum at  $f_{\max}$ . Sections with smaller values of  $\theta$  are optically thick only at lower frequencies. Consideration of the weak dependence on  $\theta$  in Equation (3.6) suggests that this variation of optical depth with  $\theta$  could reduce  $A_0$  by as much as another factor of 2 in the case of a symmetrical arch. Because of the effects described in this paragraph, the inequality,  $A_0 \lesssim 2 L w \lesssim 2\pi A_0$ , is expected to hold for each impulsive burst, resulting in an intrinsic scatter in the correlation between the observed rise times and those calculated with the present method.

It should be noted that the foregoing discussion of systematic uncertainties that contribute to the scatter may not be sufficiently exhaustive. For example, the arches could be nonuniform in temperature (cf. SA), and some arches could be asymmetrical, with different values of  $B$  at each foot. Each of these factors would affect the observed area. Imaging observations with good temporal and spatial resolution (which are not currently available) offer the only feasible means of sorting out these effects. On the other hand, if most flares occur in symmetrical arches with approximately uniform temperature, then the above inequality expresses the uncertainty in the predictions, as discussed below.

Substituting for  $w$  in the inequality and taking the square root

yields

$$(\eta A_0)^{1/2}/2 \lesssim L \lesssim (\pi \eta A_0/2)^{1/2}. \quad (3.7)$$

It is useful to define the derived scale length,

$$L_0 \equiv A_0^{1/2} = 8.6 \times 10^{21} (S_2/T_e)^{1/2} f_2^{-1}. \quad (3.8)$$

The inequality becomes

$$\eta^{1/2} L_0/2 \lesssim L \lesssim (\pi \eta/2)^{1/2} L_0. \quad (3.9a)$$

As an example, assuming typical arch dimensions,  $\eta = 5$ , leads to

$$1.1 L_0 \lesssim L \lesssim 2.8 L_0. \quad (3.9b)$$

The measured rise time,  $t_r$ , should be within a factor of order unity of  $\tau_0 \equiv L_0/c_s$ , the derived timescale. More explicitly,

$$\tau_0 = 2.8 \times 10^{14} S_2^{1/2} / (f_2 T_e). \quad (3.10)$$

In general, the measured rise time is predicted to lie in the range

$$\eta^{1/2} L_0/2 c_s \lesssim t_r \lesssim (\pi \eta/2)^{1/2} L_0/c_s. \quad (3.11a)$$

For a typical arch with  $\eta = 5$ ,

$$1.1 \tau_0 \lesssim \tau_r \lesssim 2.8 \tau_0. \quad (3.11b)$$

In summary, the model predicts a linear correlation between the measured rise time,  $t_r$ , and the parameter  $\tau_0$ , computed from the spectral parameters. The constant of proportionality is predicted to be of order unity for typical arch dimensions. The best way to test this prediction is to construct a correlation plot of  $\log t_r$  vs.  $\log \tau_0$ , which is done in Chapter V. An intrinsic scatter in the correlation is expected of about a factor of  $2.8/1.1 = 2.5$ , in the values of  $t_r$ .

### 3.4 Other Derived Parameters

The average density also can be calculated from the projected area and emission measure,  $\mu$ . The volume of the arch is approximately  $V = 2 \pi L (w/2)^2$ . From this formula, relation (3.9), and the definition of  $\eta$ , it follows that

$$\pi V_0 / (4 \eta^{1/2}) \lesssim V \lesssim \pi^{5/2} V_0 / (2\eta)^{1/2}, \quad (3.12a)$$

where  $V_0 \equiv L_0^3$  is the derived scale volume. For a typical arch with  $\eta = 5$ ,

$$0.35 V_0 \lesssim V \lesssim 5.5 V_0. \quad (3.12b)$$

From relation (3.12a), and the definition of emission measure,  $\mu = n_e^2 V$ , it follows that

$$\left[ \frac{4 \eta^{1/2} \mu}{\pi V_0} \right]^{1/2} \gtrsim n_e \gtrsim \left[ \frac{(2\eta)^{1/2} \mu}{V_0} \right]^{1/2} \pi^{-5/2}, \quad (3.13a)$$

where  $n_0 \equiv (\mu/V_0)^{1/2}$  is the derived scale density. For  $\eta = 5$ ,

$$1.7 n_0 \gtrsim n_e \gtrsim 0.43 n_0. \quad (3.13b)$$

(This estimate may be misleading, however, if there are large density gradients.)

The magnetic field in the plasma also can be calculated though the use of Equation (3.6). Because the source is assumed to be an arch, the portions of the arch with maximum  $\theta$  will dominate the emission. It is assumed here that  $\theta = 80^\circ$ . The systematic uncertainty introduced by this assumption is small because of the weak dependence of  $f_{\max}$  on  $\sin \theta$ . The very weak dependence of this expression on  $n_e$  and  $w$  allows mean values of these parameters to be used without introducing large uncertainties. If  $n_e$  is given the value  $n_0$ , and  $w$  is given the value  $2 L_0/5$ , corresponding to  $\eta = 5$ , Equation (3.6) can be solved for  $B$ , yielding

$$B = 0.77 (n_0 L_0)^{-0.1} T_e^{-0.8} f_{\max}^{1.1}. \quad (3.14)$$

Another quantity of interest is the thermal energy density in the plasma,  $w_T = (3/2) n_e k T_e$  (assuming  $T_e \gg T_i$ , the ion temperature), easily obtained from relations (3.13a). The total energy of the thermal plasma is given by  $U = w_T V$ . The plasma  $\beta$  is defined as  $w_T/w_B$ , where  $w_B = B^2/8\pi$  is the energy density associated with the magnetic

field. (If the magnetic field is to be capable of preventing the source from expanding laterally,  $\beta$  must be less than unity. The dynamics of the emission would be so altered by the expansion anticipated in a high- $\beta$  plasma that the analysis in this paper would be inadequate.)

The quantities  $w_T$ ,  $U$ ,  $w_B$ , and  $\beta$  are uncertain by the same multiplicative factor as  $n_e$ , about 4 in the case of  $\eta = 5$ . Useful estimates,  $w_{T0}$ ,  $U_0$ ,  $w_{B0}$ , and  $\beta_0$ , are derived by using  $n_0$  as an estimate of  $n_e$ .

### 3.5 Efficiency of the Conduction Front Model

As shown by SL, the bremsstrahlung emission efficiency of the model is the ratio of the bremsstrahlung energy loss rate to the heating rate required to balance conduction losses. The bremsstrahlung emissivity of a thermal source is (Tucker 1975)

$$j(T_e) = 2.4 \times 10^{-27} T_e^{1/2} n_e^2, \quad (3.15)$$

in the units  $\text{erg cm}^{-3} \text{ s}^{-1}$ . The total bremsstrahlung loss rate is computed from this expression by multiplying by  $V/A$ , the ratio of the volume of the source to its area. For the geometry considered here,  $V/A \approx (\eta L/2)/(\eta + 1)$ . (SL merely used  $V/A = L$ .) The conduction loss rate is just  $c_s w_T$ , corresponding to the conduction of thermal energy along the arch, which is limited by the velocity of the conduction front. At  $t_{\text{peak}}$ ,  $L$  is approximately  $c_s t_r$ , so the efficiency of the thermal source at this time is

$$\eta_{cf} \approx \frac{j(T) (V/A)}{c_s w_T} \approx 5.8 \times 10^{-12} T_e^{-1/2} n_e t_r \frac{\eta}{\eta + 1}. \quad (3.16)$$

This is to be compared with the efficiency of a thick-target model of the same source,  $\eta_{tt}$ , given by Equation (2.14). The relative advantage in efficiency of the conduction front model over the thick-target model is  $\eta_{cf}/\eta_{tt}$ , or

$$\xi \approx 1.3 \times 10^{-5} \frac{\gamma - 2}{\gamma - 1} \frac{n_e t_r}{T_e^{1/2} E_0} \frac{\eta}{\eta + 1}. \quad (3.17)$$

In this expression,  $\gamma$  is the best-fit power-law index of the hard X-ray spectrum at  $t_{peak}$ ,  $T_e$  is the electron temperature of the best-fit thermal bremsstrahlung function of the spectrum at the same time, and  $E_0$  is the low-energy cut-off in the assumed power-law electron distribution.

It should be noted that a different expression for this quantity is given by SL. The bremsstrahlung emission efficiency of the entire thermal electron distribution is compared by SL with the efficiency of a single electron in a power-law distribution. This is not a proper comparison unless the energy of the electron is taken to be  $E_0$ , which was not done by SL. The value of  $E$  used by SL was 41 keV;  $E_0$  is typically estimated to be 16 keV or less (e.g. Hoyng *et al.* 1983; Kahler and Kreplin 1971). The correct value of  $V/A$  also was not used by SL. These omissions resulted in an underestimate of the relative efficiency advantage of the conduction front model by a factor of 2 or more, depending on  $E_0$  and  $\eta$ .

## Chapter IV

### OBSERVATIONS AND DATA REDUCTION

#### 4.1 Hard X Rays

##### 4.1.1 The Hard X-Ray Burst Spectrometer

Since 1959, many spacecraft have carried hard X-ray detectors, and thousands of the hard X-ray bursts that usually accompany flares have been studied. The Hard X-Ray Burst Spectrometer (HXRBS) is the fifth in a series of scintillation spectrometers designed specifically for flare observations, and has been described in detail by Orwig, Frost, and Dennis (1980). The HXRBS is one of eight instruments aboard the SMM spacecraft, which orbits the Earth in a circular orbit with an altitude of 500 km and an orbital inclination of  $33^{\circ}$ . The orbital period is 95 minutes, of which 60 to 65 minutes are spent in sunlight, and the remainder behind the Earth. During 1980 and 1981, when the flares analyzed herein were observed, the duty cycle for the detection of solar flares was about 60%.

High time resolution and accurate absolute timing are required to study the most rapid flux variations in solar hard X-ray bursts. The time resolution of the HXRBS spectral data is 0.128 s. Variations that are still unresolved on this timescale have been found to be very rare.

(Kiplinger et al. 1983). The instrument also returns the counting rate, integrated over the entire range of energy, at a time resolution of 1 ms if the count rate exceeds  $800 \text{ counts s}^{-1}$ . The absolute timing is accurate to  $\pm 3$  ms. This is more than adequate for comparisons with other observations, such as the microwave data. To be useful, observations obtained with a hard X-ray burst detector must not be compromised by detector saturation effects. Saturation can be caused by paralysis of the counting system at high count rates, overflow of a count register, or other instrumental problems. No saturation of the HXRBS has occurred to date. Pulse height spectral data can also be compromised by pulse pile-up, an instrumental problem which is described in Section 4.1.3. Pulse pile-up affected the HXRBS data significantly in many cases, but the data were corrected for this effect, as well as for the other factors that affect instrument response.

A cross sectional view of the detector is shown in Figure 4-1. The scintillation material is CsI(Na). The central crystal has a sensitive area of  $71 \text{ cm}^2$ , and is used for viewing the Sun. The anticoincidence shield is used to collimate the detector by rejecting counts collected by both the shield and the central crystal. The collimator geometry provides a field of view of  $40^\circ$  FWHM, and the satellite's orientation keeps the field centered on the Sun. Aluminum windows are used to attenuate the large fluxes of solar soft X rays with energies  $< 30 \text{ keV}$  which would otherwise distort the measured hard X-ray spectra by pulse pile-up. In-flight calibration of the central detector is performed by detection of  $59.6\text{-keV}$  X rays emitted by an  $\text{Am}^{241}$  radioactive source located in the field of view.

Pulse height spectral data were obtained every  $0.128 \text{ s}$  for each of

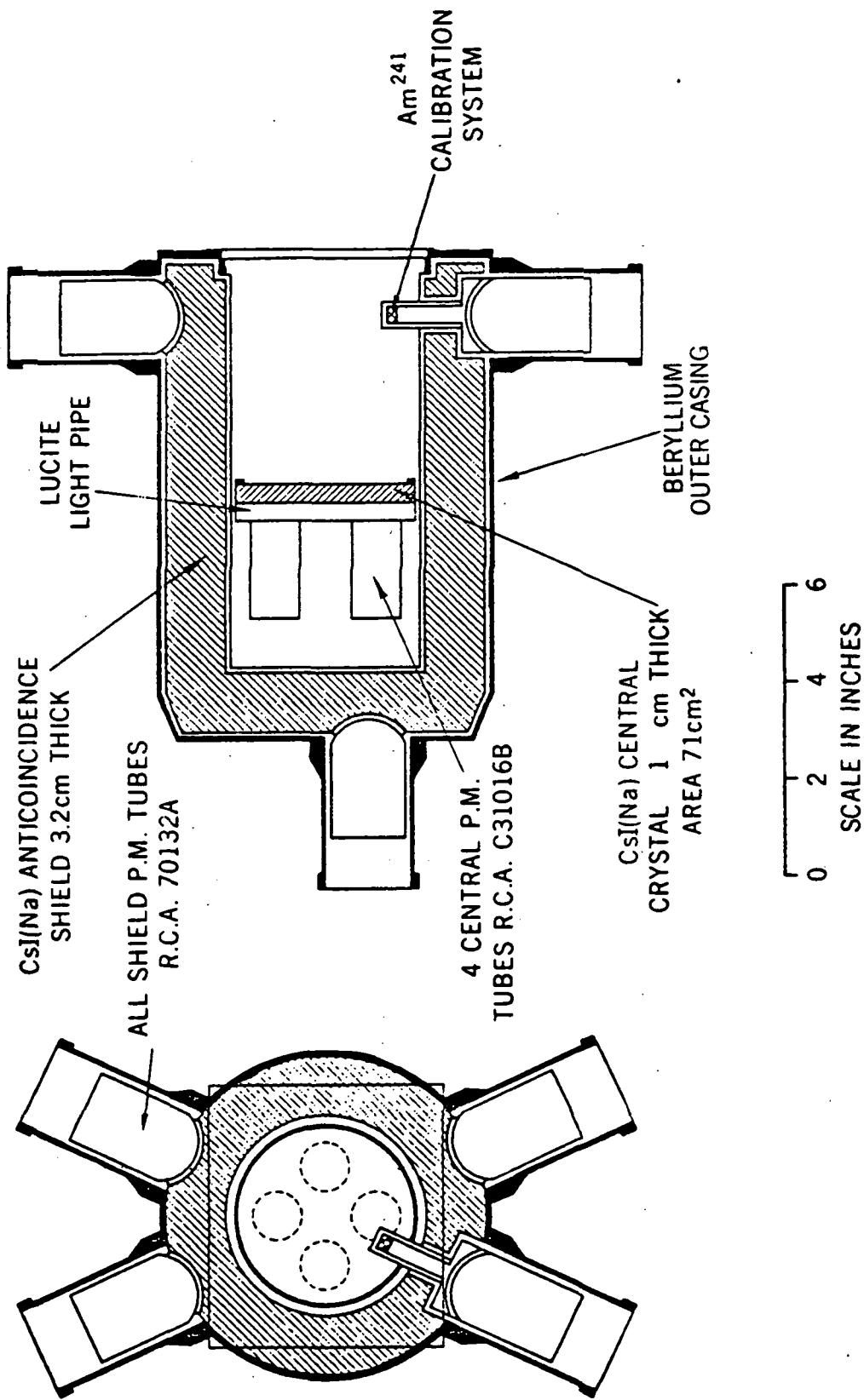


Figure 4-1. Cross-sectional view of the Hard X-Ray Burst Spectrometer.

15 channels distributed over the instrument's energy range of sensitivity. The energy range has varied slowly and monotonically since launch. In 1980 March it was 26 to 456 keV, and in 1981 December it was 30 to 531 keV. A detailed description of this behavior and a listing of events observed with HXRBS are available in Dennis et al. (1983). The measured energy resolution at 122 keV is 30% FWHM.

#### 4.1.2 Instrumental Effects

Because of the limited energy resolution of scintillation detectors, and the complexity of the instrument response, the form of the incident photon flux density must be derived by an iterative method. A functional form for the incident photon flux density is assumed on physical grounds, which are discussed in Chapter II. This assumption is then tested for consistency with the measured pulse height spectral data by means of an iterative technique described in Section 4.1.5.

The incident spectra are most often assumed to have one of two possible functional forms: the power law (Equation 2.1), and the thermal bremsstrahlung function (Equation 2.2). The response function of the detector depends critically on the form of the incident photon spectrum, as described in the following section.

To determine the incident photon spectra from the measured pulse height spectra, the response function of the instrument had to be taken into account. The theory and practice of scintillation counting is discussed in detail by Birks (1964). A brief summary of the principles of the HXRBS detector is given here. The instrument was designed to detect photons primarily by means of the photoelectric effect in the

scintillation crystal. That is, an incident photon interacts with the central detector crystal by being absorbed by an atom of the crystal, which ejects an electron with energy equal to the energy in the incident photon, minus the electron's atomic binding energy. These photoelectrons are then stopped in the crystal, producing a flash of light (scintillation) with an integrated intensity proportional to the energy of the incident photon (minus the electron's binding energy). The flash is detected with a photomultiplier tube, and the resulting signal is used to produce a voltage pulse in the instrument electronics with an amplitude proportional to the integrated light intensity. This voltage pulse is sent to the pulse height analyzer, which measures its amplitude and increments the number of counts in the corresponding channel.

Although most of the photons interact with the detector by means of the photoelectric effect, additional photons can be detected as a result of Compton scatterings in the central crystal, whether the scattered photon is totally absorbed or escapes. For example, at a photon energy of 100 keV, the probability of a photoelectric interaction in the central crystal is 85%, and the probability of a Compton scattering is 7%. In the case of a Compton-scattered photon that escapes, the detected scintillation registers only a fraction of the incident photon energy. Some of the ejected photoelectrons come from an inner atomic shell (typically the K shell or the L shell), leaving the ionized atom in a highly excited state, with a vacancy in an inner shell. The excitation energy of the ion is released in the form of low-energy X-ray photons or electrons (known as Auger electrons) which are emitted when electrons from outer shells of the ions fall into the inner-shell

vacancies created by the ejected photoelectrons. The highest-energy photons from this relaxation process (approximately 30 keV) are emitted when an electron falls into a K-shell vacancy. Such an electron generally comes from the L shell. The photons produced by this process escape from the ion with insufficient energy to knock out a K-shell electron from a neighboring atom, and therefore have a high probability of escaping from the crystal without interacting. These K-escape photons do not contribute their energy to the scintillation, and thus, as stated above, the energy recorded by the spectrometer is approximately 30 keV less than the energy of the incident photon. The probability of this process has been computed by Rieger (1969); it is about 27% at 30 keV, and falls to 5% at 100 keV.

An additional complication in the response of the detector to a given incident photon spectrum is introduced by other types of X-ray interactions which are possible in the CsI(Na) crystal itself, the aluminum window, and the so-called "dead layer" on the crystal. First, as mentioned previously, the X-ray flux at photon energies,  $\epsilon$ , less than 30 keV is strongly attenuated by the aluminum window. The purpose of the window is to attenuate the very intense soft X-ray flux from the flare, which otherwise would distort the measured spectra by the process of pulse pile-up. In addition, there is a dead layer on the surface of the crystal which does not scintillate. This is the result of a chemical reaction of the Na activator with ambient water vapor to form NaOH, which occurred prior to launch of the spacecraft (Goodman 1976). Photoelectric interactions in this dead layer, while not resulting in scintillation, nevertheless give rise to 30-keV K-escape photons, some of which pass into the "live" central portion of the crystal. For

reasons mentioned previously, these K-escape photons do not have a high probability of interacting with the crystal, but they do give rise to some extraneous scintillations. Photons also can be Compton backscattered into the central crystal from parts of the detector behind the central crystal, where they are detected at only a fraction of their incident energy. Also, photons that are Compton scattered from the central crystal into the anticoincidence shield with energies greater than the threshold of the shield, between 100 and 200 keV, may be rejected by the anticoincidence circuit.

The counting rate distribution as a function of energy that results from all of these interactions is actually measured with an energy resolution  $\sigma(\epsilon) = 0.75 \epsilon^{0.75}$  keV. This results in a redistribution of counts from a given channel into its neighboring channels, equivalent to convolving the counting rate distribution with a Gaussian function of standard deviation  $\sigma(\epsilon)$  (e.g. Datlowe 1975).

A detailed, quantitative description of the contributions to the counting rate distribution that arise from the above effects can be found in Dennis (1981). The interactions described in the previous paragraph result in a net detection efficiency as a function of incident photon energy that is shown in Figure 4-2 (Dennis, private communication). Further information about detectors such as HXRBS may be found in Frost (1969).

At high counting rates, the instrument response is also affected by pulse pile-up. That is, voltage pulses arrive at the pulse height analyzer at such a high rate that there is a significant probability of the superposition of two or more voltage pulses. In such a case, the analyzer incorrectly records a single count in a channel corresponding

# HXRBS DETECTION EFFICIENCY VS PHOTON ENERGY

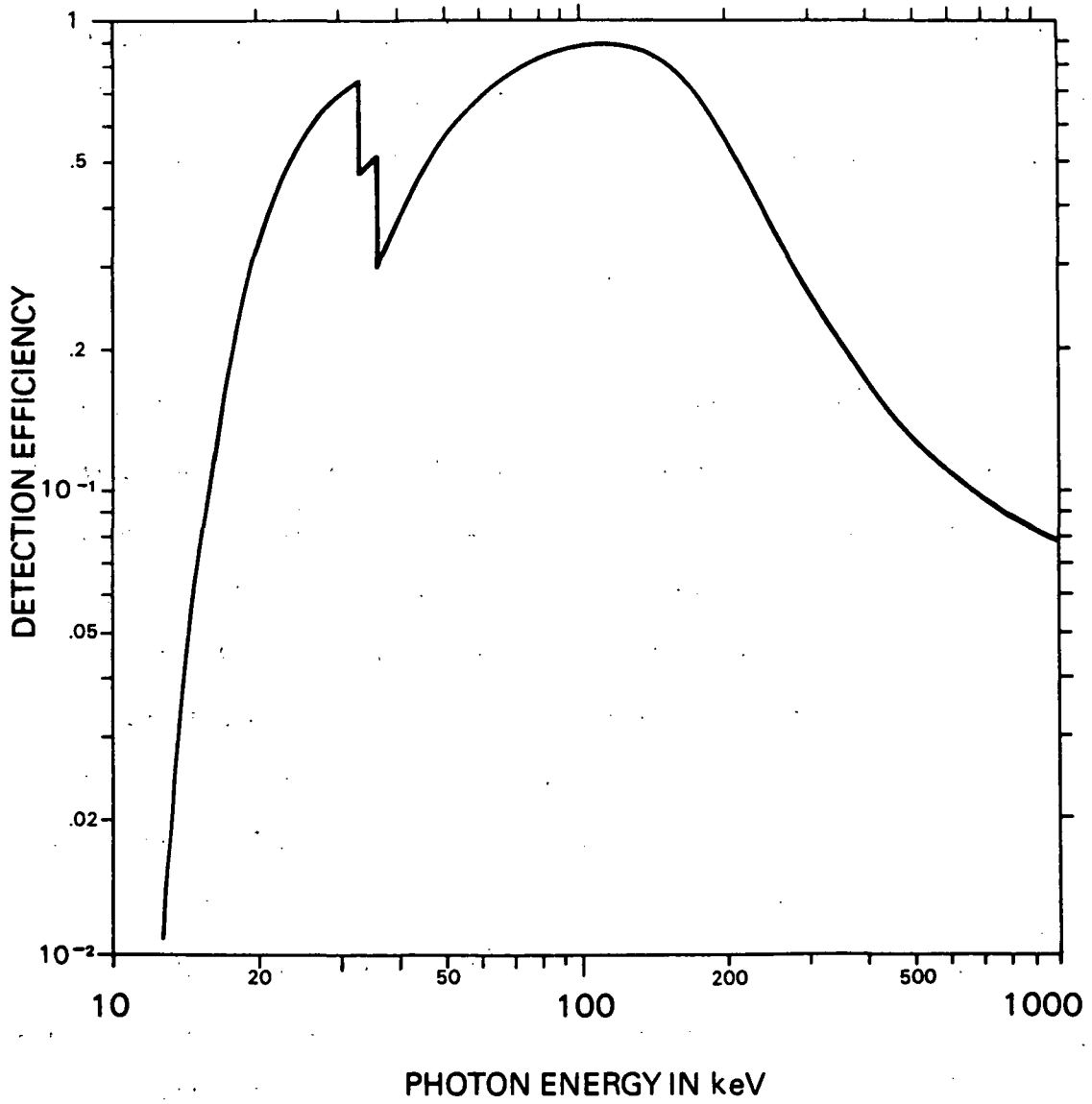


Figure 4-2.

to the maximum voltage of the pulse. In the case of solar flare spectra, which decline steeply with increasing energy, the effect of pulse pile-up is to reduce the counting rate at low energies and increase it at high energies, reducing the steepness of the measured distribution. For example, the flare of 1980 March 29, 0918 UT, reached a peak counting rate of 19,000 counts  $s^{-1}$ . Without correction of the spectrum for pulse pile-up effects, the fitted temperature at the peak was measured as  $\approx 40$  keV; correction of the spectrum by means of the method described in the Appendix resulted in a value of  $\approx 30$  keV.

#### 4.1.3 Simulation of the Instrument Response

The instrumental effects described in Section 4.1.2 result in a very complex instrument response to a given incident photon spectrum. Ideally, one would use laboratory continuum X-ray sources with thermal bremsstrahlung spectra of various temperatures and power-law spectra with various spectral indices to calibrate the detector. Indeed, a continuum lab source was used in a pre-launch test of HXRBS (Orwig, Frost, and Dennis 1980), but the source produced a very hard spectrum which was only marginally useful for calibrating the HXRBS response to softer sources, of whatever form. In fact, suitable laboratory calibration sources are exceedingly difficult to obtain. Most laboratory sources are likely to be contaminated by X-ray spectral lines which are characteristic of their containers. In addition, the only ways to adjust the source intensity would be to collimate or attenuate the source, or to vary the distance from source to detector. All of these techniques would either alter the spectrum or introduce complex

geometrical effects, which would be difficult to distinguish from the change in response that was due to the intensity variation alone. Therefore, as mentioned briefly in Section 4.1.2, the method adopted for correcting for instrument response is a form of self-calibration, by first assuming an incident spectrum, and then testing this assumption for consistency with the measured pulse height spectral data. As a prelude to correcting the data for the instrumental effects just described, the processes mentioned in Section 4.1.2 were simulated by means of a FORTRAN program. The operations performed by the program were as follows:

A spectrum of power-law form (Equation 2.1) or thermal form (Equation 2.2) was assumed. The spectral range from 5 to 1200 keV was divided into 200 bins, each with center  $s_i$ . For each value of  $s_i$ , a value of the function  $I_i \equiv I(s_i)$ , in units of photons  $s^{-1} \text{ cm}^{-2} \text{ keV}^{-1}$ , was calculated. (Note: the number of energy bins, 200, was much larger than the number of channels of HXRBS, 15, in order for the calculation to represent accurately the steep incident spectra.) Calculations by Dennis (1981) of the instrumental effects described in Section 4.1.2 were used to obtain a new array  $S_i$ . The array  $S_i$  contained the estimated counting rate that would be observed in each of the 200 bins. Calculation of  $S_i$  from  $I_i$  is referred to as convolving the incident spectrum with the instrument response function of the detector. The two fit parameters that determine the function  $I(s)$ , and the output array,  $S_i$ , were stored together in a disk file. In the case of a power-law spectrum (Equation 2.1), the fit parameters were  $K_\gamma$  and  $\gamma$ ; in the case of a thermal spectrum (Equation 2.2), the fit parameters were  $K_T$  and  $T$ .

For each of the two assumed functional forms, a table of fit parameter pairs was selected, and the procedure described in the preceding paragraph was performed for each pair in the table. The fit parameter pairs in the table were chosen so as to span the space of possible incident spectra closely enough so that output arrays corresponding to intermediate pairs could be obtained by interpolation, with an accuracy of 10% of the count rate  $S_1$ . The ranges of the best-fit parameters  $T$  and  $\gamma$  for the two assumed spectral forms are discussed in Section 2.3.1. The ranges of  $K_T$  and  $K_\gamma$  were governed by the maximum intensity of observed flares and the minimum detectable intensity for spectral analysis. The two fitting tables could then be used as described in Section 4.1.4 to determine the best fitting function of the selected form to the incident spectrum.

The program used for simulation of instrument response effects in HXRBS data is the most sophisticated and exhaustive thus far developed for any solar burst spectrometer. Details of the calculations, excluding the effects of pulse pile-up, are documented by Dennis (1981). The calculations of pulse pile-up effects were made using the techniques of Datlowe (1975, 1977). The necessary subroutines for the pulse pile-up calculations were developed by the author, and were adopted by the HXRBS instrument team as part of the instrument response simulation. Because of their value to other observers, the pulse pile-up simulation programs are documented and listed in the Appendix of this dissertation.

#### 4.1.4 Spectral Analysis Procedure

Best fit representations of the incident spectra are obtained by an iterative procedure, which is as follows.

- (1) Pulse height spectral data for a chosen time interval are obtained from archive tapes of the HXRBS data, and stored in a file on disk.
- (2) A spectral form is assumed by the user, either a thermal function or a power law, and a corresponding initial estimate is made of the fit parameter pair,  $(K_T, T)$  or  $(K_\gamma, \gamma)$ , which is based on typical values of the fit parameters (see Section 4.1.4). Using this estimate, the corresponding output array  $S_i$  is obtained from the table described in Section 4.1.3.
- (3) The output array  $S_i$ , a 200-bin representation of the observed count rate distribution for the selected fit parameters, is compressed into a 15-bin representation corresponding to the HXRBS energy channels on the date of observation. (As noted in Section 4.1.1, the channel edges have shifted slowly and monotonically to higher energies since launch.)
- (4) A 200-bin representation of the incident photon spectrum is computed for the chosen fit parameters from step (2), and compressed to yield the differential photon flux in each of the 15 channels of HXRBS on the day of observation.

- (5) The 15 values found in step (4) are divided by the 15 values found in step (3), yielding a conversion factor from count rate to incident differential photon flux for each of the 15 channels.
- (6) The pulse height spectrum stored on disk in step (1) is converted to an estimated differential photon spectrum, using the conversion factors obtained in step (5).
- (7) Using a linear least-squares fitting method, a model spectrum of the chosen functional form which best fits the estimated photon spectrum is computed. This usually results in fit parameters which are different from the initial estimate. This fitting method is designed to obtain a model spectrum with the minimum  $\chi^2$ , and is given by Bevington (1969, Chap. 11, subroutine 11-5, entitled CURFIT).
- (8) The best fit parameters found in step (7) are used as the next estimates for step (2). Steps (2) through (8) are repeated until the value derived for each parameter differ by less than 10% from its value on the previous iteration (approximately the uncertainty in each parameter).

The procedure described above is represented as a flow chart in Figure 4-3. Fit parameters derived by means of this iterative procedure usually converge in 3 to 5 iterations, to yield the best fit parameters.

The spectral analysis procedure employed in this work is not a deconvolution method, such as is often used in the analysis of

# FLOW CHART OF SPECTRAL ANALYSIS PROCEDURE

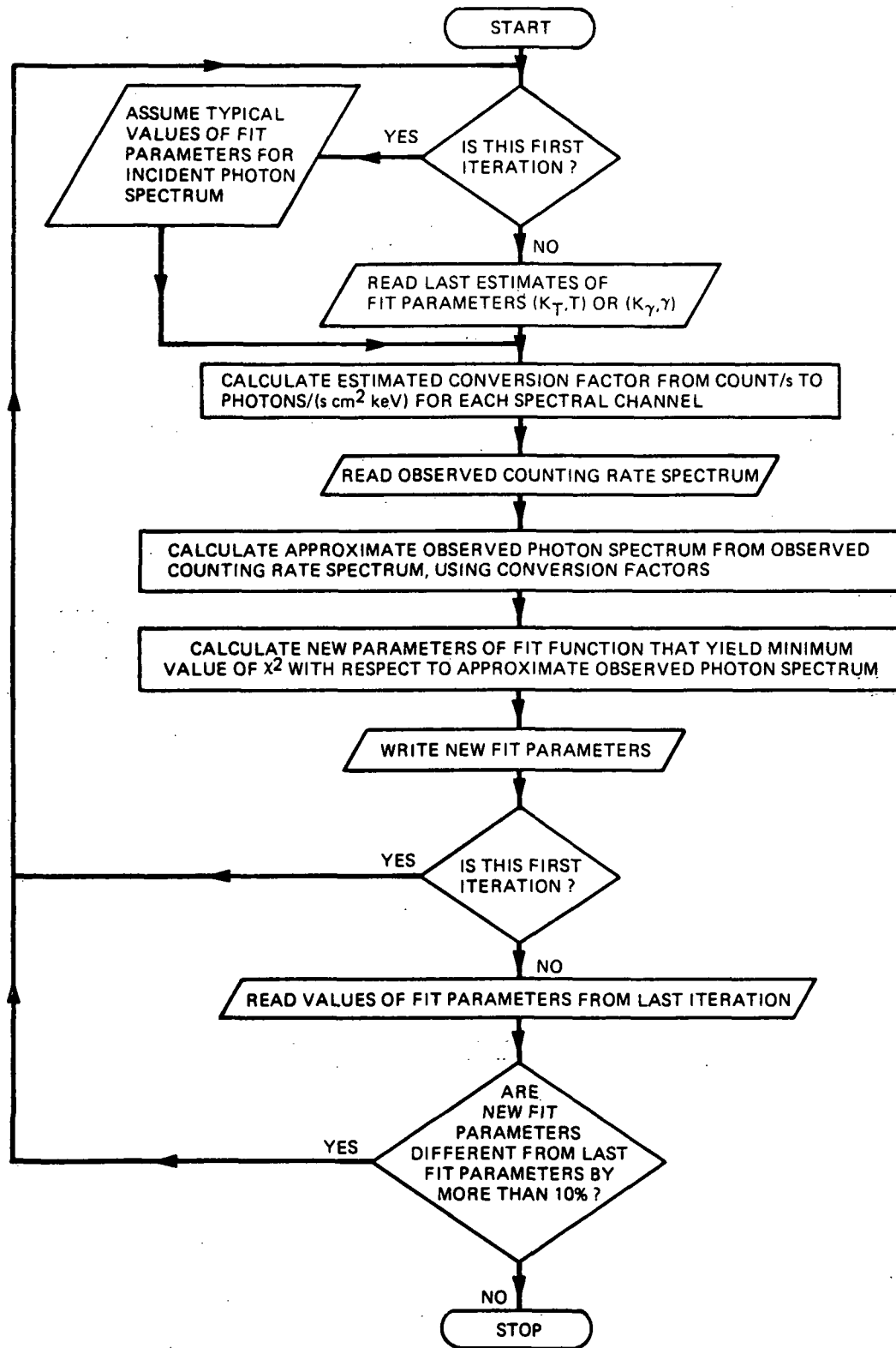


Figure 4-3.

scintillation counter data. A true deconvolution requires the inversion of spectral response matrices (e.g. Dolan 1972), and sometimes involves computational difficulties due to vanishing determinants. The procedure used here, in effect, matches the convolved form of a model theoretical spectrum with the observed pulse height spectrum, and presents the results in terms of the two parameters that determine the theoretical spectrum. This procedure serves the same purpose as a deconvolution, but has the advantage of computational efficiency.

It should be noted that spectral fits performed for this work were made with the exclusion of Channel 1 of HXRBS. This lowest-energy channel of the spectrometer has a narrow width,  $\approx 4$  keV, much narrower than the widths of the other channels, which are 22 keV wide or more. The calibration and precise width of Channel 1 are highly uncertain, and consequently, if used, would contribute unreliable information.

Photon spectra from HXRBS have been compared with photon spectra obtained from simultaneous observations with a hard X-ray detector on the International Sun-Earth Explorer-3 spacecraft, resulting in agreement to better than 20% of the photon flux (Kane, private communication).

## 4.2 Microwaves

### 4.2.1 Spectral Coverage and Temporal Resolution

The University of Bern operates 7 fixed-frequency, heterodyne receivers. A detailed description of the facilities and instrumentation at Bern is given by Magun et al. (1981). For the flares analyzed

herein, data are available at most of the following frequencies: 3.2, 5.2, 8.4, 10.4, 11.8, 19.6, 35, and 92.5 GHz. These frequencies span nearly the full range of interest for microwave emission from solar flares. In two cases, time histories of 2.8 GHz emission obtained at Algonquin Radio Observatory in Ottawa, Canada, were used to supplement the coverage when no 3.2 GHz data from Bern were available.

Temporal resolution of quiet-Sun observations is 1 s. The resolution changes automatically to 0.1 s at the start of a burst. Absolute universal time with an accuracy of 100  $\mu$ s is derived from a standard frequency reference from Prangins, Switzerland.

#### 4.2.2 Flux Calibration

Observations made at Bern were recorded on tape in digital form. At each observing frequency, the microwave burst flux was recorded as a percentage of the quiet-Sun flux. Quiet-Sun flux measurements were made between bursts, and were calibrated in the following way. The amplitude of the quiet-Sun signal at each observing frequency was measured automatically, three times each day, by pointing the antenna away from the Sun. Absolute quiet-Sun fluxes were obtained at 2.8 GHz from Ottawa; at 1.0, 2.0, 3.75, and 9.4 GHz from Toyokawa Observatory, Japan; at 1.47 and 9.5 GHz from Heinrich-Hertz Institute, Berlin; and at 17 GHz from Nobeyama Observatory, Japan. These values were used to construct a spectrum of the quiet-Sun flux in the range from 1 to 17 GHz for each observing day. At 35 GHz, the quiet-Sun flux density was assumed to be 2400 SFU. Interpolation of this spectrum was used to obtain absolute quiet-Sun fluxes at the observing frequencies of the

Bern Observatory, which were used to compute absolute burst fluxes from the original relative values. The accuracy of the absolute fluxes so derived is estimated at  $\pm 5\%$ .

**Page Intentionally Left Blank**

## Chapter V

### THE TEST OF THE MODEL

#### 5.1 Flare Selection

Between 1980 February and 1981 December, 61 flares exceeding 500 SFU were observed at Bern. Of these flares, 26 also were observed with the HXRBS on SMM. For each of these flares, the plot of the hard X-ray counting rate, summed over Channels 2 through 15 was examined for statistically significant impulsive increases by at least a factor of 2 in 30 s or less. Channel 1 was excluded because its width and calibration are not well known, as mentioned in Section 4.1.4. The threshold of a factor of 2 was chosen because in some cases the impulsive rise was superposed on a clearly distinguishable gradual component, which was to be subtracted. In 23 of the events, such impulsive rises were found. These 23 bursts are listed in Table 1, with the locations on the solar disk of associated H $\alpha$  emission. The impulsive rises analyzed in the present work occurred during the flares on this list.

Of the flares listed in Table 1, 13 have been investigated previously by Wiehl et al. (1983). Most of the impulsive rises considered here are different from the ones studied by Wiehl et al., however, because of the different selection criteria.

TABLE 1  
Times and Positions of Impulsive Rises

Event Number	$t_{\text{peak}}$ (UT)	$H_{\alpha}$ Position
1	1980 Mar 29 0918:10	N 27 E 38
2	Mar 29 0955:07.1	N 07 W 10
3	Jun 4 0654:19.6	S 14 E 59
4*	Jun 29 1041:36	S 27 W 90
5	Jul 1 1626:56.7	S 12 W 38
6	Oct 9 1123:59.2	S 10 E 54
7	Nov 6 0650:52	N 09 E 08
8	Nov 8 1449:47	S 09 E 37
9	Nov 8 1450:26	S 09 E 37
10	Nov 8 1452:18.5	S 09 E 37
11*	Nov 18 0718:09	S 10 W 90
12	Dec 17 0845:37.7	N 10 E 03
13	1981 Mar 23 0655:51	N 10 W 54
14	Apr 10 1644:53	N 09 W 37
15	Apr 15 0643:09.6	N 20 W 65
16	Apr 18 1049:28.5	Unknown
17	Apr 26 1115:32	N 12 W 74
18	May 4 0838:03.8	N 16 E 19
19	Jul 19 0533:31.5	S 29 W 56
20	Jul 20 1311:33	S 26 W 56
21	Jul 26 1350:00	S 15 E 27
22	Aug 10 0658:50.9	S 13 W 15
23*	Dec 7 1451:03	S 06 E 90

N. B. Events labeled with an asterisk (\*) were not included in the statistical analysis because they occurred on the limb.

## 5.2 Selection of a Homogeneous Sample of Impulsive Rises

During most of the flares, more than one impulsive rise occurred that satisfied the above criteria. To discriminate against superpositions of impulsive features that might originate in different locations on the Sun, only the first such rise in each flare was chosen. This set includes impulsive rises to a more-or-less constant "plateau" of emission as well as "spike" bursts that fell in roughly the same time as they rose. Such plateaus were not included in the similar analysis of Crannell *et al.* (1978). No systematic differences between the properties of the plateaus and those of the spikes are found in the results of this work.

To test the proposed model, two conditions must hold with respect to each impulsive rise in addition to the specified selection criteria. First, the optically-thick portion of the microwave spectrum must be observed. Secondly, the entire source area must be observed. If part of the source were occulted by the solar limb, the derived value of  $L$  would be too low. Because Events 4, 11, and 23 were associated with H $\alpha$  emission at the limb, and may therefore have occurred in partially occulted arches, they were excluded from the correlation analysis. The rises occurring in these limb events can be used as a consistency check, however, as is shown after the statistical analysis of a properly homogeneous set of events is complete. The remaining 20 rises were analyzed as a homogeneous sample. The 3 rises which were excluded from this group are distinguished in Table 1 by asterisks.

### 5.3 Observed and Derived Parameters for Each Rise

The hard X-ray time history, summed over Channels 2 through 15, was inspected to determine  $t_{\text{peak}}$ , the time of peak counting rate. Figure 5-1, including the time history for Event 7, serves as an example. In the cases of plateaus,  $t_{\text{peak}}$  was taken to be the time at which the counting rate stopped rising, excluding small fluctuations at a level consistent with stochastic fluctuations in the counting rate. An example of a plateau is shown in Figure 5-2. Three spikes such as the rise in Event 5, shown in Figure 5-3, exhibited significant structure near the peak. In such a case, if the counting rate dropped by as much as 10%, and afterward resumed rising,  $t_{\text{peak}}$  was taken to be at the peak prior to the drop. From the standpoint of the model, this behavior could be interpreted as the result of heating at a point not precisely at the apex of the arch, as might occur in an assymetrical arch (cf. Spicer 1976). It is also possible that these cases are examples of superposed impulsive features, despite efforts to exclude them. The values of  $t_{\text{peak}}$  are listed in Table 1.

The hard X-ray time history was inspected to measure the excess counting rate above background,  $I_{\text{peak}}$ , at  $t_{\text{peak}}$ . The time at which an excess counting rate of  $I_{\text{peak}}/2$  above background was attained,  $t_{1/2}$ , was determined as well. For cases in which the impulsive rise is superposed on a gradual component, as in Figure 5-3, the gradual flare emission was treated as background.

The quantity  $t_r \equiv 2 (t_{\text{peak}} - t_{1/2})$  was used as a measure of the observed rise time. Because small statistical fluctuations in the counting rate can introduce large uncertainties in the start time of the

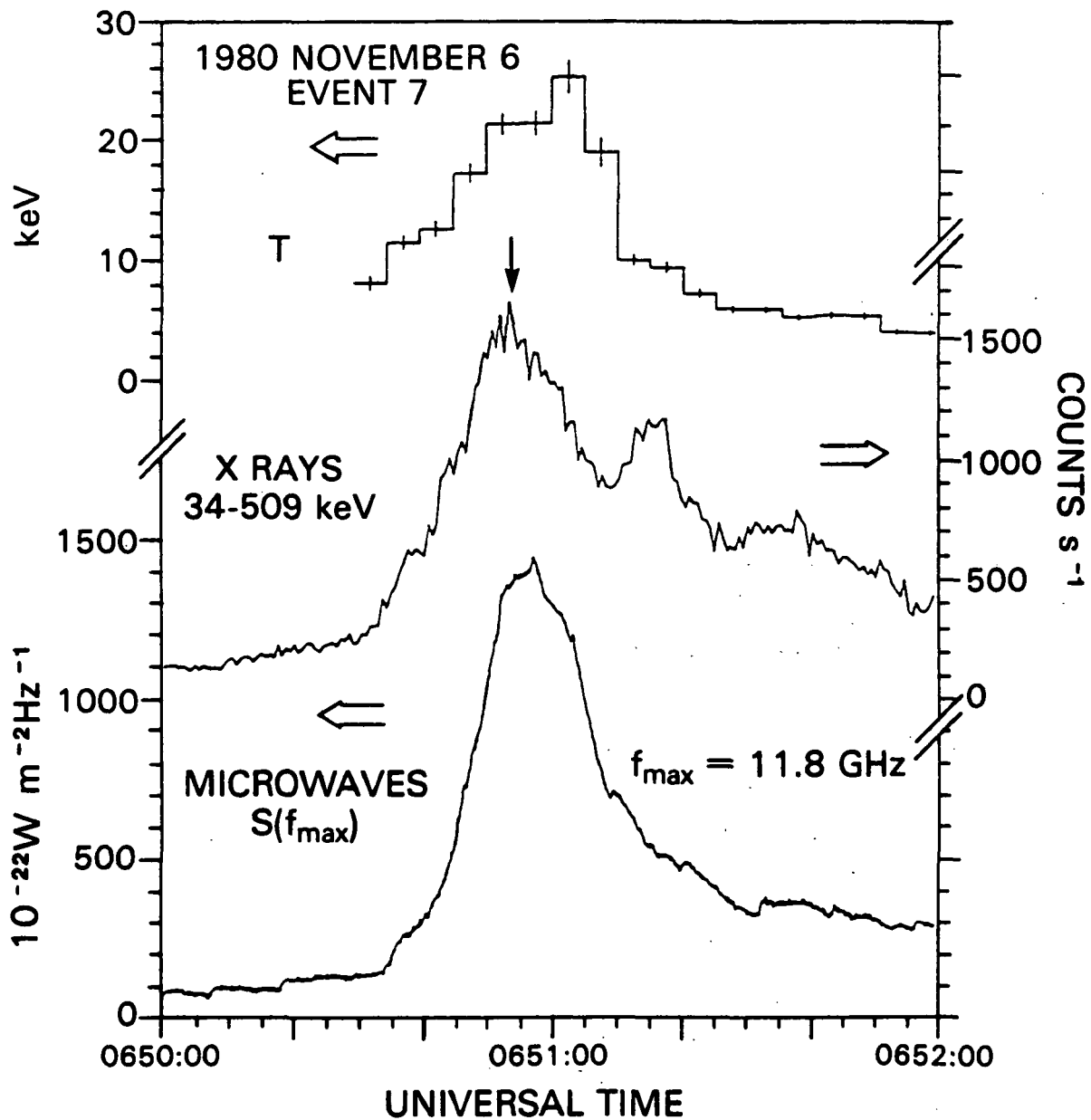


Figure 5-1. Time histories of best-fit temperature, hard X-ray counting rate, and microwave flux density for Event 7. The vertical arrow indicates  $t_{\text{peak}}$ .

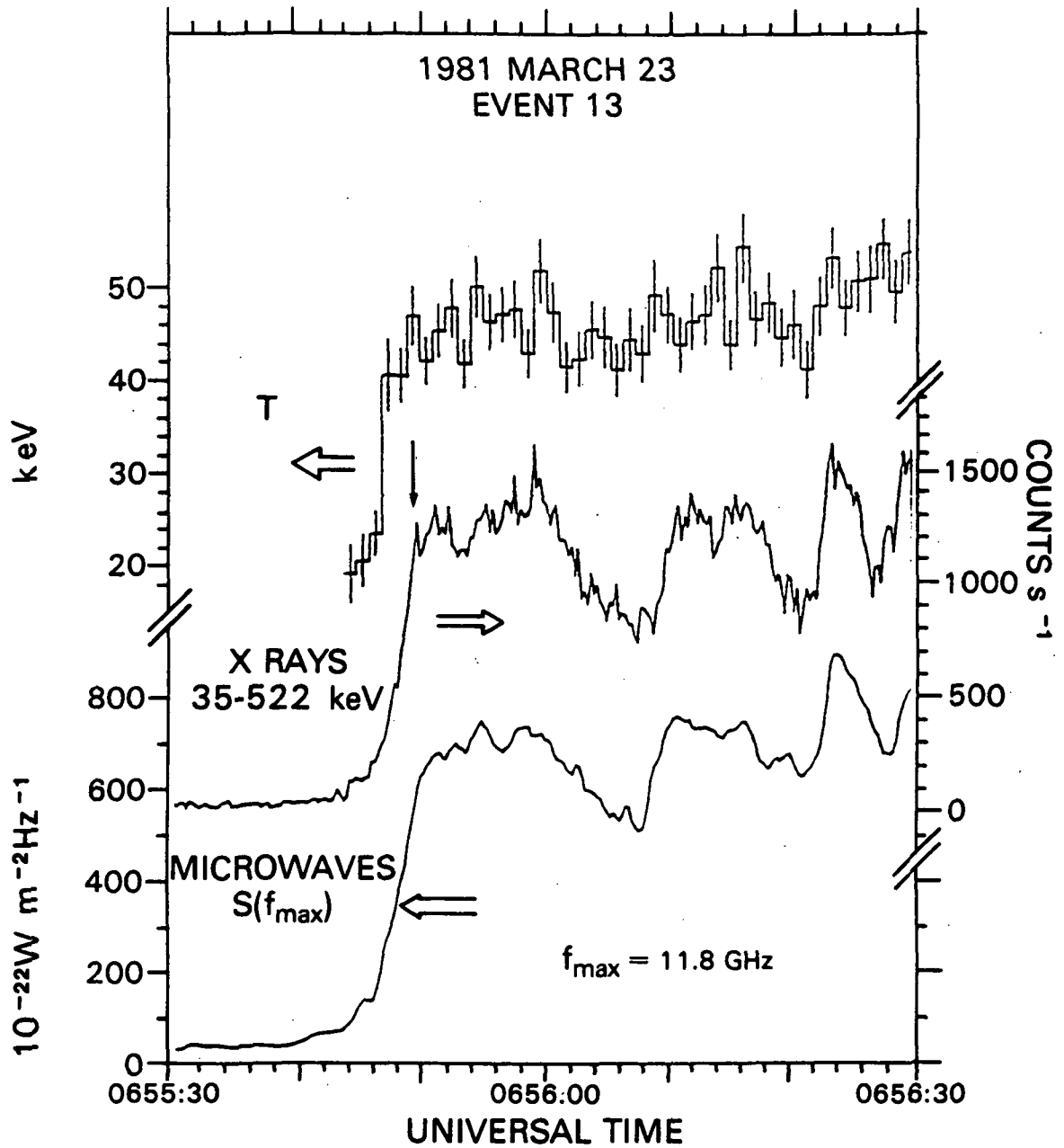


Figure 5-2. Time histories of best-fit temperature, hard X-ray counting rate, and microwave flux density for Event 13. The vertical arrow indicates  $t_{\text{peak}}$ .

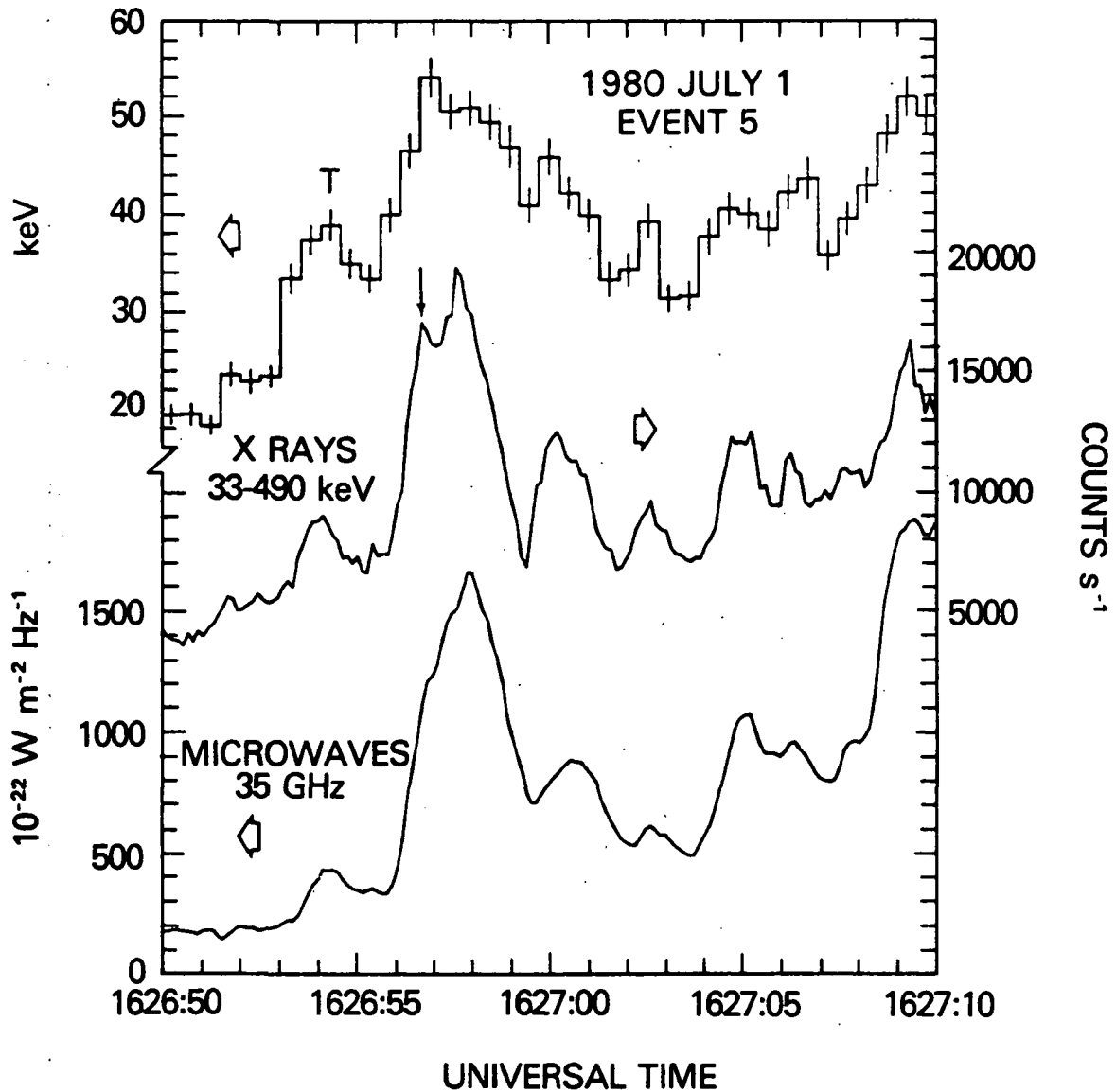


Figure 5-3. Time histories of best-fit temperature, hard X-ray counting rate, and microwave flux density for Event 5. The vertical arrow indicates  $t_{\text{peak}}$ .

rise,  $t_r$  is a more precise measure of the rise time than  $t_{\text{peak}} - t_{\text{start}}$ . The values of  $t_r$  are listed in Table 2.

The microwave spectrum associated with each rise was constructed from observations at  $t_{\text{peak}}$ . Gradual microwave emission, analogous to the gradual hard X-ray emission, was similarly treated as background. The resulting spectrum was examined to determine  $S_2$ ,  $f_2$ , and  $f_{\text{max}}$ . Two example spectra are presented in Figure 5-4.

For all of the flares except Events 8, 10, 20, and 21,  $f_2$  and  $S_2$  could be determined from the Bern observations. In the case of Event 20, the optically-thick part of the spectrum was not observed at Bern. In the absence of other data, this event would have been excluded. A time history at 2.8 GHz obtained at Ottawa was available, however, and this made it possible to determine  $S_2$  at  $f_2 = 2.8$  GHz. The spectrum of the rise in Event 8 was too flat for determination of the parameters. The spectrum of Event 10 had two peaks, and the optically-thick portion of the peak at low frequency was not observed. The optically-thick part of the spectrum of Event 21 was not observed at all. Consequently, calculations of the derived parameters could not be done for Events 8, 10, and 21, and they were not included in the statistical analysis.

Determinations of  $f_{\text{max}}$  could be made for most of the remaining 17 rises of the homogeneous sample. Only lower bounds on  $f_{\text{max}}$  could be found for Events 5, 11, 19, and 23, because  $f_{\text{max}}$  was greater than or equal to the highest frequency of observation, 35 GHz. In the case of Event 20, it was again necessary to use the Ottawa data at 2.8 GHz. The estimate  $f_{\text{max}} \approx 5$  GHz was adopted.

Hard X-ray spectra were determined for each of the rises by means

TABLE 2

Observed and Derived Parameters at  $t_{\text{peak}}$ 

Rise	$S_2$	$f_2$	$f_{\text{max}}$	$T_e$	$\mu$	$t_r$	$\tau_0$	$L_0$	$n_0$	$v_{T0}$	$U_0$	B	$w_B$	$\beta_0$
SFU	$10^9$	$10^9$	$10^9$	$10^8$	$10^{45}$	s	s	$10^9$	$10^9$	erg	$10^{27}$	G	erg	
	Hz	Hz	Hz	K	$\text{cm}^{-3}$			cm	$\text{cm}^{-3}$	$\text{cm}^{-3}$	erg		$\text{cm}^{-3}$	
1	510	10.4	11.8	5.2	1.2	3.0	3.9	0.81	1.5	160	87	150	920	0.18
2	210	10.4	11.8	4.9	0.85	5.2	2.7	0.54	2.3	240	37	160	1000	0.23
3	320	8.4	11.8	3.9	8.5	7.0	5.1	0.91	3.3	280	210	170	1200	0.23
4*	31	8.4	11.8	3.2	0.29	3.6	1.9	0.31	3.1	210	6.4	230	2100	0.10
5	460	19.6	$\geq 35.0$	6.4	1.0	0.9	1.6	0.37	4.5	600	30	$\geq 420$	$\geq 6900$	$\leq 0.087$
6	100	5.2	8.4	2.7	0.98	5.2	6.8	1.0	0.99	55	56	180	1300	0.041
7	910	8.4	11.8	2.4	0.56	20	14	2.0	0.27	14	100	300	3700	0.004
9	33	8.4	10	1.0	0.77	7.0	6.2	0.57	2.0	45	8.3	460	8500	0.005
11*	44	19.6	$\geq 35.0$	2.9	0.16	2.2	1.1	0.17	5.7	350	1.7	$\geq 820$	$\geq 27000$	$\leq 0.013$
12	280	8.4	11.8	4.8	0.17	3.2	3.9	0.78	0.60	60	28	180	1300	0.046
13	260	8.4	11.8	4.9	0.33	6.0	3.7	0.74	0.90	92	37	170	1200	0.079
14	120	5.2	8.4	3.6	0.098	10	5.5	0.95	0.34	26	22	160	1000	0.025
15	14	5.2	8.4	1.9	0.27	3.8	3.6	0.45	1.7	67	6.1	250	2500	0.027
16	55	8.4	11.8	2.2	0.27	5.0	3.8	0.51	1.4	67	8.7	320	4100	0.016
17	75	3.2	5.2	2.7	0.50	11	9.5	1.4	0.42	24	66	110	510	0.046
18	17	5.2	10	2.2	0.68	1.8	3.4	0.45	2.7	120	12	250	2500	0.049
19	1400	19.6	$\geq 35.0$	3.5	3.3	12	5.2	0.87	2.2	160	110	$\geq 660$	$\geq 18000$	$\leq 0.009$
20	170	2.8	5	2.2	0.24	22	20	2.7	0.11	5	99	140	730	0.007
22	200	8.4	11.8	3.1	1.2	2.6	5.1	0.81	1.5	99	52	230	2100	0.047
23*	240	19.6	$\geq 35.0$	5.8	0.74	10	1.3	0.28	5.8	710	15	$\geq 450$	$\geq 8100$	$\leq 0.088$

\* Limb event. Derived parameters may not characterize whole source, if source is occulted.

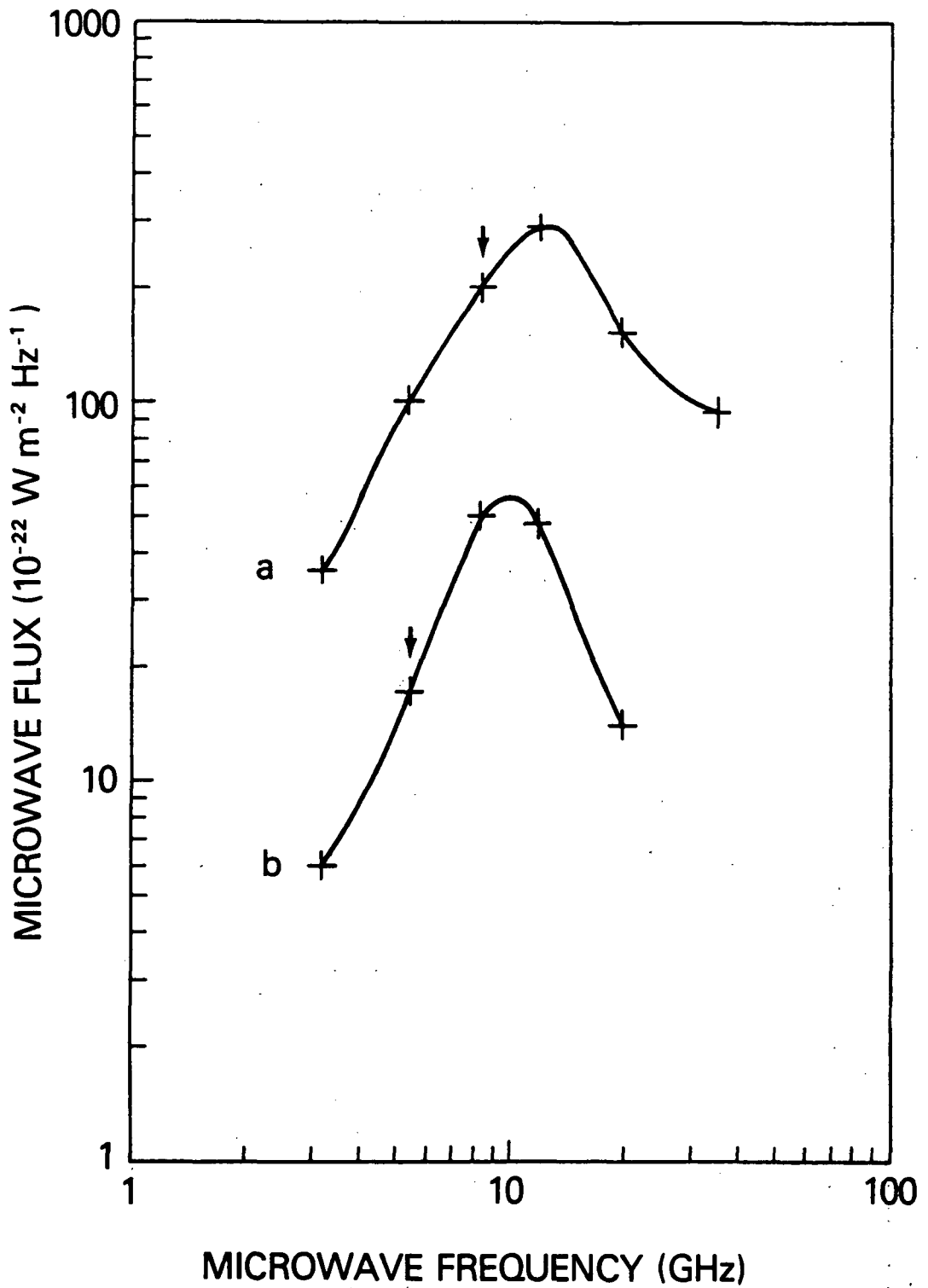


Figure 5-4. Microwave spectra at  $t_{\text{peak}}$  for Events 22 (a) and 18 (b). For each spectrum,  $f_2$  is indicated by the vertical arrow.

of the spectral analysis procedure described in Section 4.1.4. For each rise, the best-fit thermal bremsstrahlung function was found, using data accumulated for a time interval centered on  $t_{\text{peak}}$  of sufficient duration to obtain adequate counting statistics.

The derived parameters defined in Sections 3.3 and 3.4 could be calculated for the 20 events in which  $f_2$  and  $S_2$  were known; that is, for all rises except Events 8, 10, and 21. In Table 2, the observed parameters at  $t_{\text{peak}}$  and the derived parameters for the 20 rises are presented.

#### 5.4 Correlation Analysis of Observed and Predicted Rise Times

The predictions of the model were tested as described in Section 3.3. A linear correlation analysis was performed on the parameters  $t_r$  and  $\tau_0$  derived for each of the 17 impulsive rises that were not associated with H $\alpha$  emission at the limb. The three limb rises were excluded, for reasons explained in Section 5.3; they are considered separately in Section 5.6.2.

The relationship between  $t_r$  and  $\tau_0$  is presented graphically in Figure 5-5, and is  $t_r = a (\tau_0)^b$ , with some scatter. The parameters  $a$  and  $b$  are determined for the 17 disk events by means of an unweighted, linear least-squares fitting procedure. The values of  $a$  and  $b$  that are most representative of the relationship are found by minimizing the root-mean-square (rms) perpendicular distance of the 17 points from a straight line in the  $(\log t_r, \log \tau_0)$  plane. This method was used to determine  $a$  and  $b$ . Two additional linear least-squares fits were carried out, one with respect to the  $t_r$  coordinate and one with

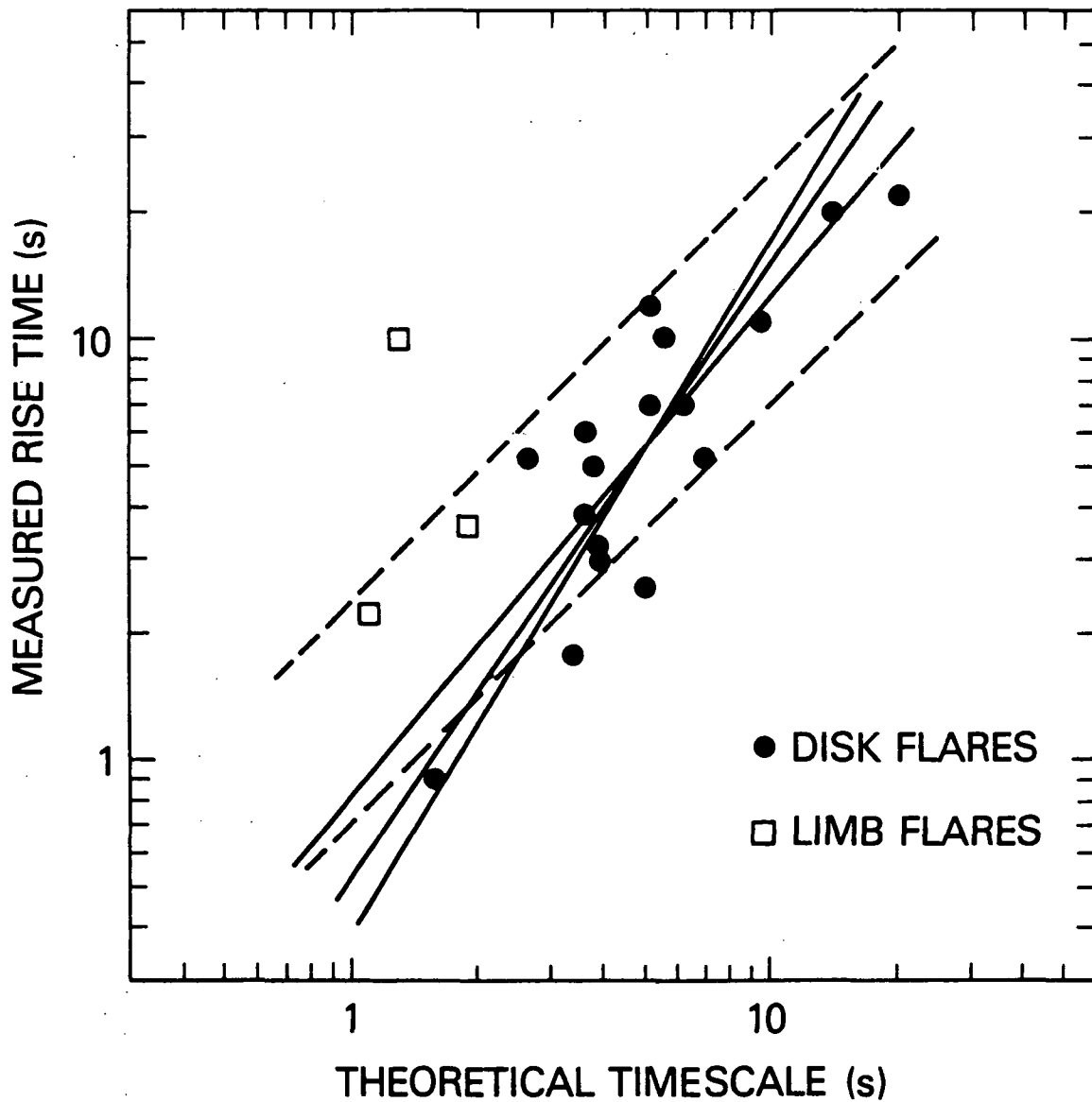


Figure 5-5. Correlation diagram of  $t_r$  and  $\tau_0$ . Solid lines indicate best fits found by linear least-squares fitting. Dashed lines are boundaries of the expected positions of disk points, if the sources are arches from 2 to 4 times as long as they are thick.

respect to the  $\tau_0$  coordinate (Bevington 1969). The best fits derived by all three methods are indicated in Figure 5-5 with solid lines. The solid line with a slope intermediate between the other two represents the best fit derived by minimizing the rms perpendicular distance. The resulting parameters are:  $a = 0.51$ ,  $b = 1.5$ , with a correlation coefficient  $r = 0.84$ ; i.e.  $t_r \approx 0.51 \tau_0^{1.5}$ . Calculations of the one-sigma uncertainties in  $a$  and  $b$  by propagation of errors lead to the ranges  $0.28 < a < 1.1$  and  $0.98 < b < 2.0$ . Thus the correlation is indeed approximately a linear relationship, as predicted in Section 3.3, and is consistent with equality, within the uncertainties. This agreement between the predicted timescale and the measured rise time provides strong support for the model.

The probability  $P_c(r, N)$  that the  $(t_r, \tau_0)$  parameter pairs come from an uncorrelated parent population is a quantitative measure of the statistical significance of the correlation,  $N$  being the number of points (Bevington 1969). For these 17 disk events,  $P_c(r, N) = 2.4 \times 10^{-5}$ , hence an accidental relationship with a correlation coefficient as large as 0.84 is highly unlikely. One would have to analyze 710,000 bursts and construct 42,000 plots like Figure 5-5 to obtain a correlation this good by accident.

The observed scatter in the correlation is about a factor of 3, in good agreement with the factor of 2.5 estimated in Section 3.3, considering the uncertainties noted. The area between the dashed lines represents the predicted range determined from the inequality (3.11) for arches with  $2 < \eta < 4$ , somewhat less than the typical value of 5. This range should not be regarded as precise, however, because of possible contributions from asymmetrical arches and temperature gradients, and

because of uncertainties in the measurements, described next.

### 5.5 Uncertainties in the Measurements

Uncertainties in the measurements of  $f_2$ ,  $S_2$ , and  $T_e$  contribute to uncertainty in  $\tau_0$ . The choice of  $f_2$  is not crucial to a precise calculation of  $\tau_0$ , however. Only the value of  $S^{1/2}/f$  in the optically-thick part of the spectrum is required, with the qualification in the case of an inhomogeneous source that the frequency be as near  $f_{\max}$  as possible (see Section 3.3). Determination of  $S_2$  and  $f_2$  as described in Section 3.3 should not introduce uncertainties of more than 20% in the ratio  $S^{1/2}/f$ , including the uncertainties in  $S_2$  alone. The uncertainty in  $T_e$  is also about 20%. Thermal fits were acceptable representations of the hard X-ray spectra from about 30 to 300 keV in most cases; in the remainder, the fit was acceptable at low energies but some excess was present at 100 keV or above. These excesses can be explained by departures from uniform temperature in the source, of the same magnitude as the uncertainty in  $T_e$ . The uncertainties in measurements of  $f_2$ ,  $S_2$ , and  $T_e$  are therefore estimated to contribute much less to the scatter than the intrinsic uncertainties estimated in Section 3.3.

### 5.6 Consistency Checks

#### 5.6.1 Search for More Fundamental Correlations

Consider first the possibility that the correlation between  $t_x$

and  $\tau_0$  is not the fundamental relationship revealed by Figure 5-5, but rather is the result of a relationship of  $t_r$  with some other parameter. The possible parameters are  $f_2$ ,  $S_2$ , and  $T_e$ , and combinations of these parameters such as the derived length scale,  $L_0$  ( $c_s$  is proportional to  $T_e^{1/2}$ , so we need not consider it separately).

Correlation diagrams such as Figure 5-5 were constructed for the four possibilities, and are shown in Figures 5-6 through 5-9. The correlation diagrams for  $f_2$ ,  $S_2$ , and  $T_e$  exhibit large amounts of scatter, and none has a correlation coefficient  $r$  greater than 0.40. Because this corresponds to a  $P_c(r,N)$  of 0.1, it is clear that none of these parameters is the sole source of the relation of  $t_r$  and  $\tau_0$ .

The relationship between  $L_0$  and  $t_r$  was also considered. This possibility was suggested by a similar relationship found by Crannell *et al.* (1978) in a study of spike bursts (see Section 5.6.3). In the case of  $L_0$  and  $t_r$ , derived herein,  $L_0$  is well correlated with  $t_r$  ( $r = 0.81$ ,  $P_c(r,N) = 8.1 \times 10^{-5}$ ). This result is to be expected because the values of  $c_s$  are all of the same order, in the range from 910 to 2300 km s<sup>-1</sup>. The best-fit relationship is  $L_0 \approx 0.30 \times 10^9 t_r^{0.57}$ , and the correlation exhibits somewhat more scatter than that of  $t_r$  with  $\tau_0$ . Thus, dividing  $L_0$  by  $c_s$  produces a slightly better correlation, with  $r = 0.84$ , as opposed to  $r = 0.81$  if  $L_0$  alone is compared with  $t_r$ . The difference between these values of  $r$  is not a compelling argument in favor of the model, but is consistent with the expectation that including the influence of  $c_s$  removes some of the variance in the observed relationship between  $t_r$  and  $L_0$ . Physical considerations, the existence of a model that predicts the observed relationship between  $t_r$  and  $\tau_0 \equiv L_0/c_s$ , favor the interpretation

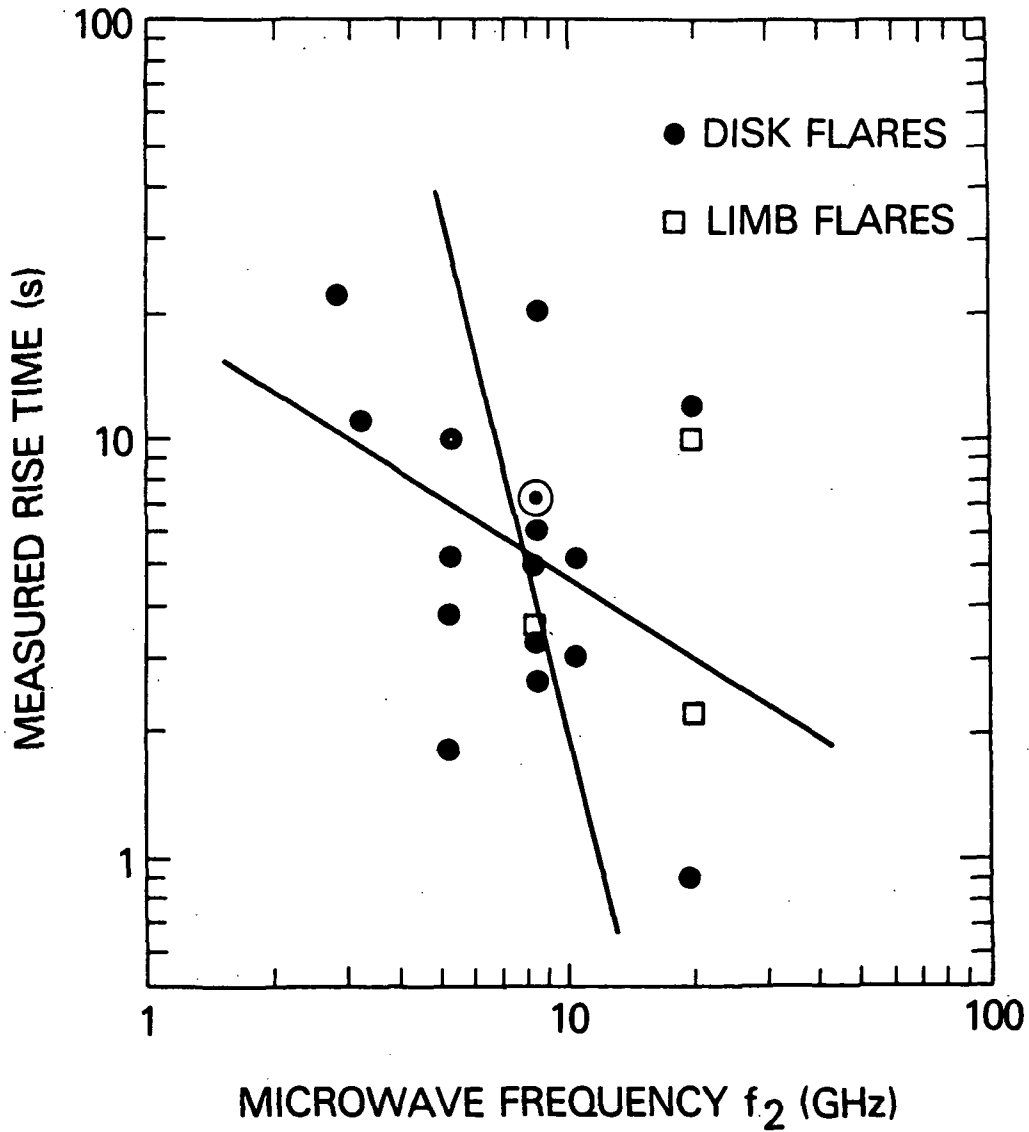


Figure 5-6. Plot of  $t_r$  vs.  $f_2$ . (Circled point indicates 2 overlapping points.)

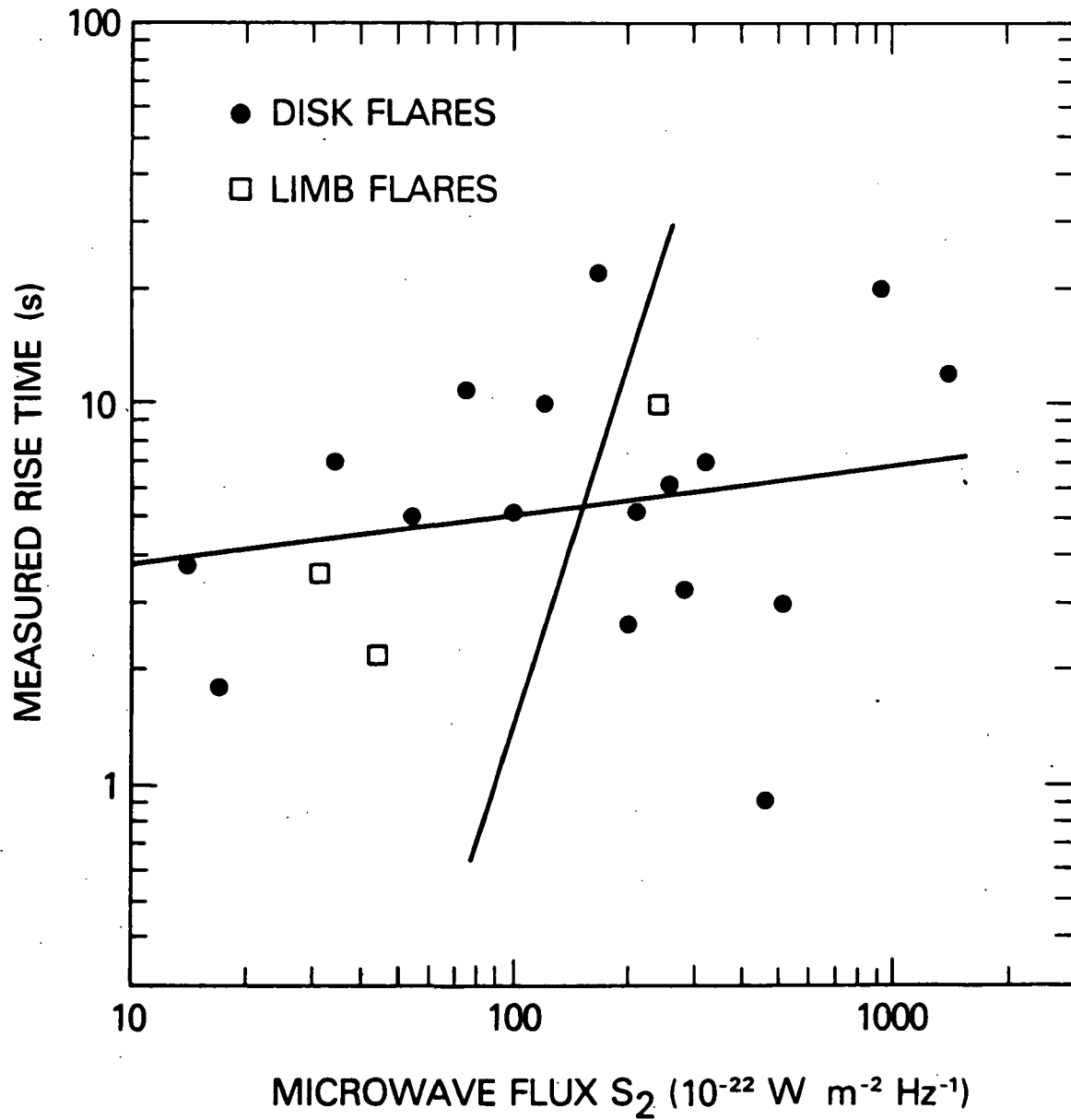


Figure 5-7. Plot of  $t_r$  vs.  $S_2$ .

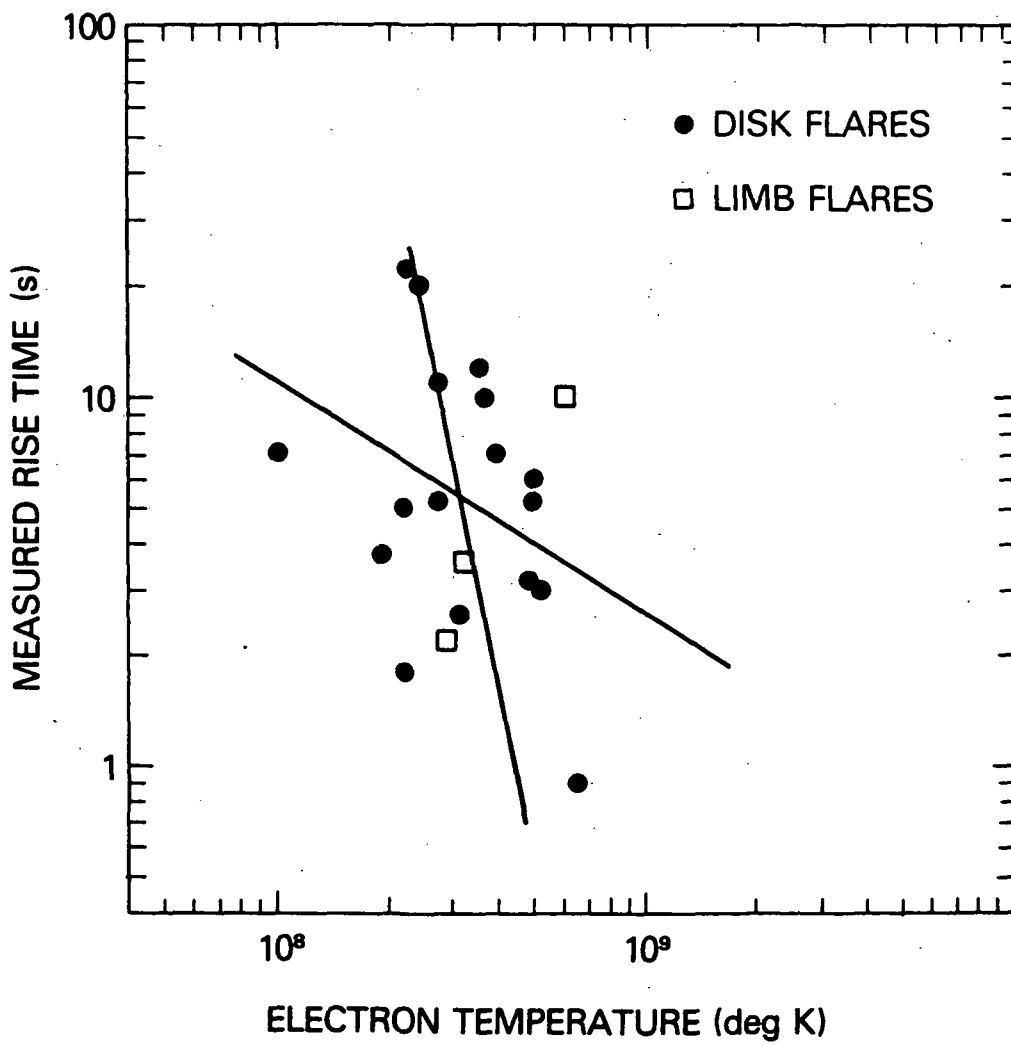


Figure 5-8. Plot of  $t_r$  vs.  $T_e$ .

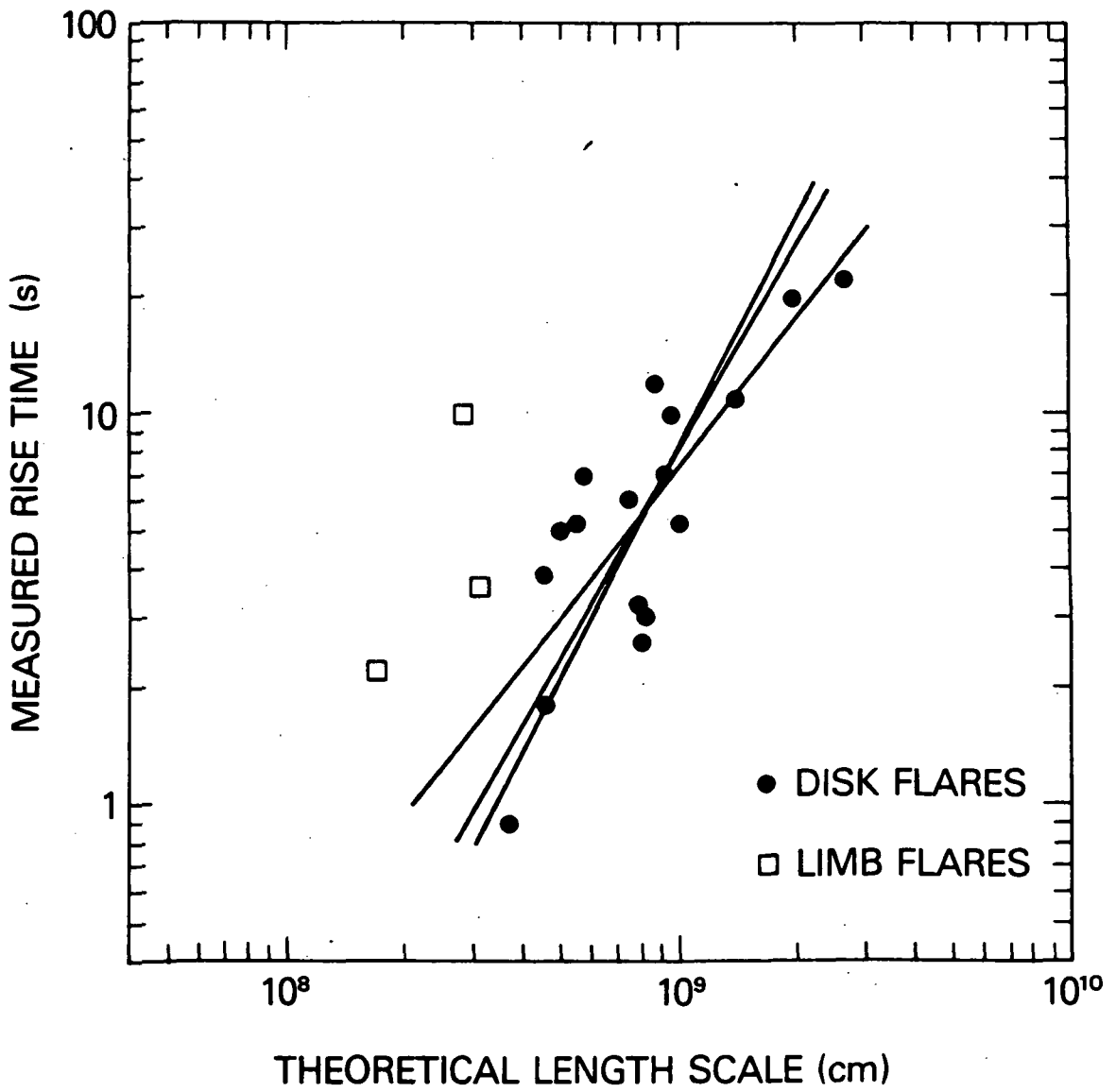


Figure 5-9. Plot of  $t_r$  vs.  $L_0$ .

inferred from the model.

### 5.6.2 Limb Rise Analysis

Another check of the model is provided by the three limb rises that were observed. Partial occultation of the source by the solar limb in such cases might reduce the observed  $L_0$ , and therefore  $\tau_0$ . Precise information about the source location with respect to the limb is not available. The area of a source precisely at the limb would not be occulted by a large fraction, and the corresponding point in Figure 5-5 would be near the least squares fit of the disk sources. A source beyond the limb would be occulted, and the corresponding point would appear farther to the left of the least squares fit in Figure 5-5.

Data on the three limb rises were reduced as described in Section 5.3. The points corresponding to the limb rises in Figure 5-5 are all to the left of the best fit of the homogeneous group. The point for Event 23 appears farthest to the left ( $t_r = 10$  s,  $\tau_0 = 2.8$  s), suggesting that occultation by the solar limb reduced its apparent area by a large fraction, approximately 90%. All three of these cases are consistent with the prediction of the model and provide additional support for it.

It is also noteworthy that the values of  $L_0$  derived for the limb rises are the three lowest values in Table 2. This is also consistent with the interpretation that they are partially occulted. It is remarkable that this interpretation can be made from observations with no spatial resolution.

### 5.6.3 Comparison with Results of Crannell et al. (1978)

The correlation of  $L_0$  and  $t_r$  presented here can be compared to a similar result of the spike burst study by Crannell et al. (1978). A correlation was found in that study between  $D$ , the derived source diameter in units of  $10^9$  cm at the time of peak microwave emission, and  $t_x$ , the burst duration in hard X rays (the rise time plus the fall time). Because the rise and fall times of the spike bursts are approximately equal,  $t_x$  is approximately twice the rise time,  $t_{xr}$ . The best-fit relationship  $t_x \approx 3.8 D^{0.68}$  was found ( $r = 0.80$ ,  $P_c = 2 \times 10^{-4}$ ). To investigate whether or not this is consistent with the prediction of the model, the parameters  $S_2$ ,  $f_2$ ,  $T$ , and the actual  $t_{xr}$  measured by Crannell et al. for 16 of the spike bursts, were used to calculate the corresponding  $L_0$  and  $t_r$ . For comparison, the length scales,  $D$  and  $L_0$ , for both sets of measurements, are re-expressed in units of  $10^9$  cm, and designated  $L_9$ . The rise time used herein is  $t_r \approx 4t_{xr}/3$ . The spike bursts exhibit the relationship  $t_r = a L_9^b \approx 13 L_9^{0.57}$ . The one-sigma uncertainties in fitting parameters give  $9.7 < a < 25$  and  $0.40 < b < 1.0$ . For comparison, the relationship shown in Section 5.6.1 is  $t_r \approx 8.3 L_9^{1.7}$ . The one-sigma uncertainties in this relationship are  $6.3 < a < 12$  and  $1.0 < b < 2.4$ . Both of these relationships are consistent to within one sigma with the prediction of the model,  $b \approx 1$ , with  $a \approx 10$ . This value of  $a$  corresponds to a mean ion-sound velocity of  $\approx 1000 \text{ km s}^{-1}$ , and electron temperature of  $\approx 10^8 \text{ K}$  for the disk events. A correlation similar to that shown in Figure 5-5 was also present in the spike burst study:  $t_r \approx 5.4 \tau_0^{0.49}$ , with a correlation coefficient

$r = 0.75$ . The one-sigma uncertainties in this relationship are  $2.3 < a < 6.8$  and  $0.33 < b < 1.0$ . Thus, this result, too, is consistent with a linear relationship between  $t_r$  and  $\tau_0$ , as predicted by the model.

Crannell et al. interpreted the correlation of burst duration with derived diameter as support for the possibility that a compressional disturbance could traverse the source region, and cause the required heating on timescales consistent with the time structures of the observed emissions (see the discussion of adiabatic compression in Section 2.3.6). Velocities in the range from 200 to 700 km s<sup>-1</sup> were inferred from the relationship between diameter and duration, and attributed to such compressional disturbances. This result, however, was never related to a specific travel time of the disturbance.

Observational bias is present in both the spike burst study and the present work. The flares listed in Table 1 were selected because of their large peak microwave fluxes, and include relatively more large bursts than the sample of spike bursts, which were selected on the basis of the X-ray time histories. Thus the results presented here may be biased in favor of the properties of large bursts. As shown by Figure 5-7, there is no significant correlation of  $S_2$  with  $t_r$ , however, and the average value of  $L_0$  in the present study differs from that of the spike burst events by only about 10%. Thus the excess of large bursts in the present study does not appear to contribute to systematic differences from the spike burst results. A factor that may contribute to a systematic difference in the exponents of  $\tau_0$  is the lower sampling rate of the OSO-5 X-ray data which were used in the spike burst study. Spectral data were measured by the spectrometer on OSO-5

for a 0.19 s interval, every 1.9 s; HXRBS accumulates spectral data for each 0.128 s, continuously. Undersampling of the OSO-5 data would introduce a systematic overestimate of  $t_r$  for X-ray variations on timescales of the order of the sampling interval or less, or disguise some multiply-impulsive events as single spikes. Both of these effects would contribute to the relatively low exponent of  $\tau_0$  derived from the OSO-5 measurements. Future verifications of these correlations should make use of data with the best possible time resolution and a sample of bursts that is unbiased with respect to intensity.

In summary, the results of this work and the spike burst analysis of Crannell et al. together provide strong support for the model.

### 5.7 Other Derived Parameters

The derived lengths, densities, and values of  $\beta$  are all consistent with the assumptions of the model. The length scales of the rises observed on the solar disk vary from 3700 km to 27000 km, which is a representative range of lengths for coronal arches. The densities are appropriate to arches in the corona, ranging from 0.11 to  $4.5 \times 10^9 \text{ cm}^{-3}$ . The values of  $\beta$  are less than unity, showing that the neglect of lateral expansion in the heated arch is justified. The low  $\beta$ 's also indicate that the energy requirements are not too great to be supplied by annihilation of a fraction of the derived magnetic field within the volume. The total energy inferred in the plasma,  $U_0$ , ranges from  $\sim 10^{27}$  to  $\sim 10^{29}$  erg. This is quite modest in comparison with the requirements of nonthermal models, which range from  $\sim 10^{28}$  to  $\sim 10^{32}$  erg (Brown and Melrose 1977).

**Page Intentionally Left Blank**

## Chapter VI

### CONCLUSIONS AND SUGGESTIONS FOR FUTURE INVESTIGATIONS

In this dissertation, new observational support is presented for the thermal flare model which was proposed by Brown, Melrose, and Spicer (1979) and Smith and Lilliequist (1979). The observed relationship between the burst dynamics and the parameters of the microwave and hard X-ray spectra has not been predicted by any other model presented in the literature. The high degree of statistical significance of the correlation presented in Section 5.4 is clearly indicative of some fundamental underlying physical process that demands to be explained, whatever model is chosen for these impulsive bursts.

These results are particularly difficult to explain in the context of either of the major competing nonthermal models, the thick-target model and the trap-plus-precipitation model. In the thermal conduction-front model, the calculation of predicted rise time,  $\tau_0$ , from spectral parameters depends upon the thermal interpretation of the hard X-ray and microwave spectra, and the characteristic expansion rate of a confined, thermal source. For the thick-target model to be successful, it also would be required to explain the specific relationships between observed rise time and spectral parameters of the hard X-ray and microwave emissions. In the thick-target model, however, the rise time of a burst is determined by the dynamics of an unknown

acceleration mechanism. The travel time of freely-streaming nonthermal electrons from the apex to the footpoint of an arch in the thick-target model is of order 0.1 s, too short to be of relevance for the rise time of a burst. The observed correlation between rise time and spectral parameters would imply a specific relationship between rise time, source size, and nonthermal electron distribution. The trap-plus-precipitation model also would require a specific relationship, resulting from the competition of the acceleration timescale, the escape timescale of the precipitating component of the electron distribution, and the effects of trapping or re-acceleration. Neither of these models have been found to present any a priori physical reasons for the observationed correlations.

In the thermal conduction-front model, the confinement mechanism leads in a straightforward way to the observed relationship of the parameters. That some correlation exists between the observed and derived rise times is, perhaps, not surprising, but the fact that the correlation is consistent with equality strongly suggests that the model has physical significance. These results also suggest that the model proposed by Brown, Craig, and Karpen (1980), which invokes many separate thermal sources with very short lifetimes, is not required to explain the observations.

Another interesting aspect of this model that has not been investigated here is the implication of the existence of the thermoelectric field in the conduction front for proton and ion acceleration. While this field has the effect of confining electrons within the thermal source, its direction is such as to accelerate positively-charged particles out of the source. The potential,

$E = 2kT_e/e$ , could accelerate protons to energies of order 50 keV, and ions of charge  $Z$  could reach proportionally higher energies. The possibility that the thermoelectric potential is actually higher than the value derived by Smith and Brown (1980) is also relevant to ion acceleration.

The results of this work are amenable to further testing by means of statistical analysis of additional rises, and by means of imaging observations. The method used here to derive source sizes has never been tested by direct comparison with interferometric microwave observations or hard X-ray images. Additional theoretical development of the model would also be useful, in the form of improved fluid MHD simulations and particle simulations. These simulations could illuminate the detailed physics of the decline in emission, which is not considered here, and, perhaps, provide detailed explanations of the observed relationships between temperature and emission measure.

An instrument for imaging of hard X rays in the energy range from 2 to 120 keV is being considered as part of the Pinhole/Occulter Facility, which has been proposed for use with Spacelab on a future Space Shuttle mission (Tandberg-Hanssen *et al.* 1983). With its proposed angular resolution of less than 1 arc second and sub-second time resolution, this instrument could provide an important test of the predictions of the model considered herein. Concurrent observations with such an instrument and a microwave interferometer with similar temporal and spatial resolution would be ideal for testing theoretical models of the flare phenomenon.

**Page Intentionally Left Blank**

## REFERENCES

- Acton, L. W. 1964, Nature, 204, 64.
- \_\_\_\_\_ 1968, Astrophys. J., 152, 305.
- Acton, L. W., Canfield, R. C., Gunkler, T. A., Hudson, H. S., Kiplinger, A. L., and Leibacher, J. W. 1982, Astrophys. J., 263, 409.
- Akhiezer, A. I., and Berestetskii, V. B. 1965, Quantum Electrodynamics (New York: Interscience).
- Allen, C. W. 1976, Astrophysical Quantities (London: Athlone), 3rd ed.
- Antiochus, S., and Sturrock, P. A. 1978, Astrophys. J., 220, 1137.
- Arnoldy, R. L., Kane, S. R., and Winckler, J. R. 1968, Astrophys. J., 151, 711.
- Bai, T. 1977, Ph. D. Dissertation, University of Maryland, published as NASA document X-660-77-85.
- Bekefi, G. 1966, Radiation Processes in Plasmas (New York: Wiley).
- Benford, G., and Book, D. L. 1971, in Advances in Plasma Physics 4, A. Simon and W. B. Thomsen, eds. (Interscience), p. 125.
- Benz, A. O. 1977, Astrophys. J., 211, 270.
- Bevington, P. R. 1969, Data Reduction and Error Analysis for the Physical Sciences (New York: McGraw-Hill).
- Birks, J. B. 1964, The Theory and Practice of Scintillation Counting (New York: MacMillan).
- Boyd, T. J. M., and Sanderson, J. J. 1969, Plasma Dynamics, (New York: Barnes and Noble).
- Brown, J. C. 1971, Solar Phys., 18, 489.
- \_\_\_\_\_ 1973, Solar Phys., 28, 151.
- \_\_\_\_\_ 1974, in IAU Symposium No. 57, Coronal Disturbances, ed. G. Newkirk (Dordrecht: Reidel), p. 395.
- \_\_\_\_\_ 1975, in IAU Symposium No. 68, Solar Gamma, X-, and EUV Radiation, ed. S. R. Kane (Dordrecht: Reidel), p. 245.
- \_\_\_\_\_ 1976, Phil. Trans. Roy. Soc. London, 281, 473.
- Brown, J. C., Carlaw, V. A., Cromwell, D., and Kane, S. R. 1983a, Solar Phys., 88, 281.

- Brown, J. C., Craig, I. J. D., and Karpen, J. T. 1980, Solar Phys., 67, 143 (BCK).
- Brown, J. C., and Hoyng, P. 1975, Astrophys. J., 200, 734.
- Brown, J. C., MacKinnon, A. L., Zodi, A. M., and Kaufmann, P. 1983b, Astron. Astrophys., 123, 10.
- Brown, J. C., and McClymont, A. N. 1975, Solar Phys., 41, 135.
- \_\_\_\_\_ 1976, Solar Phys., 49, 329.
- Brown, J. C., and Melrose, D. B. 1977, Solar Phys., 52, 117.
- Brown, J. C., Melrose, D. B., and Spicer, D. S. 1979, Astrophys. J., 228, 592 (BMS).
- Brown, J. C., and Smith, D. F. 1980, Rep. Prog. Phys., 43, 125.
- Bumba, V. 1958, Izv. Krymsk. Astrofiz. Obs., 19, 105.
- Cheng, C.-C. 1972, Space Sci. Rev., 13, 3.
- Chubb, T. A. 1972, in Solar-Terrestrial Physics/1970: Part I, Astrophys. and Space Sci. Library, 29, E. R. Dyer, ed. (Dordrecht: Reidel), p. 99.
- Chubb, T. A., Kreplin, R. W., and Friedman, H. 1966, J. Geophys. Res., 71, 3611.
- Colgate, S. A. 1978, Astrophys. J., 221, 1068.
- Cornell, M. E., Hurford, G. J., Kiplinger, A. L., and Dennis, B. R. 1984, Astrophys. J.
- Covington, A. E. 1948, Proc. I R E, 36, 454.
- \_\_\_\_\_ 1951, J. Roy. Astron. Soc. Canada, 45, 157.
- Crannell, C. J., Frost, K. J., Mätzler, C., Ohki, K., and Saba, J. L. 1978, Astrophys. J., 223, 620.
- Datlowe, D. W. 1975, Space Sci. Instrum., 1, 389.
- \_\_\_\_\_ 1977, Nucl. Instrum. Methods, 145, 365.
- Datlowe, D. W., O'Dell, S. L., Peterson, L. E., and Elcan, M. J. 1977, Astrophys. J., 212, 561.
- de Jager, C., and de Jonge, G. 1978, Solar Phys., 58, 127.
- de Jager, C., and Kundu, M. R. 1963, Space Res., 3, 836.

Dennis, B. R. 1981, "Response of HXRBS as a Function of the Spectrum of Incident Photon Energies", NASA internal document.

\_\_\_\_\_ 1982, "Thermal Bremsstrahlung X-Ray Spectrum - Modifications for the HXIS Energy Range", NASA internal document.

Dennis, B. R., Frost, K. J., Orwig, L. E., Kiplinger, A., Dennis, H. E., Gibson, B. E., Kennard, G. S., and Tolbert, A. K. 1983, NASA Tech. Memo. 84998.

Dolan, J. F. 1972, Astrophys. Space Sci., 17, 472.

Duijveman, A., Hoyng, P., and Machado, M. E. 1982, Solar Phys., 81, 137.

Dulk, G., and Dennis, B. 1982, Astrophys. J., 260, 875.

Dulk, G. A., and Marsh, K. A. 1982, Astrophys. J., 259, 350.

Dulk, G. A., Melrose, D. B., and White, S. M. 1979, Astrophys. J., 234, 1137.

Elcan, M. J. 1978, Astrophys. J. Lett., 226, L99.

\_\_\_\_\_ 1979, Ph. D. Dissertation, U. of Calif., San Diego, UCSD-SP-79-28.

Emslie, A. G., McCaig, M. G., and Brown, J. C. 1979, Solar Phys., 63, 175.

Emslie, A. G., and Vlahos, L. 1980, Astrophys. J., 242, 359.

Enome, S., Kakinuma, T., and Tanaka, H. 1969, Solar Phys., 6, 428.

Foukal, P. 1975, Solar Phys., 43, 327.

Fowler, T. K. 1968, in Advances in Plasma Physics, Vol. 1, ed. A. Simon and W. B. Thomson (New York: Interscience), p. 201.

Frost, K. J. 1969, "The High-Energy X-Ray Detector on the Last Orbiting Solar Observatory, OSO - 8", NASA-X-682-75-159.

Frost, K. J., and Dennis, B. R. 1971, Astrophys. J., 165, 655.

Furth, H. P., Killeen, J., and Rosenbluth, M. N. 1963, Phys. Fluids, 6, 459.

Ginzburg, V. L., and Syrovatskii, S. I. 1964, The Origin of Cosmic Rays (New York: MacMillan).

\_\_\_\_\_ 1965, Ann. Rev. Astron. Astrophys., 3, 297.

- Goodman, N. B. 1976, Space Sci. Instrumentation, 2, 425.
- Groenschild, E. H. B. M., and Mewe, R. 1978, Astron. Astrophys. Suppl. Ser., 32, 283.
- Gordon, I. M. 1960, Soviet Astron. — A. J., 4, 874.
- Guidice, D. A., and Castelli, J. P. 1975, Solar Phys., 44, 155.
- Guseinov, R. E. 1963, Soviet Astron. — A. J., 7, 444.
- Hachenberg, O., and Wallis, G. 1961, Z. Astrophys., 52, 42.
- Heitler, W. 1954, The Quantum Theory of Radiation (Oxford: Oxford University Press).
- Heyvaerts, J., Priest, E. R., and Rust, D. M. 1977, Astrophys. J., 216, 123.
- Holt, S., and Ramaty, R. 1969, Solar Phys., 8, 119.
- Horton, W., and Choi, D. 1979, Phys. Rept., 49, 273.
- Hoyng, P., Brown, J. C., and van Beek, H. F. 1976, Solar Phys., 48, 197.
- Hoyng, P., Duijveman, A., Machado, M. E., Rust, D. M., Svestka, Z., Boelee, A., de Jager, C., Frost, K. J., Lafleur, H., Simnett, G. M., van Beek, H. F., and Woodgate, B. E. 1981, Astrophys. J. Lett., 246, L155.
- Hoyng, P., Knight, J. W., and Spicer, D. S. 1978, Solar Phys., 58, 139.
- Hoyng, P., Marsh, K. A., Zirin, H., and Dennis, B. R. 1983, Astrophys. J., 268, 865.
- Hudson, H. S. 1972, Solar Phys., 24, 414.
- \_\_\_\_\_ 1973, in High Energy Phenomena on the Sun, ed. R. Ramaty and R. G. Stone, NASA SP-342, p. 207.
- Kahler, S. W. 1971a, Astrophys. J., 164, 365.
- \_\_\_\_\_ 1971b, Astrophys. J., 168, 319.
- Kahler, S. W., and Kreplin, R. W. 1971, Astrophys. J., 168, 531.
- Kahler, S., Spicer, D., Uchida, Y., and Zirin, H. 1980, in Solar Flares, P. A. Sturrock, ed.
- Kane, S. R. 1974, in Coronal Disturbances, IAU Symposium No. 57, G. Newkirk, Jr., ed. (Dordrecht: Reidel), p. 105.

Kaplan, S. A., Pikel'ner, S. B., and Tsytovich, V. N. 1974, Phys. Rep. C, 15(1), 1.

Karpen, J. T. 1980, Ph. D. Dissertation, University of Maryland, College Park, published as NASA Technical Memo. No. 82013.

\_\_\_\_\_ 1982, Solar Phys., 77, 205.

Karpen, J. T., Crannell, C. J., and Frost, K. J. 1979, Astrophys. J., 234, 370.

Kattenberg, A., and Kuperus, M. 1983, Solar Phys., 85, 185.

Kaufmann, P., Strauss, F. M., Costa, J. E. R., Dennis, B. R., Kiplinger, A. L., Frost, K. J., and Orwig, L. E. 1983, Solar Phys., 84, 311.

Kiplinger, A. L., Dennis, B. R., Enslie, A. G., Frost, K. J., and Orwig, L. E. 1983, Astrophys. J. Lett., 265, L99.

Korchak, A. A. 1965, Geomagn. Aeron., 5, 32 and 601.

\_\_\_\_\_ 1967, Astron. Zh., 44, 328; English trans. Soviet Astron. = A. J., 11, 258.

\_\_\_\_\_ 1971, Solar Phys., 18, 284.

Kosugi, T. 1981, Solar Phys., 71, 91.

Krüger, A. 1979, Introduction to Solar Radio Astronomy and Radio Physics (Dordrecht: Reidel).

Kundu, M. R. 1965, Solar Radio Astronomy (New York: Wiley Interscience).

Lin, R. P. 1974, in Coronal Disturbances, IAU Symp. 57, G. Newkirk, ed., p. 201.

MacDonald, W. M., Rosenbluth, M. N., and Chuck, W. 1957, Phys. Rev., 107, 350.

Magun, A., Fuhrer, M., Kaempfer, N., Staehli, M., Schöchlin, W., Wiehl, H. 1981, Institute of Applied Physics Report 46, University of Berne, Switzerland.

Makishima, K. 1982, Proc. Hinotori Symp. on Solar Flares (Tokyo: Institute Space Astronaut. Sci.), p. 102.

Mannheimer, W. M. 1977, Phys. Fluids, 20, 265.

Marsh, K. A., and Hurford, G. J. 1982, Ann. Rev. Astron. Astrophys., p. 497.

Matteson, J. L. 1971, Ph. D. Thesis, UCSD, San Diego, California.

Mätzler, C. 1978, Astron. Astrophys., 70, 181.

Mätzler, C., Bai, T., Crannell, C. J., and Frost, K. J. 1978, Astrophys. J., 223, 1058.

Maxon, M. S., and Corman, E. G. 1967, Phs. Rev., 163, No. 1, 156.

Melrose, D. B. 1974, Solar Phys., 34, 421.

\_\_\_\_\_ 1979, Plasma Astrophysics (London: Gordon and Breach), 2 vols.

Melrose, D. B., and Brown, J. C. 1976, M. N. R. A. S., 176, 15.

Montgomery, D. C., and Tidman, D. A. 1964, Plasma Kinetic Theory (New York: McGraw-Hill), p. 30.

Orwig, L. E., Frost, K. J., and Dennis, B. R. 1980, Solar Phys., 65, 25.

Peterson, L. E., and Winckler, J. R. 1958, Phys. Rev. Lett., 1, 205.

\_\_\_\_\_ 1959, J. Geophys. Res., 64, 697.

Petrosian, V. 1973, Astrophys. J., 186, 291.

Petschek, H. E. 1964, AAS-NASA Symp. on Physics of Solar Flares, W. N. Hess, ed. (Greenbelt: NASA), p. 425.

Priest, E. R. 1978, Solar Phys., 58, 57.

\_\_\_\_\_ 1981a, ed., Solar Flare Magnetohydrodynamics (New York: Gordon and Breach).

\_\_\_\_\_ 1981b, in Solar Flare Magnetohydrodynamics, E. R. Priest, ed., p. 139.

Quigg, C. 1967, Lawrence Radiation Laboratory Report UCRL - 50227, "A Relativistic Calculation of the Bremsstrahlung Spectrum of a Maxwell-Boltzmann Plasma."

\_\_\_\_\_ 1968, Phys. Fluids, 11, 461 and 1592.

Ramaty, R. 1969, Astrophys. J., 158, 753.

Ramaty, R., and Petrosian, V. 1972, Astrophys. J., 178, 241.

Reif, F. 1965, Fundamentals of Statistical and Thermal Physics (New York: McGraw-Hill).

Reigler, G. R. 1969, Ph. D. Dissertation, University of Maryland, published as NASA-X-611-69-1, "An X-Ray Survey of the Sky from Balloon Altitudes".

- Roy, J. R., and Datlowe, D. W. 1975, Solar Phys., 40, 165.
- Rust, D. M. 1976, Phil. Trans. R. Soc. Lond. A, 281, 427.
- Rust, D. M., and Bar, V. 1973, Solar Phys., 33, 445.
- Rust, D. M., and Emslie, A. G., eds. 1979, Report UAG-72 1979, Energy Release in Solar Flares, Proceedings of the Workshop on Energy Release in Flares, 26 Feb. - 1 Mar. 1979, Cambridge, Mass., U. S. A. (Boulder, CO: U. S. Department of Commerce, NOAA).
- Sagdeev, R. Z., and Galeev, A. A. 1969, Nonlinear Plasma Theory (New York: Benjamin), section III-2.
- Schöchlin, W., and Magun, A. 1979, Solar Phys., 64, 349.
- Severny, A. B. 1958, Izv. Krymsk. Astrofiz. Obs., 20, 22.
- Shklovskii, I. S. 1964, Nature, 202, 275.
- \_\_\_\_\_ 1965, Soviet Astron. — A. J., 8, 538.
- Smith, D. F. 1975, Astrophys. J., 201, 521.
- \_\_\_\_\_ 1980, Solar Phys., 66, 135.
- Smith, D. F., and Auer, L. H. 1980, Astrophys. J., 238, 1126 (SA).
- Smith, D. F., and Brown, J. C. 1980, Astrophys. J., 242, 799 (SB).
- Smith, D. F., and Harmony, D. W. 1981, Proceedings of an International School and Workshop on Plasma Astrophysics held at Varenna, Como, Italy, 27 Aug. - 7 Sept. 1981 (SH1).
- \_\_\_\_\_ 1982, Astrophys. J., 252, 800 (SH2).
- Smith, D. F., and Lilliequist, C. G. 1979, Astrophys. J., 232, 582 (SL).
- Spicer, D. S. 1976, NRL Rept., No. 8036.
- \_\_\_\_\_ 1977a, Solar Phys., 53, 305.
- \_\_\_\_\_ 1977b, Solar Phys., 54, 379.
- Spitzer, L., Jr. 1962, Physics of Fully-Ionized Gases (New York: Wiley Interscience).
- Spruit, H. C. 1981, in The Sun as a Star, S. Jordan, ed., NASA SP-450.
- Sturrock, P. A. 1980, ed., Solar Flares, A Monograph from Skylab Workshop II (Boulder: University of Colorado Press).

- Svestka, Z. 1976, Solar Flares (Dordrecht: Reidel).
- Svestka, Z., Krieger, A. S., Chase, R. C., and Howard, R. 1977, Solar Phys., 52, 69.
- Syrovatskii, S. I., and Schmeleva, O. P. 1972, Solar Phys., 33, 341.
- Takakura, T. 1967, Solar Phys., 1, 304.  
\_\_\_\_\_ 1972, Solar Phys., 26, 151.
- Takakura, T., and Kai, 1966, Publ. Astron. Soc. Japan, 18, 57.
- Takakura, T., Ohki, K., Tsuneta, S., and Nitta, N. 1983, in Recent Advances in the Understanding of Solar Flares, ed. Y. Uchida, S. R. Kane, H. S. Hudson, K. Tanaka, to be published as a special issue of Solar Phys.
- Takakura, T., and Scalise, E. Jr. 1970, Solar Phys., 11, 434.
- Tandberg-Hanssen, E. A., Hudson, H. S., Dabbs, J. R., Baity, W. A. 1983, NASA Technical Paper 2168.
- Tarnstrom, G. L. 1976, Astron. Astrophys., 49, 31.  
\_\_\_\_\_ 1977, Astron. Astrophys., 58, 181.
- Trubnikov, B. A. 1958, dissertation, Moscow University (English translation 1960, USARC Tech. Information Service AEC-tr-4073).
- Trulsen, J., and Fejer, J. A. 1970, J. Plasma Phys., 4, 825.
- Tsuneta, S. 1983, Institute of Space and Astronaut. Sci. Research Note 239, Tokyo, Japan.
- Tucker, W. H. 1975, Radiation Processes in Astrophysics (Cambridge: MIT Press).
- Van Beek, H. F., de Feiter, L. D., and de Jager, C. 1974, Space Res., 14, 447.
- Van Beek, H. F., Hoyng, P., Lafleur, B., and Sinnott, G. M. 1980, Solar Phys., 65, 73.
- Van Hoven, G. 1976, Solar Phys., 49, 95.  
\_\_\_\_\_ 1981, in Solar Flare Magnetohydrodynamics, E. R. Priest, ed.
- Van Hoven, G., Anzer, U., Barbosa, D. D., Birn, J., Cheng, C.-C., Hansen, R. T., Jackson, B. V., Martin, S. F., McIntosh, P. S., Nakagawa, Y., Priest, E. R., Reeves, E. M., Reichmann, E. J., Schmahl, E. J., Smith, J. B., Solodyna, C. V., Thomas, R. J., Uchida, Y., and Walker, A.

B. C. 1980, in Solar Flares, P. A. Sturrock, ed.

Vlahos, L., and Papadopoulos, K. 1979, Astrophys. J., 233, 717.

Wiehl, H. J., Batchelor, D. A., Crannell, C. J., Dennis, B. R., and Price, P. N. 1983, NASA Tech. Memo. 85052; also condensed and submitted to Solar Phys..

Wiehl, H. J., Schöchlin, W. A., and Magun, A. 1980, Astron. Astrophys., 92, 260.

Wild, J. P., and Hill, E. R. 1971, Australian J. Phys., 24, 43.

Zheleznyakov, V. V. 1965, Soviet Astron. — A. J., 9, 73.

Zolcinski, M. C., Forrest, D. J., Ryan, J. M., Chupp, E. L., Kanbach, G., Reppin, C., Rieger, E., and Share, G. E. 1983, Adv. Space Res., 2, no. 11, p. 193.

**Page Intentionally Left Blank**

APPENDIX: PROGRAMS FOR SIMULATION OF PULSE PILE-UP

C  
C  
C

TITLE DATLOW

SUBROUTINE DATLOW(OLDEDG, OLDENG, FLXFLD, SIGMFL, NFLX, ENEDGE, ENMEAN)

C

C THIS SUBROUTINE USES DATLOWE'S PROCEDURE TO SIMULATE THE RESPONSE  
C OF THE SMM HXRBS DETECTOR TO SOLAR FLARE X-RAYS.

C

C REFERENCES:

C

C DATLOWE, D. W., SPACE SCIENCE INSTRUMENTATION, VOL. 1, 1975, P. 389.

C DATLOWE, D. W., NUCLEAR INSTRUMENTS AND METHODS, VOL. 145, 1977,

C

P. 365.

C

C THE NOTATION OF 1977 IS USED THROUGHOUT FOR CONSISTENCY.

C

C OLDEDG IS THE (NFLX+1)-ELEMENT ARRAY OF ENERGY CHANNEL EDGES

C PASSED FROM THE MAIN PROGRAM AND IS NOT DESTROYED.

C EDGES ARE EQUALLY-SPACED IN LOG E SPACE.

C OLDENG IS THE NFLX-ELEMENT ARRAY OF ENERGY CHANNEL CENTERS IN

C LOG E SPACE.

C ENEDGE IS THE (NFLX+1)-ELEMENT ARRAY OF ENERGY CHANNEL EDGES.

C \*\*NOT HXRBS CHANNEL EDGES\*\* THESE ARE EQUALLY-SPACED

C IN E SPACE ON RETURN.

C ENMEAN IS THE NFLX-ELEMENT ARRAY OF ENERGY CHANNEL CENTERS.

C FLXFLD IS THE NFLX-ELEMENT ARRAY OF SPECTRAL INTENSITIES IN

C PHOTONS/(S CM\*\*2 KEV) FOR ENERGIES CENTERED IN THE

C CHANNELS (AT OLDENG ON CALL, AT ENMEAN ON RETURN).

C

REAL\*4 LOFV, LVIP, LEXTND, LVNORM, LXNORM, NU, NP1FAC

INTEGER\*4 HTINDX

DIMENSION OLDENG(200), OLDEDG(201), E(200), W(200)

DIMENSION FLXFLD(200), FLXLOG(200), LOFV(200), LVIP(289)

DIMENSION ENEDGE(201), ENMEAN(200), ENMLOG(200)

DIMENSION FL1(288), FL2(288), D(200), SINC(288)

DIMENSION LEXTND(288), VEXTND(289), SIGMFX(288)

DIMENSION S(200), V(200), VIP(289), SIGMFL(200)

DIMENSION BL1(288), BL2(288), B(288), B1(288)

DIMENSION EEXTND(288), BINC(288)

DIMENSION SEXTND(288), WEXTND(288), DEXTND(288)

C

C THE OBJECT OF THE FOLLOWING EQUIVALENCE IS TO CONSERVE MEMORY.

C

EQUIVALENCE (ENMLOG(1), LVIP(1)), (LOFV(1), LEXTND(89))

EQUIVALENCE (FLXLOG(1), V(1), SINC(1), BINC(1), VEXTND(1))

EQUIVALENCE (E(1), EEXTND(89)), (W(1), WEXTND(89))

EQUIVALENCE (S(1), SEXTND(89)), (D(1), DEXTND(89))

EQUIVALENCE (FL1(1), BL1(1)), (FL2(1), BL2(1))

EQUIVALENCE (B1(1), DEXTND(1))

COMMON/OPVAR/ICMD, LIST, IERR, IDELE(15), IOP(20), ROP(20)

COMMON /DATPAR/ L, PHI1, PHI2, NU

C  
 C LOFV CONTAINS PULSE SHAPE INFORMATION.  
 C

```

DATA LOFV/130.,55.,44.,37.,33.,30.,29.,26.,25.,25.,
β      23.,22.,22.,21.,20.,28.,48.,46.,46.,47.,
β      45.,45.,45.,44.,44.,44.,43.,44.,43.,42.,
β      43.,42.,41.,43.,41.,41.,41.,41.,40.,41.,
β      41.,39.,41.,40.,40.,39.,40.,39.,39.,39.,
β      39.,39.,39.,39.,39.,38.,39.,38.,38.,38.,
β      39.,37.,39.,38.,37.,38.,38.,38.,38.,37.,
β      38.,37.,38.,38.,37.,37.,37.,38.,37.,38.,
β      36.,38.,37.,38.,37.,37.,38.,37.,37.,38.,
β      37.,37.,37.,38.,38.,36.,38.,37.,38.,38.,
β      37.,38.,38.,37.,38.,39.,37.,38.,38.,38.,
β      38.,39.,38.,39.,37.,39.,39.,38.,39.,39.,
β      39.,40.,39.,40.,39.,40.,40.,39.,41.,41.,
β      39.,41.,41.,41.,41.,41.,42.,42.,41.,42.,
β      43.,42.,43.,43.,44.,43.,44.,44.,45.,44.,
β      45.,46.,45.,46.,46.,48.,46.,48.,48.,49.,
β      48.,50.,50.,50.,52.,51.,52.,53.,54.,54.,
β      56.,56.,56.,58.,58.,60.,61.,62.,62.,66.,
β      65.,68.,70.,71.,73.,75.,79.,80.,85.,88.,
β      92.,97.,104.,111.,120.,132.,150.,178.,230.,556./
DATA SEXTND/288*0./
DATA WEXTND/288*0./
DATA DEXTND/288*0./

```

C  
 C THE FOLLOWING STATEMENT FUNCTION DEFINES THE PULSE SHAPE  
 C

```

XI(TP)=1.28*TP**2*(3.-TP)*EXP(-TP)

```

C  
 C WE FIRST INTERPOLATE THE SPECTRUM TO LINEAR E SPACE.  
 C

```

CALL FINLUN('LP',IPLU)
NEDGES=NFLX+1
NBINS=200
NBINSX=288
IZEROB=88
EMAX=ROP(11)*0.97
DELTE=EMAX/NEDGES

```

C IS THE WIDTH OF INTERPOLATED BINS IN E SPACE

```

DELHLF=0.5*DELTE
DO 5 I=1,NFLX
RI=I
E(I)=RI*DELTE
ENMEAN(I)=E(I)
ENEDGE(I)=ENMEAN(I)-DELHLF
ENMLOG(I)=ALOG10(OLDENG(I))
IF(FLXFLD(I).LE.1.E-19)GO TO 5
FLXLOG(I)=ALOG10(FLXFLD(I))

```

5 CONTINUE

```

ENEDGE(NEDGES)=ENMEAN(NFLX)+DELHLF

```

X WRITE(IPLU,1100)(OLDENG(I),I=1,NFLX)

```

X1100 FORMAT('OLDENG=',/, (1X,10(F10.3)))
X   WRITE(IPLU,1200)(FLXFLD(I),I=1,NFLX)
X1200 FORMAT(' FLXFLD=',/, (1X,10(1PE10.2)))
X   WRITE(IPLU,1300)DELTE,NFLX,EMAX
X1300 FORMAT(' DELTE=',F10.3,'   NFLX=',I5,'   EMAX=',F10.3)
C
C   INTERPOLATE TO NEW ENERGY BINS
C
      DO 100 I=1,NFLX
      S(I)=0.
      K=0
50    K=K+1
      KP1=K+1
      IF(KP1.GT.NFLX)GO TO 100
      E2=OLDENG(KP1)
      E1=OLDENG(K)
      IF(E1.GE.E(I).OR.E2.LE.E(I))GO TO 50
      IF(FLXFLD(K).LE.1.E-19.OR.FLXFLD(KP1).LE.1.E-19)GO TO 100
      Q=ALOG10(E(I)/E1)/ALOG10(E2/E1)
      S(I)=10.**(FLXLOG(K)+Q*(FLXLOG(KP1)-FLXLOG(K)))
100  CONTINUE
X   WRITE(IPLU,1400)(E(I),I=1,NFLX)
X1400 FORMAT('1E=',/, (1X,10(F10.3)))
X   WRITE(IPLU,1420)(S(I),I=1,NFLX)
X1420 FORMAT(' INTERPOLATED FLXFLD=',/, (1X,10(1PE10.2)))
C
C   NOW THE SPECTRUM S IS KNOWN FOR LINEARLY SPACED ENERGIES.
C   NEXT THE NORMALIZATION CONSTANT IS FOUND BY INTEGRATION.
C
      SINTEG=0.
      DO 190 I=1,NFLX
      SINTEG=SINTEG+S(I)
190  CONTINUE
C
      TAU=(3.-SQRT(3.))*0.75E-6+1.2E-6
C       IS THE COINCIDENCE TIME OF THE DETECTOR IN SECONDS
C       (CORRECTED FOR GATE OPENNING BEFORE PULSE RISE)
C   THE SPECTRUM IS NORMALIZED TO UNITS PROBABILITY/KEV.
C
      SNORM=SINTEG*DELTE
      SPROB=0.
      DO 200 I=1,NFLX
      S(I)=S(I)/SNORM
      IF(S(I).LE.1.E-19)S(I)=0.
      SPROB=SPROB+S(I)
200  CONTINUE
      SPROB=SPROB*DELTE
X   WRITE(IPLU,1500)(S(I),I=1,NFLX)
X1500 FORMAT(' S=',/, (1X,10(1PE10.2)))
X   WRITE(IPLU,1510)SPROB
X1510 FORMAT('ONORMALIZATION OF S=',F8.6)
C
      PREC=ROP(12)

```

```

C      IS THE MAXIMUM TOLERABLE RELATIVE ERROR IN THE SPECTRUM.
SIG=ROP(2)
C      IS THE DETECTOR CRYSTAL AREA.
R=SINTEG*SIG*DELTE
C      IS THE TOTAL COUNTS PER SECOND SEEN BY THE DETECTOR.
X      WRITE(IPLU,1600)R
X1600  FORMAT(' R=',1PE10.2)
      NU=R*TAU
C      IS THE MEAN NUMBER OF COUNTS PER COINCIDENCE TIME TAU.
C
      PHI1=0.
      DO 210 I=1,NFLX
      PHI1=PHI1+E(I)*S(I)
210    CONTINUE
      PHI1=PHI1*R*DELTE
C      IS THE INTEGRATED INCIDENT ENERGY FLUX.
C
X      WRITE(IPLU,1620)PREC,SIG,TAU,NU
X1620  FORMAT(' PREC=',1PE9.1,' SIG=',0PF5.1,
X      β ' TAU=',1PE10.2,' NU=',1PE10.2)
C
C PULSE SHAPE INFORMATION IS INCORPORATED IN THE FOLLOWING STEPS.
C
      TPMAX=3.-SQRT(3.)
      VMAX=XI(TPMAX)
      RNBINS=NBINS
      BINRAT=1./RNBINS
      DO 220 I=1,NBINS
      W(I)=0.
      RI=I
      V(I)=RI*BINRAT*VMAX
220    CONTINUE
      DO 250 I=1,NFLX
      IP=NFLX-I+1
      RIP=IP
      DO 225 J=1,IP
      RJ=J
      VIP(J)=(RJ/RIP)*VMAX
      LVIP(J)=0.
225    CONTINUE
      LVNORM=0.
      INDV=1
      INDVIP=1
      DELVIN=0.1*BINRAT*VMAX
      N=1
      NLIM=10*NBINS
230    IF(N.EQ.NLIM)GO TO 240
      RN=N
      VINTEG=RN*DELVIN
      IF(VINTEG.GT.V(INDV))INDV=MINO(INDV+1,NBINS)
      IF(VINTEG.GT.VIP(INDVIP))GO TO 235
232    LVIP(INDVIP)=LVIP(INDVIP)+LOFV(INDV)
      N=N+1

```

```

GO TO 230
235 LVNORM=LVNORM+LVIP(INDVIP)
INDVIP=MINO(INDVIP+1,IP)
GO TO 232
240 LVIP(IP)=LVIP(IP)+LOFV(NBINS)
LVNORM=LVNORM+LVIP(IP)
C WRITE(IPLU,1624)LVNORM
C1624 FORMAT('0LVNORM=',F9.7)
DO 245 J=1,IP
LVIP(J)=LVIP(J)/LVNORM
W(J)=W(J)+S(IP)*LVIP(J)
245 CONTINUE
C WRITE(IPLU,1626)(LVIP(K),K=1,IP)
C1626 FORMAT('0LVIP=',/, (1X,10F10.7))
250 CONTINUE
WPROB=0.
DO 260 I=1,NFLX
IF(W(I).LE.1.E-19)W(I)=0.
WPROB=WPROB+W(I)
260 CONTINUE
WPROB=WPROB*DELTE
X WRITE(IPLU,1630)(W(I),I=1,NFLX)
X1630 FORMAT('1W=',/, (1X,10(1PE10.2)))
X WRITE(IPLU,1632)WPROB
X1632 FORMAT(' NORMALIZATION OF W=',F8.6)
C
C THE FOLLOWING STEPS COMPUTE BASELINE PILE-UP CONTRIBUTIONS
C
TO=0.75E-6
TMAX=TPMAX*TO
TF=TAU/TO
TPMIN=3.+SQRT(3.)
VMIN=XI(TPMIN)
VRANGE=VMAX-VMIN
RNFLX=NFLX
REBNEG=-VMIN*RNFLX/VMAX
NEBNEG=REBNEG
NEBNEG=NEBNEG+1
NENERG=NFLX+NEBNEG
RENERG=NENERG
NBOT=IZEROB+1-NEBNEG
NTOP=IZEROB+NFLX
IF(NBOT.GE.1.AND.NTOP.LE.NBINSX)GO TO 261
WRITE(IPLU,1633)NBOT,NTOP
1633 FORMAT('0NBOT=',I3,' NTOP=',I3)
261 CONTINUE
X WRITE(IPLU,1634)NEBNEG,NENERG,NBOT,NTOP
X1634 FORMAT('0NUM. OF NONPOSITIVE ENERGY BINS=',I4,
X β ' TOTAL NUM. OF ENERGY BINS=',I4,
X β ' NBOT=',I3,' NTOP=',I3)
DO 262 I=1,NBINSX
LEXTND(I)=0.
VEXTND(I)=0.

```

```

262 CONTINUE
DO 263 J=NBOT,NTOP
RJ=J-NBOT+1
VEXTND(J+1)=(RJ/RENERG)*VRANGE+VMIN
263 CONTINUE
VEXTND(NBOT)=VMIN *1.01
VEXTND(NTOP+1)=VMAX*1.01
DELTTP=TF*1.E-4
K=IZEROB
RDELT=R*TAU*1.E-4
TLIMIT=1./R
HTINDX=-1
264 HTINDX=HTINDX+1
RTINDX=HTINDX
TP=RTINDX*DELTTP
T=TP*TO
F=XI(TP)
RDELT=RDELT*EXP(-R*T)
IF(T.GT.TLIMIT.OR.HTINDX.EQ.100000)GO TO 268
IF(TP.GT.TPMAX.AND.TP.LT.TPMIN)GO TO 266
265 IF(VEXTND(K).LE.F.AND.F.LT.VEXTND(K+1))LEXTND(K)=LEXTND(K)+RDELT
IF(F.LT.VEXTND(K+1))GO TO 264
K=K+1
GO TO 265
266 IF(VEXTND(K).LE.F.AND.F.LT.VEXTND(K+1))LEXTND(K)=LEXTND(K)+RDELT
IF(F.GT.VEXTND(K))GO TO 264
K=K-1
GO TO 266
268 CONTINUE
X NBXPL1=NBINSX+1
X WRITE(IPLU,1642)(VEXTND(I),I=1,NBXPL1)
X1642 FORMAT('OVEXTND=',/,(1X,10F10.6))
LXNORM=0.
DO 270 I=NBOT,NTOP
LXNORM=LEXTND(I)+LXNORM
270 CONTINUE
X WRITE(IPLU,1644)LXNORM
X1644 FORMAT('OLXNORM=',1PE10.2)
DO 272 I=NBOT,NTOP
LEXTND(I)=LEXTND(I)/LXNORM
272 CONTINUE
X WRITE(IPLU,1645)(LEXTND(I),I=1,NBINSX)
X1645 FORMAT('OLEXTND=',/,(1X,10F10.5))
DO 274 I=1,NBINSX
B1(I)=0.
BL2(I)=0.
B(I)=0.
274 CONTINUE
DO 290 I=1,NFLX
IP=NFLX-I+1
RIP=IP
DELVIP=VMAX/RIP
J=IP

```

```

276 RJ=J
    JP=J+IZEROB
    VIP(JP)=RJ*DELVIP
    VTEST=VIP(JP)-DELVIP
    LVIP(JP)=0.
    IF(VTEST.LT.VMIN)GO TO 278
    J=J-1
    GO TO 276
278 LVNORM=0.
    JPMIN=JP
    JPMAX=IP+IZEROB
    INDVEX=NBOT
    INDVIP=JPMIN
    DELVIN=0.1*BINRAT*VRANGE
    N=1
280 IF(N.EQ.NLIM)GO TO 286
    RN=N
    VINTEG=VMIN+RN*DELVIN
    IF(VINTEG.GT.VEXTND(INDVEX))INDVEX=MINO(INDVEX+1,NTOP)
    IF(VINTEG.GT.VIP(INDVIP))GO TO 284
282 LVIP(INDVIP)=LVIP(INDVIP)+LEXTND(INDVEX)
    N=N+1
    GO TO 280
284 LVNORM=LVNORM+LVIP(INDVIP)
    INDVIP=MINO(INDVIP+1,JPMAX)
    GO TO 282
286 LVIP(JPMAX)=LVIP(JPMAX)+LEXTND(NTOP)
    LVNORM=LVNORM+LVIP(JPMAX)
C    WRITE(IPLU,1646)LVNORM
C1646 FORMAT('0LVNORM=',F9.7)
    DO 288 J=JPMIN,JPMAX
    LVIP(J)=LVIP(J)/LVNORM
    B1(J)=B1(J)+S(IP)*LVIP(J)
288 CONTINUE
C    WRITE(IPLU,1647)(VIP(K),K=JPMIN,JPMAX)
C1647 FORMAT('0VIP=',/,(1X,10F10.7))
C    WRITE(IPLU,1648)(LVIP(K),K=JPMIN,JPMAX)
C1648 FORMAT('0LVIP=',/,(1X,10F10.7))
290 CONTINUE
C
C WE NOW HAVE THE PROBABILITY DISTRIBUTION OF BASELINE SHIFTS
C IN ARRAY B1—FOR SINGLE PULSES. NEXT WE MUST CONVOLVE IT
C WITH ITSELF TO GENERATE THE SHIFT DISTRIBUTION FOR MULTIPLE
C PULSES.
C
    B1NRM=0.
    DO 291 I=NBOT,NTOP
    IF(B1(I).LE.1.E-19)B1(I)=0.
    B1NRM=B1NRM+B1(I)
291 CONTINUE
    B1PROB=B1NRM*DELTE
X    WRITE(IPLU,1649)(B1(I),I=1,NBINSX)
X1649 FORMAT('0B1=',/,(1X,10(1PE10.2)))

```

```

X      WRITE(IPLU,1650)B1PROB
X1650 FORMAT('ONORMALIZATION OF B1=',F8.6)
C
C      EXTEND THE ENERGY BINS INTO THE NEGATIVE ENERGY RANGE
C
      DO 292 I=1,NEBNEG
      RI=I
      IP=IZEROB-I+1
      EEXTND(IP)=(1.-RI)*DELTE
292    CONTINUE
X      WRITE(IPLU,1651)(EEXTND(I),I=1,NBINSX)
X1651 FORMAT('OEEXTND=',/, (1X,10F10.3))
      RTO=R*TO
      C1=1./(EXP(RTO)-1.)
      C2=C1*RTO
      DO 300 I=NBOT,NTOP
      BL1(I)=B1(I)
      B(I)=C2*B1(I)
      IF(B(I).LE.1.E-19)B(I)=0.
300    CONTINUE
X      WRITE(IPLU,1660)(B(I),I=1,NBINSX)
X1660 FORMAT('O',30X,' 1-PULSE BASELINE SHIFT DISTRIBUTION',//,
X       $\beta$  (1X,10(1PE10.2)))
      M=1
      FACTRM=1.
310    M=M+1
      RM=M
      TEST=ALOG10(RM)+ALOG10(FACTRM)
      IF(TEST.LT.-37.)GO TO 350
      FACTRM=FACTRM*M
      C=C1*RTO**M/FACTRM
      CALL FOLD(EEXTND,B1,NBOT,NTOP,DELTE,NENERG,BL1,BL2)
      BNORM=0.
      DO 320 I=NBOT,NTOP
      BNORM=BNORM+BL2(I)
320    CONTINUE
      BPROB=BNORM*DELTE
X      WRITE(IPLU,1670)M,BPROB
X1670 FORMAT('ONORMALIZATION OF B(',I2,',')=',F8.6)
      RBIMAX=0.
      DO 330 I=NBOT,NTOP
      BINC(I)=0.
      BL2(I)=BL2(I)/BPROB
      IF(BL2(I).GT.1.E-19)GO TO 323
      BL2(I)=0.
      GO TO 325
323    TEST=ALOG10(C)+ALOG10(BL2(I))
      IF(TEST.GE.-19.)BINC(I)=C*BL2(I)
      IF(B(I).LE.0.)GO TO 325.
      RBI=BINC(I)/B(I)
      IF(RBI.LE.RBIMAX)GO TO 325
      RBIMAX=RBI
325    B(I)=B(I)+BINC(I)

```

```

330 CONTINUE
X WRITE(IPLU,1680)M,(BINC(I),I=1,NBINSX)
X1680 FORMAT('0',30X,I2,'-PULSE BASELINE SHIFT DISTRIBUTION',
X   β //,(1X,10(1PE10.2)))
      IF(RBIMAX.LE.PREC)GO TO 350
      DO 340 I=NBOT,NTOP
      BL1(I)=BL2(I)
340 CONTINUE
      GO TO 310
350 CONTINUE
X WRITE(IPLU,1690)(B(I),I=1,NBINSX)
X1690 FORMAT('0',30X,'TOTAL BASELINE SHIFT PROBABILITY DISTRIBUTION',
X   β //,(1X,10(1PE10.2)))
C
C NOW WE CONVOLVE THE BASELINE SHIFT DISTRIBUTION WITH THE INCIDENT
C SPECTRUM TO GET THE 1-PULSE PILE-UP DISTRIBUTION AS IN EQ. (18) OF
C DATLOWE 1977.
C
      CALL FOLD(EEXTND,SEXTND,NBOT,NTOP,DELTE,NENERG,
      β B,FL1)
C
C THE FOLLOWING STEPS COMPUTE THE PILED-UP VERSION OF THE
C FLARE SPECTRUM. ARRAY D IS USED FOR THE
C SPECTRUM AND IS CORRECTED ITERATIVELY. IF THE EFFECTS OF
C LTH-ORDER PILE-UP WERE NOT NEGLIGIBLE (TO THE REQUESTED
C PRECISION) THEN (L+1)TH-ORDER EFFECTS ARE INCLUDED.
C
699 C1=EXP(-NU)/TAU
      C2=C1*NU
      UNCERT=.1
      DO 700 I=NBOT,NTOP
      IF(FL1(I).LE.1.E-19)FL1(I)=0.
      DEXTND(I)=C2*SEXTND(I)
      SIGMFX(I)=UNCERT*DEXTND(I)
700 CONTINUE
X WRITE(IPLU,1855)(DEXTND(I),I=1,NBINSX)
X1855 FORMAT('0',30X,' 1-PULSE CONTRIBUTION (COUNTS/(S KEV))',//,
X   β (1X,10(1PE10.2)))
C
      L=1
      FACTRL=1.
C
C NOW THE ITERATION STARTS, I.E. ADDING OF NON-NEGLIGIBLE
C PILE-UP CONTRIBUTIONS OF 2ND AND HIGHER ORDER.
C
800 L=L+1
      UNCFAC=1.-(1.-UNCERT)**L
      RL=L
      TEST=ALOG10(RL)+ALOG10(FACTRL)
      IF(TEST.LT.-37.)GO TO 950
      FACTRL=FACTRL*L
      C=C1*NU**L/FACTRL

```

C

C SUBROUTINE FOLD PRODUCES THE (L+1)TH-ORDER PILE-UP  
 C DISTRIBUTION FROM THE LTH-ORDER ONE. ARRAY FL1 CONTAINS  
 C DATLOWE'S F(L-1). THE SUBROUTINE WILL USE THAT TO  
 C COMPUTE F(L) IN ARRAY FL2. SEE DATLOWE, 1975, EQ. (8A).

C  
 CALL FOLD(EEXTND,WEXTND,NBOT,NTOP,DELTE,NENERG,  
 $\beta$  FL1,FL2)

C  
 FNORM=0.  
 DO 850 I=NBOT,NTOP  
 FNORM=FNORM+FL2(I)

850 CONTINUE  
 FPROB=FNORM\*DELTE

X WRITE(IPLU,1860)L,FPROB  
 X1860 FORMAT('ONORMALIZATION OF F(',I2,')=',F8.6)

C  
 C THE FOLLOWING STEPS CORRECT THE SPECTRUM FOR THE NEXT ORDER  
 C OF PILE-UP. IN THE PROCESS, THE MAXIMUM FRACTIONAL  
 C CONTRIBUTION OF THIS ORDER IS RECORDED.

C  
 RSIMAX=0.  
 DO 900 I=NBOT,NTOP  
 SINC(I)=0.  
 FL2(I)=FL2(I)/FPROB  
 IF(FL2(I).GT.1.E-19)GO TO 880  
 FL2(I)=0.  
 GO TO 890

880 TEST=ALOG10(C)+ALOG10(FL2(I))  
 IF(TEST.GE.-19.)SINC(I)=C\*FL2(I)  
 IF(DEXTND(I).EQ.0.)GO TO 890  
 RSI=SINC(I)/DEXTND(I)  
 IF(RSI.LE.RSIMAX)GO TO 890  
 RSIMAX=RSI

890 DEXTND(I)=DEXTND(I)+SINC(I)  
 SIGMFX(I)=SIGMFX(I)+UNCFAC\*SINC(I)

900 CONTINUE

X WRITE(IPLU,1900)L,(SINC(I),I=1,NBINSX)  
 X1900 FORMAT('0',30X,I2,'-PULSE CONTRIBUTION (COUNTS/(S KEV))',  
 X  $\beta$  //,(1X,10(1PE10.2)))  
 IF(RSIMAX.LE.PREC)GO TO 950

C  
 C THE LAST ORDER OF PILE-UP WAS SIGNIFICANT. PREPARE FOR  
 C ANOTHER ITERATION.

C  
 DO 940 I=NBOT,NTOP  
 FL1(I)=FL2(I)  
 940 CONTINUE  
 GO TO 800

C  
 C THE LAST ORDER WAS NEGLIGIBLE, TO SPECIFIED PRECISION.

C  
 950 PHI2=0.  
 DO 960 I=NBOT,NTOP

```

PHI2=PHI2+DEXTND(I)*DEXTND(I)
960 CONTINUE
PHI2=PHI2*DELTE
C      IS THE INTEGRATED ENERGY FLUX COMPUTED WITH PILE-UP.
CONPAR=0.598203
SUM=1.
NP1FAC=1.
DO 970 N=1,L
RN=N
RNP1=RN+1.
NP1FAC=NP1FAC*RNP1
PROD=RN*CONPAR
SUM=SUM+(1.+PROD)*NU**N/NP1FAC
970 CONTINUE
SUM=SUM*EXP(-NU)
PHI2=PHI2/SUM
DPROB=0.
DO 990 I=NBOT,NTOP
DPROB=DPROB+DEXTND(I)
990 CONTINUE
DPROB=DPROB*DELTE*TAU
DNORM=1.-EXP(-NU)
X WRITE(IPLU,1990)DPROB,DNORM
X1990 FORMAT('ONORMALIZATION OF DEXTND=',F8.6,
X      β 1-EXP(-NU)=' ,F8.6)
DO 999 I=1,NFLX
FLXFLD(I)=D(I)/SIG
SIGMFL(I)=SIGMPX(I+IZEROB)
999 CONTINUE
X WRITE(IPLU,1940)(FLXFLD(I),I=1,NFLX)
X1940 FORMAT('0',30X,'PILED-UP SPECTRUM (COUNTS/(S CM**2 KEV)',
X      β //,(1X,10(1PE10.2)))
C
X WRITE(IPLU,1980)PHI1
X1980 FORMAT('0ENERGY FLUX COMPUTED FROM INCIDENT SPECTRUM =',
X      β 1PE11.4)
X WRITE(IPLU,2000)PHI2
X2000 FORMAT('0ENERGY FLUX COMPUTED FROM PILED-UP SPECTRUM =',
X      β 1PE11.4)
RETURN
END

```

C  
C  
C

TITLE FOLD

C

C THE FOLLOWING SUBROUTINE GENERATES THE (L+1)TH-ORDER  
C PILE-UP DISTRIBUTION FROM THE LTH-ORDER ONE. SEE  
C DATLOWE, EQ. (8A).

C

SUBROUTINE FOLD(E, W, NBOT, NTOP, DELTE, NENERG, FL1, FL2)

C

C THIS SUBROUTINE PERFORMS THE CONVOLUTIONS OF PROBABILITY  
C DISTRIBUTIONS IN DATLOWE'S EQ. 8A.

C

```

REAL*8 WFL1, SUM
DIMENSION E(288), W(288), FL1(288), FL2(288)
TOL=DELTE/10.
EMIN=E(NBOT)
EMINT=EMIN-TOL
DO 110 I=NBOT, NTOP
SUM=0.
M=0
EDIF=E(I)-E(NBOT)
IF(EDIF.LT.EMINT)GO TO 50
DO 40 K=NBOT, NTOP
Q=ABS(EDIF-E(K))
IF(Q.GT.TOL)GO TO 40
M=K
GO TO 50
40 CONTINUE
50 IF(M.EQ.0)GO TO 100
J=NBOT
60 K=M-J+NBOT
IF(K.LT.NBOT)GO TO 100
WFL1=W(J)*FL1(K)
SUM=SUM+WFL1
J=J+1
GO TO 60
100 FL2(I)=SUM*DELTE
110 CONTINUE
RETURN
END

```

## BIBLIOGRAPHIC DATA SHEET

1. Report No. 86102	2. Government Accession No.	3. Recipient's Catalog No.	
4. Title and Subtitle Energetic Electrons in Impulsive Solar Flares		5. Report Date May 1984	
		6. Performing Organization Code 682	
7. Author(s) David A. Batchelor		8. Performing Organization Report No.	
9. Performing Organization Name and Address Solar Physics Branch Laboratory for Astronomy and Solar Physics NASA/Goddard Space Flight Center Greenbelt, MD 20771		10. Work Unit No.	
		11. Contract or Grant No. NGT 34-003-801	
		13. Type of Report and Period Covered  Technical Memorandum	
12. Sponsoring Agency Name and Address		14. Sponsoring Agency Code	
15. Supplementary Notes			
<p><b>16. Abstract</b> A new analysis is made of a thermal flare model proposed by Brown, Melrose, and Spicer (1979) and Smith and Lilliequist (1979). They assumed the source of impulsive hard X rays to be a plasma at a temperature of order <math>10^8</math> K, initially located at the apex of a coronal arch, and confined by ion-acoustic turbulence in a collisionless conduction front. Such a source would expand at approximately the ion-sound speed, <math>c_s = (kT_e/m_i)^{1/2}</math>, until it filled the arch. Brown, Melrose and Spicer and Smith and Brown (1980) argued that the source assumed in this model would not explain the simultaneous impulsive microwave emission. In contrast, the new results presented here show that this model leads to the development of a quasi-Maxwellian distribution of electrons that explains both the hard X-ray and microwave emissions. This implies that the source sizes can be determined from observations of the optically-thick portions of microwave spectra and the temperatures obtained from associated hard X-ray observations. In this model, the burst emission would rise to a maximum in a time, <math>t_r</math>, approximately equal to <math>L/c_s</math>, where <math>L</math> is the half-length of the arch. New observations of these impulsive flare emissions are analyzed herein to test this prediction of the model. Observations made with the <u>Solar Maximum Mission</u> spacecraft and the Bern Radio Observatory are in good agreement with the model.</p>			
17. Key Words (Selected by Author(s)) Plasmas, Sun, flares, radio radiation X rays, impulsive bursts		18. Distribution Statement	
19. Security Classif. (of this report) Unclassified	20. Security Classif. (of this page) -	21. No. of Pages 168	22. Price*